Numerical study of the overturning circulation of the Persian Gulf

Master's thesis
written at the Leibniz-Institute for Baltic Sea Research Warnemünde
Partner Institute of the Faculty of Mathematics and Natural Sciences
at the University of Rostock

by Marvin Lorenz, born on 14. April 1993 in Eutin

Rostock, September 4, 2017

Abstract

In this study a model simulation for the Persian Gulf using the coastal ocean model GETM has been set up successfully. The simulation covers two years using the first year as a spin up. Although the model results are warmer and more saline, the density was in range with measurements. The main reason for the increased temperatures is found to be the shortwave radiation which was overestimated in the model. Dust aerosols from adjacent deserts reflect the radiation and decrease the short wave radiation over the Persian Gulf significantly.

Furthermore, the seasonal circulation of the Persian Gulf was reproduced. In spring when the heat flux is positive the Indian Ocean Surface Water (IOSW) reaches farther west due to a shallow thermocline restricting inflows to the upper 10-20 m. Because of persistent northwesterlies the IOSW forms a cyclonic circulation in the central and northern Gulf. In summer this circulation becomes strongest since the stratification reaches its maximum. In fall, when the heat flux decreases and evaporation increases, vertical mixing creates a deep mixed surface layer which weakens the spreading of IOSW. In addition, the cyclonic eddies dissolve into smaller eddies which dissipate in late fall/early winter. In winter almost the whole Persian Gulf is vertically homogeneously mixed and no significant surface circulation is found.

Besides the circulation the formation of the dense Persian Gulf Water (PGW) was investigated. The densest water in the Persian Gulf can be found in winter around Bahrain, but does only contribute little to the PGW due to mixing. The PGW is created in the northern and southern shallows. The dense water of the northern region sinks into the deep channel of the Gulf and moves to the Strait of Hormuz. The saline water of the southern shallows is too warm in summer and stratifies

over the denser water in the channel and becomes part of a near surface recirculation. In winter the southern shallows are responsible for the high salinities of the PGW. Comparison of the shape of the outflows' salinity distribution shows good agreement with observations although being too saline.

The transports through the Strait of Hormuz have been analysed using Total Exchange Flow theory. The exchange flow shows a seasonal cycle which closely follows the seasonal cycle of the circulation. The annual mean quantities for the exchange flow are: $Q_{in,year} = 0.20 \pm 0.02$ Sv, $Q_{out,year} = -0.19 \pm 0.02$ Sv, $s_{in,year} = 37.02$ g/kg and $s_{out,year} = 38.86$ g/kg. The highest transport rates are found in summer and the lowest in fall. These values compare well to estimates by other studies and measurement campaigns. Knowing $Q_{out,year}$, the residence time was estimated with 1.33 years which deviates from $\sim$5 years which is found to be the mean residence time. The heat exchange with the Gulf of Oman is found to be a net zero in an annual cycle.

Acknowledgement

First, I want to thank my family and my girlfriend who always supported me over the last five years. Without them I would not be the one I am today. Then I would like to thank my supervisors Hans and Ulf who gave me the opportunity to write this thesis and to make great experiences over the last year, in particular the participation at the 1st Bilateral German-Iranian Workshop on Kish Island and at the Baltic Sea Science Congress in Rostock. Furthermore, I want to thank all people in the physics department of IOW helping me solving model, programming or other problems which taught me a lot, namely Knut, Peter, Martin, Hagen, Selina, Xaver and Merten. Thank you Florian and Christiane for proofreading this thesis. Last but not least, I want to thank my office colleagues for the great working atmosphere which always made work feel more fun.

Contents

List of variables

ρ	density of the water	C_p	specific heat capacity
ρ_0	reference density	$I(z)$	shortwave radiation profile
$\hat{\rho}$	density perturbation from ρ_0	I_0	shortwave radiation for $I(z=0)$
ρ_{air}	air density	Q_θ	sources and sinks for temperature
$\mathbf{u}$	3-D velocity vector	Q_s	sources and sinks for salinity
u, v, w	x,y,z components of $\mathbf{u}$	C	tracer
u', v', w'	velocity fluctuations due to turbulence	w_s	settling velocity of C
t	time	Q_C	sources and sinks for C
$\mathbf{\Omega}$	Earth rotation vector	Q_S	sensible heat flux
f	Coriolis parameter	C_S	bulk transfer coefficient for Q_S
ϕ	latitude	Q_l	latent heat flux
$\mathbf{g}$	gravitational acceleration vector	Q_b	long-wave heat flux
g	absolute value of $\mathbf{g}$	Q_{net}	net heat flux
∇	3-D nabla operator	$Q_{\theta,in}$	imported heat flux from TEF
p	pressure	$Q_{\theta,out}$	exported heat flux from TEF
p_0	reference pressure	$Q_{\theta,net}$	net heat flux from TEF
$\hat{p}$	pressure perturbation from p_0	u_{10}	wind speed in 10m height
μ	viscosity	L	specific latent heat of water
ν	dynamic viscosity	C_E	bulk transfer coefficient for E
ν_t	turbulent dynamic viscosity	q	specific humidity
$\mathcal{R}$	Reynolds stress tensor	q_s	saturated specific humidity
A_H^X	horizontal eddy diffusivity of variable X	$\hat{u}$	temporal tidal mean velocity
c_μ	non-dimensional stability function	u_e	exchange flow intensity
k	turbulent kinetic energy	u_r	residual run off
ϵ	dissipation rate of k	$\hat{\zeta}$	temporal tidal mean surface height
ζ	surface height	Q_F	net fresh water flux
b	buoyancy	Q_R	river run off
H	bottom depth	B_0	surface buoyancy flux
E	evaporation rate	V	volume
P	precipitation rate	Q_{in}	inflowing transport
U, V	horizontal transports in x and y	$Q_{in,year}$	annual mean Q_{in}
$\boldsymbol{\tau}^b, \boldsymbol{\tau}^s$	bottom and surface stress tensor	Q_{out}	outflowing transport
n	outward normal vector	$Q_{out,year}$	annual mean Q_{out}
Θ	conservative temperature	Q	isohaline transport function
θ	in-situ temperature	F_{in}	inflowing salinity flux
θ_0	reference in-situ temperature	$F_{\theta,in}$	ingoing temperature flux
θ_{air}	air in-situ temperature	F_{out}	outflowing salinity flux
s	absolute salinity	$F_{\theta,out}$	outgoing temperature flux
s_0	reference absolute salinity	$\chi^{(C)}$	physical mixing of tracer C
s_{surf}	surface salinity	M	vertical integrated $\chi^{(C)}$
s_a	average salinity	$\chi^{(num)}$	numerical mixing
s_{in}	salinity of the inflow	$A\{C\}$	advection scheme of tracer C
$s_{in,year}$	annual mean s_{in}	T_i	passive marker tracer
s_{out}	salinity of the outflow	Δt	numerical time step
$s_{out,year}$	annual mean s_{out}	V_{PG}	volume of the Persian Gulf
α	thermal expansion coefficient	A_{PG}	surface area of the Persian Gulf
β	haline contraction coefficient	t_{res}	residence time

Chapter 1.

Introduction

The Persian Gulf is a semi-enclosed marginal sea located at the northwest of the Indian Ocean north of the Arabian peninsula and south of Iran. With a mean depth of $\sim$40 m and a surface area of $\sim$ 240,000 km^2 the Persian Gulf is a shallow sea with comparable size and depth to the Baltic Sea (377,000 km^2, 55 m). It is connected to the Gulf of Oman through the Strait of Hormuz which is 56 km wide at its narrowest point. In the north it is bordered by the Shatt-Al Arab river delta, which is also known as the Arvand river. A map of the Persian Gulf region is shown in figure 1.1 with the bordering countries.

The climate in the Persian Gulf region is arid, meaning high evaporation dominates the fresh water flux, causing the formation of the Persian Gulf Water (PGW) which is one of the most saline waters in the world. The main formation regions are found to be the shallow parts in the north and south (Reynolds, 1993; Kämpf and Sadrinasab, 2006; Yao and Johns, 2010a; Pous et al., 2015). Average evaporation rates are found to be up to 2 m/yr (Ahmad and Sultan, 1991; Johns et al., 2003; Pous et al., 2015). This saline, thus dense, water is in exchange with the Gulf of Oman through the Strait of Hormuz. The resulting exchange flow can be described by an inverse estuarine circulation. The PGW flows out at the bottom which is compensated with an inflow of less saline Indian Ocean Surface Water (IOSW). The IOSW drives the surface circulation of the Persian Gulf that is strongly dependent on the heat flux. With a positive heat flux in spring and summer, meaning absorption of heat by the water, a seasonal thermocline establishes which reduces vertical mixing. This allows the IOSW to reach far west in summer along the Iranian coast. Due to persistent northwesterly winds, the surface circulation can adjust as shown in figure 1.2. It consists of one cyclonic part in the central Gulf and a separate circulation in the north. The cyclone in the central dissolves into smaller
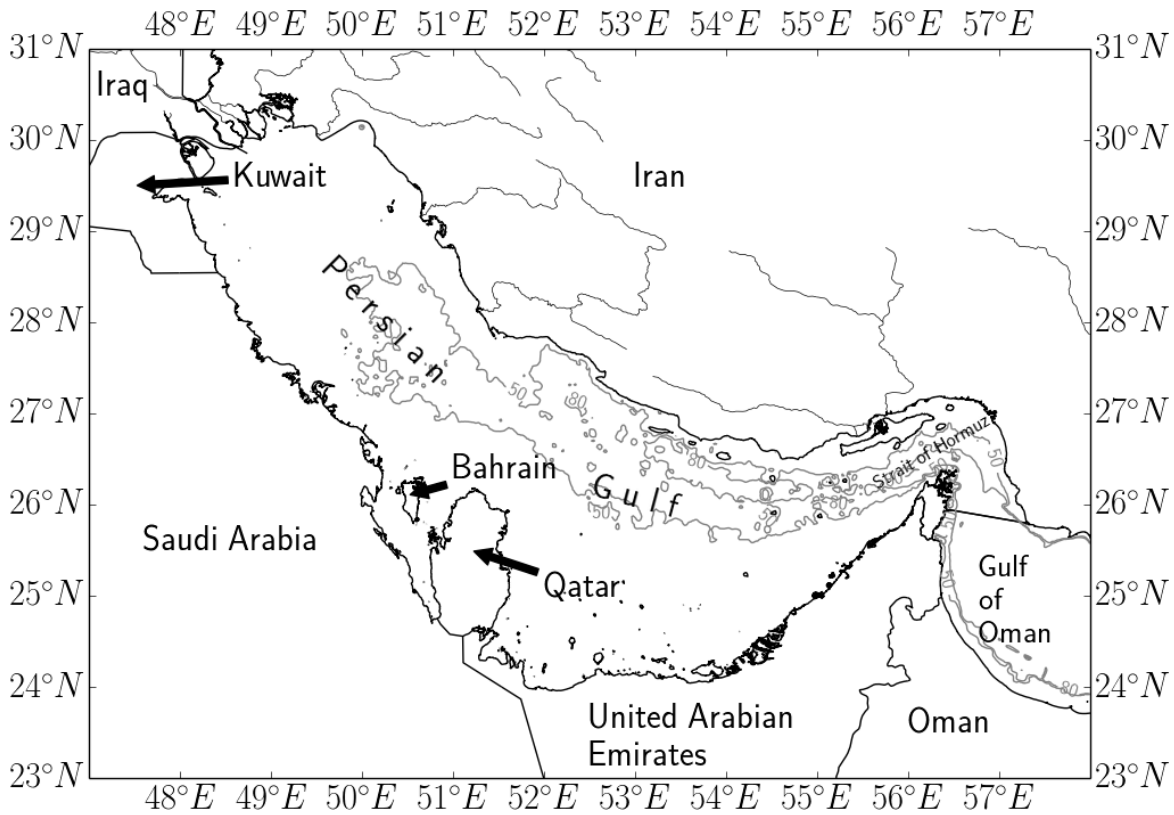
Figure 1.1.: Map of the Persian Gulf area. Coastlines generated with data from Claus et al. (2014).

eddies in fall (Kämpf and Sadrinasab, 2006; Yao and Johns, 2010b; Thoppil and Hogan, 2010) that subsequently dissipate during the winter months. Observational data of the circulation is spatially and temporally limited. The last coordinated gulf-wide measurement campaign was carried out during the Mt. Mitchell expedition in 1992 (Reynolds, 1993). Swift and Bower (2003) collected all available data to investigate the formation of PGW and the exchange flow.

Additional measurements were performed in the late 90s which focus on the exchange flow through the Strait of Hormuz (Johns et al., 2003; Pous et al., 2004). The exchange flow through the Strait of Hormuz has also been investigated in model studies of Yao and Johns (2010a); Pous et al. (2015). Johns et al. (2003) found that the bottom outflow is relatively stable with a mean transport of 0.15 ± 0.02 Sv and a mean salinity of 39.5 psu. Additionally, they found an outflow at the surface in the western part of the Strait of Hormuz (west coast of Oman) with 0.06 ± 0.02 Sv. The inflow is located in the northern part of the Strait with a transport of 0.23 Sv. Although measurements showed a constant exchange flow over the year (Johns et al., 2003), model studies
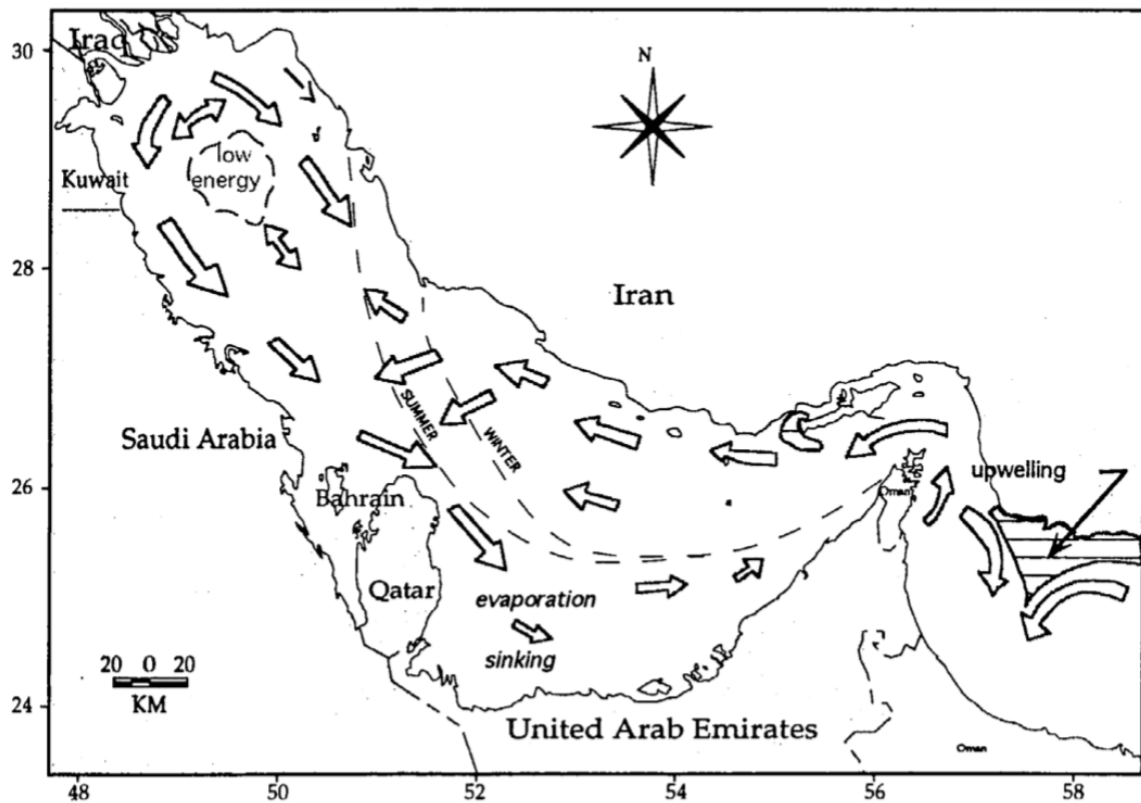
Figure 1.2.: Schematic of the surface circulation of the Persian Gulf by Reynolds (1993). The circulation consists of one cyclonic part east of Qatar and a south-east ward part in the north. The dashed lines show the estimate of the salinity front between the IOSW and the more saline water of the Persian Gulf.

suggest a seasonal cycle in the transport (Yao and Johns, 2010a). Pous et al. (2015) showed that the exchange flow can change from year to year.

A number of numerical studies have investigated the dynamics of the overturning circulation in recent years (Yao and Johns, 2010b,a; Pous et al., 2015) using realistic and high frequency forcing. With these high-resolution models the knowledge of the dynamics and the exchange flow of the Persian Gulf increased. The aim of this work is to create a realistic model of the Persian Gulf using GETM to analyse the exchange flow with the Total Exchange Flow theory. This and a higher vertical resolution using 40 layers of topography-following coordinates should give a more detailed insight into the exchange flow. Furthermore, the seasonal circulation and the formation of PGW will be discussed. The exchange flow is of special interest since the PGW could feed Indian Ocean intermediate or deep waters with long residence times, leading to a sequestration of atmospheric properties such as the greenhouse gas CO_2.

The outline of this work is the following: First, the governing equations of ocean dynamics and modelling are presented, as well as the description of estuarine circulation in general. Second, the used numerical model, GETM, and the model set-up of the Persian Gulf are shortly described. Third, the analysis of the model data is carried out before validating and discussing the results in comparison to other studies.

Chapter 2.

Theory

In this chapter the necessary basics to understand this work will be briefly presented. First, the three-dimensional shallow water equations are derived which suit the description of the oceans' hydrodynamics the best. Second, the boundary and tracer equations are presented that describe the oceans interaction with its boundaries, the atmosphere and the seafloor, as well as the evolution of temperature, salinity and other tracers, which could be suspended matter as well as zoo- or phytoplankton. Afterwards the theory of the dynamics and analysis of an estuary is presented.

2.1. Governing equations

2.1.1. Momentum equations

The most suitable equations to describe the hydrodynamics in the ocean are the three-dimensional shallow water equations. These are derived from the Navier-Stokes equations which for an incompressible fluid on a rotating frame can be written like this:

$$\rho \frac{D\mathbf{u}}{Dt} + 2\rho \mathbf{\Omega} \times \mathbf{u} = \rho \mathbf{g} - \nabla p + \nabla \cdot \left(\mu \nabla \mathbf{u} \right) + \mathbf{F}_{ext}, \tag{2.1}$$

$$\frac{D\rho}{Dt} = 0, \tag{2.2}$$

$$\nabla \cdot \mathbf{u} = 0 \tag{2.3}$$

where bold printed letters denote a three dimensional vector, $\frac{D}{Dt} = \frac{\partial}{\partial t} + \mathbf{u} \cdot \nabla$, $\mathbf{u}$ denotes the three dimensional velocity field with its components u, v, w in the directions x, y, z

with x being the zonal, y being the meridional and z being the vertical coordinate. ρ denotes the density, $\boldsymbol{\Omega}$ the Earth rotation, $\mathbf{g}$ the gravitational acceleration modified by the centrifugal force, p the pressure and μ the viscosity.

The first equation describes the change of momentum due to Coriolis force, gravitational force, pressure gradient, viscous forces and external forces. The second equation describes the conservation of mass and the third equation the incompressibility of the fluid.

Typically further assumptions and approximations are made to simplify these equations. The Boussinesq approximation makes use of the fact, that density changes in the ocean are small compared to the mean density itself. It uses an ansatz for the density:

$$\rho(x, y, z, t) = \rho_0(z) + \hat{\rho}(x, y, z, t), \qquad \rho_0 \gg \hat{\rho}, \qquad (2.4)$$

$$p(x, y, z, t) = p_0(z) + \hat{p}(x, y, z, t), \qquad p_0 \gg \hat{p} \quad , \qquad (2.5)$$

where ρ_0 and p_0 are the reference density/pressure and the hat variables the perturbations. By inserting (2.4) and (2.5) into (2.1), one can show that ρ is replaced in every term by ρ_0 except the buoyancy term, where the approximation error of $\mathcal{O}(\hat{\rho}/\rho_0)$ is assumed to be small and p is replaced by $\hat{p}$. This process of linearisation and ignoring external forces, equation (2.1) reduces to:

$$\frac{D\mathbf{u}}{Dt} + 2\boldsymbol{\Omega} \times \mathbf{u} = \frac{\hat{\rho}}{\rho_0}\mathbf{g} - \frac{1}{\rho_0}\nabla\hat{p} + \nabla \cdot \left(\nu\nabla\mathbf{u}\right) \qquad (2.6)$$

with $\nu = \mu/\rho_0$ being the kinematic viscosity.

Inserting (2.4) into the continuity equation (2.2), it reduces to the incompressibility equation (2.3) by assuming that the scales of the perturbation $\hat{\rho}$ on length and time are comparable to those of the velocity components (Haidvogel and Beckmann, 1999).

For most geophysical problems the solution of the Boussinesq equations (2.6) are complicated by the occurrence of turbulence which causes stochastic non predictable fluctuations. A way of dealing with these problems is the Reynolds decomposition. A flow variable X is decomposed into the mean part $\langle X \rangle$, defined as the ensemble average of an infinite number of identical flow experiments, and a fluctuation X' so

that X can be written as:

$$X = \langle X \rangle + X' \quad .\tag{2.7}$$

The ensemble average, denoted by angular brackets, has the properties that an ensemble average of the fluctuating part vanishes, i.e. $\langle X' \rangle = 0$, and the ensemble average of the mean part is unchanged, $\langle\langle X \rangle\rangle = \langle X \rangle$. Further important properties can be shown:

1. Linearity:

$$\langle X + \lambda Y \rangle = \langle X \rangle + \lambda \langle Y \rangle, \qquad \lambda = \text{const.}\tag{2.8}$$

2. Derivatives and average commute:

$$\left\langle \frac{\partial X}{\partial x} \right\rangle = \frac{\partial \langle X \rangle}{\partial x}, \qquad \left\langle \frac{\partial X}{\partial t} \right\rangle = \frac{\partial \langle X \rangle}{\partial t}\tag{2.9}$$

3. Product average:

$$\langle X \langle Y \rangle \rangle = \langle X \rangle \langle Y \rangle\tag{2.10}$$

To obtain the Reynolds-averaged Navier-Stokes equations (RANS) one averages the Boussinesq equations (2.6) and uses the definition (2.7) for all flow variables and the properties from (2.8)-(2.10). The RANS read as:

$$\frac{D\langle \mathbf{u} \rangle}{Dt} + 2\mathbf{\Omega} \times \langle \mathbf{u} \rangle = \frac{\langle \hat{\rho} \rangle}{\rho_0}\mathbf{g} - \frac{1}{\rho_0}\nabla\langle \hat{p} \rangle + \nu\nabla \cdot \left(\nabla\langle \mathbf{u} \rangle - \mathcal{R} \right)\tag{2.11}$$

with $\mathcal{R}$ being the Reynolds stress tensor with the entries $\mathcal{R}_{ij} = \langle u_i' u_j' \rangle$. Further attempts to solve the Reynolds stress tensor by deriving an equation for $\langle u_i' u_j' \rangle$ only leads to higher momentum terms in the form of $\langle u_i' u_j' u_k' \rangle$ and so on. This is referred to as the closure problem of turbulence. In the following a parametrization will be used for the vertical, see equation (2.16) and section 2.1.2. The averaged incompressibility equation (2.3) reads as:

$$\frac{\partial \langle u \rangle}{\partial x} + \frac{\partial \langle v \rangle}{\partial y} + \frac{\partial \langle w \rangle}{\partial z} = 0 \quad .\tag{2.12}$$

Scale analysis of the governing equations (see appendix A) further shows that for the Persian Gulf the vertical momentum equation can be approximated by the hydrostatic equation:

$$\frac{\partial \langle \hat{p} \rangle}{\partial z} = -\langle \hat{\rho} \rangle g, \tag{2.13}$$

with g being the absolute value of **g**. Doing the same scale analysis (appendix A) as before for the x- and y-components of (2.11), one finds (A.4) and (A.5):

$$\frac{\partial \langle u \rangle}{\partial t} + \langle u \rangle \frac{\partial \langle u \rangle}{\partial x} + \langle v \rangle \frac{\partial \langle u \rangle}{\partial y} + \langle w \rangle \frac{\partial \langle u \rangle}{\partial z} - f \langle v \rangle = -\frac{1}{\rho_0} \frac{\partial \langle \hat{p} \rangle}{\partial x} - \frac{\partial}{\partial z} \langle u'w' \rangle, \tag{2.14}$$

$$\frac{\partial \langle v \rangle}{\partial t} + \langle u \rangle \frac{\partial \langle v \rangle}{\partial x} + \langle v \rangle \frac{\partial \langle v \rangle}{\partial y} + \langle w \rangle \frac{\partial \langle v \rangle}{\partial z} + f \langle u \rangle = -\frac{1}{\rho_0} \frac{\partial \langle \hat{p} \rangle}{\partial y} - \frac{\partial}{\partial z} \langle v'w' \rangle \tag{2.15}$$

where f is the Coriolis parameter defined by $f = 2\Omega \sin(\phi)$ with the latitude ϕ. The equations are called the shallow water equations since the scale analysis is based on the assumption that the ocean/sea is shallow, meaning that the horizontal length scale L is far greater than the vertical length scale H, $L \gg H$. Compared to the RANS (2.11) one sees that all molecular diffusion terms are neglected as well as the horizontal turbulent terms. To deal with the vertical turbulent terms $\langle u'w' \rangle$ and $\langle v'w' \rangle$ a parametrisation by introducing a turbulent diffusivity ν_t is used:

$$\langle u'w' \rangle = -\nu_t \frac{\partial \langle u \rangle}{\partial z}, \qquad \langle v'w' \rangle = -\nu_t \frac{\partial \langle v \rangle}{\partial z} \quad . \tag{2.16}$$

Since ν_t is not constant it has to be computed in a numerical model. A way of dealing with this turbulence closure is shown in section 2.1.2. In a numerical model large scale eddies that are smaller than the horizontal grid resolution of the model, in order to account for the mixing effects. This is done by adding new stress terms to the horizontal components of the shallow water equations. With these parametrisations the shallow water equations can be written as:

$$\frac{\partial \langle u \rangle}{\partial t} + \langle u \rangle \frac{\partial \langle u \rangle}{\partial x} + \langle v \rangle \frac{\partial \langle u \rangle}{\partial y} + \langle w \rangle \frac{\partial \langle u \rangle}{\partial z} - f \langle v \rangle = -\frac{1}{\rho_0} \frac{\partial \langle \hat{p} \rangle}{\partial x}$$
$$+ \frac{\partial}{\partial z} \left(\nu_t \frac{\partial \langle u \rangle}{\partial z} \right) + \frac{\partial}{\partial x} \left(2 A_H^M \frac{\partial \langle u \rangle}{\partial x} \right) + \frac{\partial}{\partial y} \left[A_H^M \left(\frac{\partial \langle v \rangle}{\partial x} + \frac{\partial \langle u \rangle}{\partial y} \right) \right],$$
(2.17)

$$\frac{\partial \langle v \rangle}{\partial t} + \langle u \rangle \frac{\partial \langle v \rangle}{\partial x} + \langle v \rangle \frac{\partial \langle v \rangle}{\partial y} + \langle w \rangle \frac{\partial \langle v \rangle}{\partial z} + f \langle u \rangle = -\frac{1}{\rho_0} \frac{\partial \langle \hat{p} \rangle}{\partial y}$$
$$+ \frac{\partial}{\partial z} \left(\nu_t \frac{\partial \langle v \rangle}{\partial z} \right) + \frac{\partial}{\partial y} \left(2 A_H^M \frac{\partial \langle v \rangle}{\partial y} \right) + \frac{\partial}{\partial x} \left[A_H^M \left(\frac{\partial \langle v \rangle}{\partial x} + \frac{\partial \langle u \rangle}{\partial y} \right) \right]$$
(2.18)

with A_H^M being the horizontal eddy viscosity. A_H^M is dependent of the numerical grid size of the model. It can be computed with a formula proposed by Smagorinsky (1963) depending on approximations done before.

The last step is the elimination of the pressure perturbation $\hat{p}$ from the shallow water equations (2.17) and (2.18) by finding an expression for $\hat{p}$. One integrates the hydrostatic equilibrium (2.13) vertically from a position z to the surface ζ and receives:

$$\langle \hat{p}(\zeta) \rangle - \langle \hat{p}(z) \rangle = - \int_z^\zeta g \langle \hat{\rho} \rangle dz' \quad . \tag{2.19}$$

Since the horizontal pressure gradients shall be eliminated, $\frac{\partial}{\partial x}$ is applied to (2.19). Using the Leibniz' rule of differentiation one finds:

$$\frac{\partial \langle \hat{p}(\zeta) \rangle}{\partial x} - \frac{\partial \langle \hat{p}(z) \rangle}{\partial x} = -g \int_z^\zeta \frac{\partial \langle \hat{\rho} \rangle}{\partial x} dz' - g \langle \hat{\rho}(\zeta) \rangle \frac{\partial \zeta}{\partial x} \quad . \tag{2.20}$$

The pressure at the surface $\hat{p}(\zeta)$ is set to the atmospheric pressure p_a. To eliminate the density, the buoyancy b is defined with:

$$b = -g \frac{\hat{\rho}}{\rho_0} = -g \frac{\rho - \rho_0}{\rho_0} \quad . \tag{2.21}$$

The new equation reads as:

$$-\frac{1}{\rho_0} \frac{\partial \langle \hat{p}(z) \rangle}{\partial x} = \int_z^\zeta \frac{\partial \langle b \rangle}{\partial x} dz' + \langle b(\zeta) \rangle \frac{\partial \zeta}{\partial x} - \frac{1}{\rho_0} \frac{\partial \langle p_a \rangle}{\partial x} \quad . \tag{2.22}$$

The contributions to the horizontal pressure gradient are the vertically integrated buoyancy gradient, the surface slope and the atmospheric pressure gradient. Analogously one can derive an equation for the y-direction. Inserting the found expressions for the pressure gradient terms into (2.14) and (2.15), the final horizontal momentum equations are the following:

$$
\frac{\partial \langle u \rangle}{\partial t} + \langle u \rangle \frac{\partial \langle u \rangle}{\partial x} + \langle v \rangle \frac{\partial \langle u \rangle}{\partial y} + \langle w \rangle \frac{\partial \langle u \rangle}{\partial z} - f \langle v \rangle = \int_z^\zeta \frac{\partial \langle b \rangle}{\partial x} dz' + \langle b(\zeta) \rangle \frac{\partial \zeta}{\partial x} - \frac{1}{\rho_0} \frac{\partial \langle p_a \rangle}{\partial x}
$$
$$
+ \frac{\partial}{\partial z} \left(\nu_t \frac{\partial \langle u \rangle}{\partial z} \right) + \frac{\partial}{\partial x} \left(2 A_H^M \frac{\partial \langle u \rangle}{\partial x} \right) + \frac{\partial}{\partial y} \left[A_H^M \left(\frac{\partial \langle v \rangle}{\partial x} + \frac{\partial \langle u \rangle}{\partial y} \right) \right],
$$
$$
\tag{2.23}
$$

$$
\frac{\partial \langle v \rangle}{\partial t} + \langle u \rangle \frac{\partial \langle v \rangle}{\partial x} + \langle v \rangle \frac{\partial \langle v \rangle}{\partial y} + \langle w \rangle \frac{\partial \langle v \rangle}{\partial z} + f \langle u \rangle = \int_z^\zeta \frac{\partial \langle b \rangle}{\partial y} dz' + \langle b(\zeta) \rangle \frac{\partial \zeta}{\partial y} - \frac{1}{\rho_0} \frac{\partial \langle p_a \rangle}{\partial y}
$$
$$
+ \frac{\partial}{\partial z} \left(\nu_t \frac{\partial \langle v \rangle}{\partial z} \right) + \frac{\partial}{\partial y} \left(2 A_H^M \frac{\partial \langle u \rangle}{\partial x} \right) + \frac{\partial}{\partial x} \left[A_H^M \left(\frac{\partial \langle v \rangle}{\partial x} + \frac{\partial \langle u \rangle}{\partial y} \right) \right] \quad .
$$
$$
\tag{2.24}
$$

2.1.2. Turbulence closure

A parametrisation to express vertical turbulent terms was carried out by the introduction of the turbulent diffusivity ν_t. In a numerical model ν_t is computed with

$$
\nu_t = c_\mu^4 \frac{k^2}{\epsilon}, \tag{2.25}
$$

where c_μ is a non-dimensional stability function, k the turbulent kinetic energy and ϵ the dissipation rate. k and ϵ are each calculated via a prognostic equation which includes production and dissipation terms. For a detailed description see Umlauf and Burchard (2005). In this study the used model GETM is coupled to the General Ocean Turbulence Model (GOTM) in which the turbulence closure is implemented (Burchard et al., 1999). In particular, ν_t is computed in GOTM and then used in GETM.

2.1.3. Boundary conditions

There exist two types of conditions at the boundaries that must be satisfied at all times depending on the flow kinematics and the material properties. The *kinematic boundary*

conditions are derived from kinematic argument that the fluid particles at the fluids' boundary stay there for all times. This has to be satisfied by all fluids, irrespective of their properties and read as:

$$w(\zeta) = \frac{\partial \zeta}{\partial t} + u(\zeta)\frac{\partial \zeta}{\partial x} + v(\zeta)\frac{\partial \zeta}{\partial y} + E - P \qquad \text{at the surface } z = \zeta(x,y,t), \qquad (2.26)$$

$$w(-H) = -u(-H)\frac{\partial H}{\partial x} - v(-H)\frac{\partial H}{\partial y} \qquad \text{at the bottom } z = -H(x,y). \qquad (2.27)$$

P is the precipitation- and E the evaporation rate in m/s. By integrating the continuity equation vertically from the bottom $-H$ to the surface ζ, using the Leibniz integration rule and (2.26) and (2.27) an equation for the surface elevation ζ is received:

$$\frac{\partial \zeta}{\partial t} = -\frac{\partial}{\partial x}\int_{-H}^{\zeta} u\, dz - \frac{\partial}{\partial y}\int_{-H}^{\zeta} v\, dz - (E - P) = -\frac{\partial}{\partial x}U - \frac{\partial}{\partial y}V - (E - P), \qquad (2.28)$$

where U and V are referred to as the horizontal transports. The *dynamic boundary conditions* apply for a viscous fluid and are based on the assumption that the particles at the boundary move with the velocity of the boundary. For the bottom boundary condition one sets

$$\mathbf{u} = \mathbf{0} \qquad \text{at } z = -H(x,y), \qquad (2.29)$$

which is corresponding a Dirichlet-type of boundary condition. Instead of the momentum itself, one can use the momentum flux to express similar von Neumann boundary conditions:

$$\nu_t \frac{\partial \mathbf{u}}{\partial n} = -\frac{\boldsymbol{\tau}^b}{\rho_0} \qquad \text{at } z = -H(x,y), \qquad (2.30)$$

$$\nu_t \frac{\partial \mathbf{u}}{\partial n} = -\frac{\boldsymbol{\tau}^s}{\rho_0} \qquad \text{at } z = -\zeta(x,y,t), \qquad (2.31)$$

with $\boldsymbol{\tau}^b$ and $\boldsymbol{\tau}^s$ being the bottom and surface momentum fluxes or stress tensors which denote the momentum fluxes into the fluid or exerted stresses, n being the normal outward vector, perpendicular on the boundaries.

2.1.4. Tracer equations

The density perturbation $\hat{\rho}$ from the background density ρ_0 appears in the momentum equations (2.23) and (2.24). In general the density is a function of conservative temperature Θ, the absolute salinity s and pressure p:

$$\rho = \rho(s, \Theta, p) \,. \tag{2.32}$$

Therefore an equation of state for the density is needed. For the computation of ρ, empirically derived high order polynomials, based on thermodynamic potentials are used, e.g. Feistel (2008) derived a Gibbs function for seawater. Until 2010 EOS-80 (UNESCO and SCOR, 1981) was the standard of computing the density which was 2010 replaced by TEOS-10 (McDougall and Barker, 2011) (`teos-10.org`). The latter is used in the present study.

The equation describing the budget of temperature is derived from the first law of thermodynamics (not shown here). Applying Boussinesq approximation, incompressibility, the Reynolds average and using eddy diffusivity coefficients, the temperature budget can be written as

$$\begin{aligned}
&\frac{\partial \langle \theta \rangle}{\partial t} + \langle u \rangle \frac{\partial \langle \theta \rangle}{\partial x} + \langle v \rangle \frac{\partial \langle \theta \rangle}{\partial y} + \langle w \rangle \frac{\partial \langle \theta \rangle}{\partial z} - \frac{\partial}{\partial x}\left(A_H^\theta \frac{\partial \langle \theta \rangle}{\partial x} \right) - \\
&\frac{\partial}{\partial y}\left(A_H^\theta \frac{\partial \langle \theta \rangle}{\partial y} \right) - \frac{\partial}{\partial z}\left((\nu_t^\theta + \nu^\theta) \frac{\partial \langle \theta \rangle}{\partial z} \right) = \frac{1}{\rho_0 C_p} \frac{\partial I(z - \zeta)}{\partial z} + Q_\theta,
\end{aligned} \tag{2.33}$$

with the horizontal eddy diffusivity A_H^θ, ν_t^θ the vertical eddy viscosity for temperature, ν^θ the molecular diffusivity. The first term on the right describes the shortwave radiation which is a source of heat. C_p is the specific heat capacity, $C_p = 4180\,\text{J}/(\text{kg}\,^\circ\text{C})$, and $I(z - \zeta)$ the shortwave radiation profile in the water in W/m^2 with $I(0) = I_0$ the surface shortwave radiation. Other sources or sinks are represented by the term Q_θ. Q_θ includes for example the absorption of longwave radiation, sensitive (temperature difference between water and atmosphere) and latent heat. The equation for salinity s reads analogous with Q_s being the term for sinks and sources:

$$\begin{aligned}
&\frac{\partial \langle s \rangle}{\partial t} + \langle u \rangle \frac{\partial \langle s \rangle}{\partial x} + \langle v \rangle \frac{\partial \langle s \rangle}{\partial y} + \langle w \rangle \frac{\partial \langle s \rangle}{\partial z} - \frac{\partial}{\partial x}\left(A_H^s \frac{\partial \langle s \rangle}{\partial x} \right) - \\
&\frac{\partial}{\partial y}\left(A_H^s \frac{\partial \langle s \rangle}{\partial y} \right) - \frac{\partial}{\partial z}\left((\nu_t^s + \nu^s) \frac{\partial \langle s \rangle}{\partial z} \right) = Q_s \quad .
\end{aligned} \tag{2.34}$$

Similarly, the equation for any other tracer can be written, e.g. suspended matter, phytoplankton, nutrients, chemical concentrations etc., with a concentration C and a settling velocity w_s:

$$\frac{\partial \langle C \rangle}{\partial t} + \langle u \rangle \frac{\partial \langle C \rangle}{\partial x} + \langle v \rangle \frac{\partial \langle C \rangle}{\partial y} + (\langle w \rangle - w_s)\frac{\partial \langle C \rangle}{\partial z} - \frac{\partial}{\partial x}\Big(A_H^C \frac{\partial \langle C \rangle}{\partial x}\Big) - \\ \frac{\partial}{\partial y}\Big(A_H^C \frac{\partial \langle C \rangle}{\partial y}\Big) - \frac{\partial}{\partial z}\Big((\nu_t^C + \nu^C)\frac{\partial \langle C \rangle}{\partial z}\Big) = Q_C \quad . \tag{2.35}$$

It should be noted that the eddy diffusivities for temperature, salt and other tracers do not differ in the scales as the molecular diffusivities do and therefore are often chosen to be the same ($\nu_t^s = \nu_t^\theta = \nu_t^C = \nu_t$, $A_H^s = A_H^\theta = A_H^C = A_H$).

Boundary conditions for temperature and salinity

Similar to the boundary conditions for the momentum equations one needs to define boundary conditions for the temperature and salinity. Especially the surface boundary is the one of interest. For temperature sensitive Q_S, latent Q_l and long-wave Q_b heat fluxes ($[Q] = \text{W/m}^2$) have to be included:

$$\nu_t^\theta \frac{\partial \langle \theta \rangle}{\partial z}\Big|_{z=\varsigma} = \frac{Q_S + Q_l + Q_b}{\rho_0 C_p}, \tag{2.36}$$

with the different heat fluxes

$$Q_S = C_S \rho_{air} C_p \Big(\theta|_{z=\varsigma} - \theta_{air}\Big)u_{10}, \tag{2.37}$$

$$Q_l = -L\rho_0 E, \tag{2.38}$$

$$E = C_E \frac{\rho_{air}}{\rho_0}\Big(q_s - q\Big)u_{10}, \tag{2.39}$$

with C_S being the bulk transfer coefficient of sensible heat, ρ_{air} the air density, θ_{air} the air temperature, u_{10} the wind velocity in 10 m height, L ($[L] = \text{J/kg}$) the specific latent heat of water, E the evaporation rate as used before, C_E the bulk transfer coefficient of water vapour, q_s the saturated specific humidity at water temperature and q ($[q] = \text{g/kg}$) the specific humidity in the atmosphere. The bulk coefficients are calculated after Kondo (1975). The formula for Q_b is more complicated. Since it includes long-wave radiation, the water emits as well as it absorbs radiation from the atmosphere and therefore not shown here.

The diffusive salinity flux at the surface is given by Beron-Vera et al. (1999) with

$$\nu_t^s \frac{\partial \langle s \rangle}{\partial z}\bigg|_{z=\zeta} = (E - P)s_{surf} \, .$$

(2.40)

It describes the salinity change due to evaporation and precipitation at the water surface.

2.2. Estuarine circulation

2.2.1. Description of the estuarine circulation

An estuary describes a semi-enclosed transition area from fresh water to saline water, for example where a river connects to the open ocean. Examples for this kind of estuary are the Elbe River (Burchard and Baumert, 1998) or the Hudson River (Geyer et al., 2000; Ralston et al., 2008). An inverse estuary in contrast describes the transition zone from an area with a high evaporation rate (which increases the salinity) to the open ocean. An example for this is the Spencer Gulf in Australia (Nunes and Lennon, 1986) or on larger scales the Persian Gulf (Johns et al., 2003; Yao and Johns, 2010a).

To understand the drivers of the dynamics in an estuary the physical 1-D problem is considered. Equation (2.23) is simplified by neglecting horizontal velocity gradients, the Earths' rotation and the atmospheric pressure gradient. Dropping the angles from the Reynolds averaging one ends up with:

$$\frac{\partial u}{\partial t} - \frac{\partial}{\partial z}\left(\nu_t \frac{\partial u}{\partial z}\right) = \int_z^\zeta \frac{\partial b}{\partial x} dz' - g \frac{\partial \zeta}{\partial x} \, .$$

(2.41)

It can be seen that the velocity profile is dependent on the vertical turbulent diffusion term, the internal pressure gradient caused by the buoyancy gradient and the external pressure gradient which is caused by a tilt in the surface. Since the buoyancy gradient is dependent on salinity and temperature, one can already see the importance of fresh water and heat fluxes which change the salinity and temperature. The equation can be further simplified by assuming the internal buoyancy gradient is constant for all depths:

$$\frac{\partial u}{\partial t} - \frac{\partial}{\partial z}\left(\nu_t \frac{\partial u}{\partial z}\right) = z \frac{\partial b}{\partial x} - g \frac{\partial \zeta}{\partial x} \, .$$

(2.42)

For the temporally tidal mean velocity $\hat{u}$, the dynamic equation can be written like:

$$-\frac{\partial}{\partial z}\left(\nu_t \frac{\partial \hat{u}}{\partial z}\right) = z\frac{\partial b}{\partial x} - g\frac{\partial \hat{\zeta}}{\partial x}, \qquad (2.43)$$

where $\hat{\zeta}$ is the tidal mean surface elevation. An analytical solution to equation (2.43) is derived by Hansen and Rattray Jr (1966), see also MacCready and Geyer (2010), for a constant turbulent diffusivity ν_t and assuming no wind stress:

$$\hat{u}(z) = \left[8\left(\frac{z}{H}\right)^3 + 9\left(\frac{z}{H}\right)^2 - 1\right]u_e - \frac{3}{2}\left[\left(\frac{z}{H}\right)^2 - 1\right]u_r \qquad (2.44)$$

where the exchange flow intensity, $u_e = \frac{\partial_x b H^3}{48 \nu_t}$, and the residual run off u_r, $u_r = \langle \frac{1}{H}\int_{-H}^{\zeta} u(z)\,dz\rangle$, are defined, with $\langle\rangle$ denoting the tidal average. u_r is a measure for the fresh water flux, Q_F. The solution is strongly dependent on u_e and u_r and shows the importance of the heat and fresh water flux, which act as the main drivers for the estuarine circulation. The resulting velocity profile of equation (2.44) is shown in figure 2.1. On the left panel the velocity profile of the classical estuarine circulation is shown with an outflow at the surface and an inflow at the bottom. On the right panel the buoyancy gradient $\partial_x b$ was reversed as well as u_r to fit the conditions of an inverse estuary. The right profile shows that the velocities switch their signs and the inflow is now at the surface and the outflow at the bottom.

A more general solution of equation (2.42), however not shown here, is given by Burchard and Hetland (2010), where also the influence of wind stress and a parabolic eddy diffusivity profile is considered. To derive an analytical expression for the velocity profile, the buoyancy gradient and the turbulent diffusivity were set to a constant value for the whole water column. But in general both are not constant. For the 1-D problem the evolution of buoyancy b can be described by:

$$\frac{\partial b}{\partial t} + u\frac{\partial b}{\partial x} - \frac{\partial}{\partial z}\left(\nu_t \frac{\partial b}{\partial z}\right) = 0. \qquad (2.45)$$

Analogous to the surface boundary conditions for salinity and temperature, one can describe the surface boundary by the introduction of the surface buoyancy flux B_0:

$$-B_0 = \nu_t \frac{\partial b}{\partial z}\Big|_{z=\zeta} = g\frac{\alpha}{\rho_0 C_p}Q_{net} + g\beta s_{surf}(P - E), \qquad (2.46)$$

with the net heat flux at the surface Q_{net}, $Q_{net} = I_0 + Q_S + Q_l + Q_b$, the thermal expansion coefficient α, $\alpha = 2\cdot 10^{-4}\text{K}^{-1}$ and the haline contraction coefficient β, $\beta = 8\cdot 10^{-4}\text{kg g}^{-1}$.
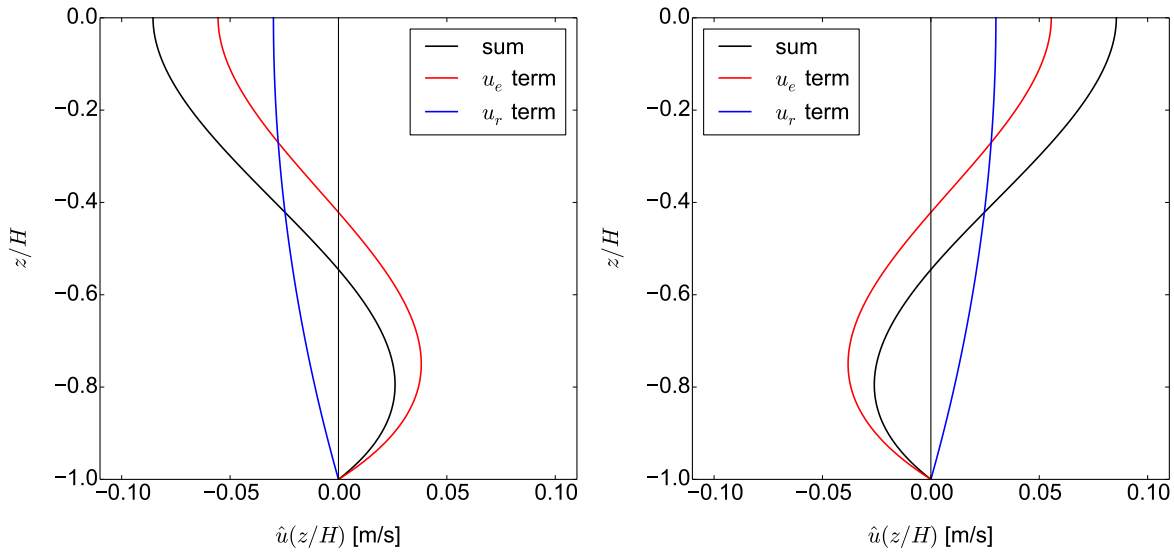
Figure 2.1.: Velocity profiles of the solution for $\hat{u}$ in equation (2.44) for $H = 20$m, $\nu_t = 3 \cdot 10^3$m^{2}s^{-1}, $\partial_x b = 10^{-6}$s^{-2} and $u_r = 0.02$m s^{-1} on the left which corresponds to the classical estuarine circulation with an outflow at the surface and an inflow at the bottom. On the right the sign of $\partial_x b$ and u_r is changed to imitate the conditions of an inverse estuary. The resulting velocity profile shows that the inflow is now at the surface and the outflow at the bottom.

It describes the change of buoyancy due to the net heat flux and fresh water flux at the surface. To conclude, the main drivers of the estuarine circulation are: the heat flux Q_{net} which influences the buoyancy, the fresh water flux Q_F which determines the internal buoyancy gradient as well as u_r, and the surface slope which creates the external pressure gradient.

In figure 2.2 all discussed drivers and the resulting circulation patterns for a classical and an inverse estuary are shown with the ocean being on the left and a river mouth on the right. The classical estuarine circulation can be solely driven by a fresh water flux of a river, but in general the surface buoyancy flux B_0 is not negligible. In this case B_0 is negative (downward) due to warming or precipitation and amplifies the stratification. The external pressure gradient is typically seaward since the surface elevation at the river mouth is higher than at the open ocean. If there is vertical mixing, e.g. due to tides, the isopycnals are typically tilted and the density gradient is landward as shown in figure 2.2a, which creates the well-known classical estuarine circulation pattern of an inflow of dense water at the bottom and an outflow of fresh water at the surface.

In figure 2.2b the circulation of the inverse estuary is shown. The surface buoyancy flux is positive (upward), resulting in a destabilisation of the water column due to

evaporation or cooling, and the Q_R is typically negligible. The external pressure gradient is landward because of evaporation which is lowering the sea level. The destabilisation creates vertical mixing because dense water is stratified over less dense water. Therefore, tides are not necessarily needed to homogenise the water column. The resulting density gradient is seaward and therefore the circulation pattern is inverse compared to the classical estuarine circulation.
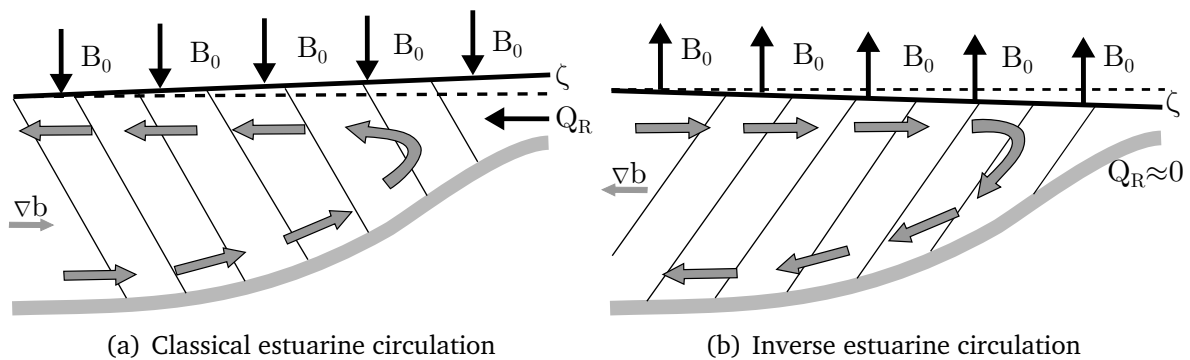

(a) Classical estuarine circulation   (b) Inverse estuarine circulation

Figure 2.2.: Schematic of the two circulation types in an estuary driven by the surface buoyancy B_0, river fresh water flux Q_R and the surface tilt ζ. (a) The negative (downward) surface buoyancy flux B_0 due to precipitation or warming, and a freshwater flux Q_R lead to a classical estuarine circulation where dense water flows into the estuary at the bottom and fresh water flows out of the estuary at the surface. (b) A positive (upward) surface buoyancy flux B_0 due to evaporation or cooling and a negligible river freshwater flux $Q_R \approx 0$ lead to an inverse estuarine circulation with flow directions in the opposite way. In addition, the current due to surface elevation flows in both cases in the same direction as the surface flow. Figures modified after Burchard and Badewien (2015).

2.2.2. Knudsen relations

Now that the drivers of the estuarine circulation are known one can look at tools which can be used to quantify the exchange flow. The first approach to describe the exchange flow of an estuary was done by Knudsen (1900) by using a simple two layer system and evaluating the volume and salinity budget. In this approach only the influence of salinity to the buoyancy is discussed. In figure 2.3 a visualisation of the idea is sketched. The upper layer with the salinity s_{out} is stratified over the bottom layer with the salinity s_{in}. Additionally, the volume fluxes in and out of the estuary are shown. The first

budget is the volume budget:

$$\frac{\partial V}{\partial t} = Q_{in} - Q_{out} + Q_F, \tag{2.47}$$

where Q_{out} is the outflow, Q_{in} the inflow, Q_F the freshwater flux, being the sum of the fluxes of river input Q_R, precipitation P and evaporation E:

$$Q_F = Q_R + P - E. \tag{2.48}$$

The second budget is the salinity budget:

$$V\frac{\partial s_a}{\partial t} = F_{in} - F_{out} = Q_{in}s_{in} - Q_{out}s_{out}, \tag{2.49}$$

where s_{in} and s_{out} are defined by the ratio of salinity flux F to volume flux Q:

$$s_{in} = \frac{F_{in}}{Q_{in}} = \frac{\int_{A_{in}} s\,\mathbf{u}\,d\mathbf{A}}{\int_{A_{in}} \mathbf{u}\,d\mathbf{A}}, \qquad s_{out} = \frac{F_{out}}{Q_{out}} = \frac{\int_{A_{out}} s\,\mathbf{u}\,d\mathbf{A}}{\int_{A_{out}} \mathbf{u}\,d\mathbf{A}}. \tag{2.50}$$

A_{in} and A_{out} denote the cross section area of the in- and outflow. The salinity budget describes the change of average salinity s_a of the whole estuary with its volume V. The change is driven by the difference of out- and inflowing salinity fluxes F. Taking a long-term mean of the two budgets yields to:

$$\langle Q_{in} \rangle - \langle Q_{out} \rangle + \langle Q_F \rangle = 0, \tag{2.51}$$

and

$$\langle Q_{in} \rangle \langle s_{in} \rangle^* - \langle Q_{out} \rangle \langle s_{out} \rangle^* = 0, \tag{2.52}$$

where $\langle\rangle$ denote the temporal averaging. Both equations can be combined to the Knudsen relations:

$$\langle Q_{out} \rangle = \frac{\langle s_{in} \rangle}{\langle s_{in} \rangle - \langle s_{out} \rangle}\langle Q_F \rangle, \qquad \langle Q_{in} \rangle = \frac{\langle s_{out} \rangle}{\langle s_{in} \rangle - \langle s_{out} \rangle}\langle Q_F \rangle. \tag{2.53}$$

$$*: \qquad \langle s_{in} \rangle = \frac{\langle F_{in} \rangle}{\langle Q_{in} \rangle} \neq \left\langle \frac{F_{in}}{Q_{in}} \right\rangle, \qquad \langle s_{out} \rangle = \frac{\langle F_{out} \rangle}{\langle Q_{out} \rangle} \neq \left\langle \frac{F_{out}}{Q_{out}} \right\rangle$$

The in- and outgoing volume fluxes can be calculated just by knowing the salinities of the in and out flowing currents plus the knowledge of freshwater input.
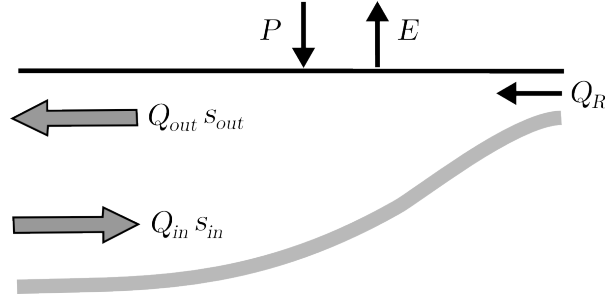

Figure 2.3.: Simple sketch to visualize the volume fluxes and the estuarine circulation after Knudsen (1900).

2.2.3. Total exchange flow (TEF) theory

A more detailed approach to analyse the exchange flow was proposed by MacCready (2011) extending the idea of Knudsen (1900). The idea is to compute the tidally averaged salt flux through a cross section by using salinity instead of spatial position as a coordinate. He defines the tidally averaged volume flux with salinity greater than s as the isohaline transport function $Q(x, s, t)$:

$$Q(x, s, t) \equiv \left\langle \int_{A_s} u(x, t) \, dA \right\rangle, \tag{2.54}$$

with $u(x, t)$ being the velocity perpendicular to the cross section at position x and time t, A_s the part of the cross section with salinities greater than s and $\langle \rangle$ denote a time average. With the definition of Q it follows that $Q(s_{max}) = 0$ and $Q(0) = Q_F$.

The TEF is defined by the following integrals:

$$Q_{in} \equiv \int -\left.\frac{\partial Q}{\partial s}\right|_{in} ds, \qquad\qquad Q_{out} \equiv \int -\left.\frac{\partial Q}{\partial s}\right|_{out} ds, \tag{2.55}$$

with 'in' meaning one only counts $-\frac{\partial Q}{\partial s}$ if it brings water into the estuary and 'out' respectively. The salt flux is therefore given by:

$$F_{in} \equiv \int s\left(-\frac{\partial Q}{\partial s}\right)\bigg|_{in} ds, \qquad\qquad F_{out} \equiv \int s\left(-\frac{\partial Q}{\partial s}\right)\bigg|_{out} ds. \tag{2.56}$$

With the introduction of flux-weighted salinities

$$s_{in} \equiv \frac{F_{in}}{Q_{in}}, \qquad s_{out} \equiv \frac{F_{out}}{Q_{out}}, \qquad (2.57)$$

the total salt conservation reads as:

$$\frac{\partial}{\partial t} \int s \, dV = Q_{in}s_{in} + Q_{out}s_{out} \qquad (2.58)$$

which corresponds to the salinity budget (2.49). Note that in MacCreadys' definition Q_{out} is negative, therefore the total salt and volume budget has opposite signs compared to the one in the Knudsen section. Figure 2.4 shows an example of the isohaline transport $Q(s)$ in black and its derivative $-\frac{\partial Q(s)}{\partial s}$ in red. The example data show the exchange flow of the cross section in the Strait of Hormuz for July 2010. The isohaline transport function denotes the transport of salinities greater than s, meaning that $Q(s = 36\text{g/kg}) = 0.022$ Sv (1 Sv = 10^6 m³/s) is the net inflow at the chosen cross section. This value should correspond to the volume net loss due to evaporation and river inflow in the Persian Gulf. Moving on to higher salinities, $Q(s)$ becomes negative showing that in higher salinities the outflow occurs. After reaching the maximum negative values $Q(s)$ becomes larger and eventually reaches 0 when s is greater than all salinities in the cross section. The in- and outflow can be seen more clearly when taking a look at the derivative $-\frac{\partial Q(s)}{\partial s}$, red line in figure 2.4. One can clearly identify in which salinity classes the transports are positive and negative. When computing the transports, salinity fluxes and salinities with equations (2.55-2.57) one gets the values:

$$Q_{in} = 0.219\,\text{Sv},$$
$$s_{in} = 37.14\,\text{g/kg},$$
$$Q_{out} = -0.197\,\text{Sv},$$
$$s_{out} = 39.06\,\text{g/kg}\,.$$

For this case of an inverse estuary a greater inflow with smaller salinity and a smaller outflow with greater salinity is found. Additionally, the sum of Q_{in} and Q_{out} is again 0.022 Sv as already found with $Q(s = 36\text{g/kg})$. Therefore, only $-\frac{\partial Q(s)}{\partial s}$ will be shown in the result section (see chapter 4) and referenced as a TEF-profile.
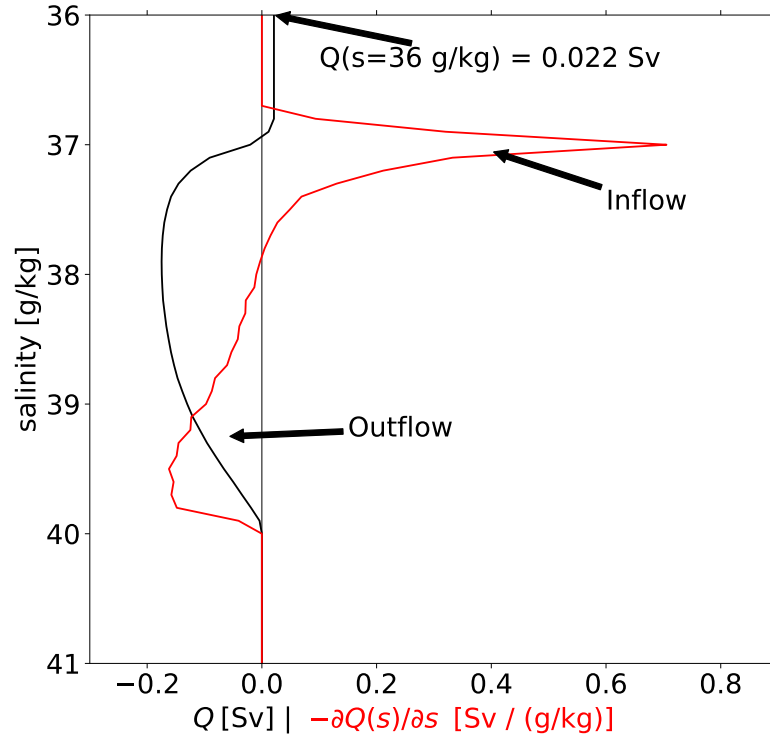
Figure 2.4.: Example for $Q(s)$ and $-\frac{\partial Q(s)}{\partial s}$.

2.2.4. Mixing in an estuary

Mixing plays an important role in an estuary. Vertical mixing is the reason that the horizontal density gradient can establish in the whole water column. There exist a number of different mixing mechanisms like entrainment which describes the mixing of a turbulent flow with ambient water (Turner, 1986) and boundary mixing which describes mixing induced by top and bottom frictional effects (Wunsch, 1970; Armi, 1978). These and additional effects contribute to the mixing in the ocean or in this case an estuary.

By multiplying equation (2.35), where the brackets are dropped for simplicity, $w_s = 0$ and the molecular diffusivity is neglected, with $2C$ one can derive an equation of the tracer variance C^2:

$$\frac{\partial C^2}{\partial t} + \frac{\partial u C^2}{\partial x} + \frac{\partial v C^2}{\partial y} + \frac{\partial w C^2}{\partial z} - \frac{\partial}{\partial x}\left(A_H^C \frac{\partial C^2}{\partial x}\right) - \frac{\partial}{\partial y}\left(A_H^C \frac{\partial C^2}{\partial y}\right) - \frac{\partial}{\partial z}\left(\nu_t \frac{\partial C^2}{\partial z}\right) = -\chi^{(C)},$$

$$(2.59)$$

where the physical mixing $\chi^{(C)}$ is defined:

$$\chi^{(C)} = 2\left[A_H^C\left(\frac{\partial C}{\partial x}\right)^2 + A_H^C\left(\frac{\partial C}{\partial y}\right)^2 + \nu_t\left(\frac{\partial C}{\partial z}\right)^2\right].\tag{2.60}$$

Burchard et al. (2017 in prep.) propose a simple estimate of the volume integrated mixing M of salinity, $M = \int_V \chi^{(s)}\,dV$, of an estuary by deriving an expression for the mixing M which is only dependent of the salinities s_{in}, s_{out} and the fresh water input by a river Q_R:

$$\langle M\rangle = \frac{\langle s_{out}\rangle\langle s_{in}^2\rangle - \langle s_{in}\rangle\langle s_{out}^2\rangle}{\langle s_{in}\rangle - \langle s_{out}\rangle}\langle Q_R\rangle,\tag{2.61}$$

where $\langle\rangle$ denote again temporal averaging. This approach takes advantage of the Knudsen relations which have been discussed before.

Chapter 3.

Model and set-up description

3.1. General Estuarine Transport Model

The General Estuarine Transport Model (GETM) originally developed by Burchard and Bolding (2002) is a three-dimensional coastal ocean model. It solves the equations (2.23), (2.24) to receive the horizontal velocity components and vertical integral of the continuity equation (2.12) to compute the vertical velocity component. With equation (2.33) for temperature and (2.34) for salinity the density is computed via TEOS-10 (McDougall and Barker, 2011) (`teos-10.org`) which then is used in the velocity equations again.

For large scale set ups, like the Persian Gulf, the model does not use Cartesian but spherical coordinates for all equations which changes the dependencies of flow variables from (x, y, z) to (λ, ϕ, z) with the longitude λ and the latitude ϕ (equations not shown here). For vertical coordinate transformation GETM can use a variety of different vertical coordinates: σ-coordinates (Phillips, 1957; Freeman et al., 1972), general vertical coordinates (gvc) (Burchard and Petersen, 1997) and adaptive coordinates (Burchard and Beckers, 2004; Hofmeister et al., 2010). The gvc allow a manual zoom to surface and bottom layers to achieve a higher resolution there. The adaptive coordinates zoom with respect to stratification. This allows a high vertical resolution where mixing is occurring, with the effect that numerical mixing, see section 3.1.1, is reduced (Klingbeil et al., 2014; Gräwe et al., 2015).

3.1.1. Numerical mixing

Using numerical models will create artificial mixing caused by discretisation errors in the advection terms. Burchard and Rennau (2008) introduced a way of classifying the numerical mixing by:

$$\chi^{(num)} = \frac{A\{C^2\} - (A\{C\})^2}{\Delta t},\tag{3.1}$$

where $A\{X\}$ describes the advection scheme of tracer X and Δt is the model time step between each computation of the advection term. The equation describes the difference between the advected tracer variance and the square of the advected tracer itself. Klingbeil et al. (2014) refined the analysis which allows the possibility to locate spatial and temporal points where strong mixing appears. These points can then be further investigated, e.g. whether physical (eq. (2.60)) or numerical mixing is the dominant process. GETM can provide both types of mixing with the tools introduced by Klingbeil et al. (2014).

3.2. Persian Gulf set up

The numerical set up of the Persian Gulf uses the ETOPO1 (Amante and Eakins, 2009) bathymetry with a resolution of one arc minute. Some modifications are applied, for example the minimum depth is set to 5 m to prevent drying and flooding and bathymetry points which are not connected to the Persian Gulf are excluded. The final bathymetry is shown in figure 3.1. GETM provides terrain following vertical coordinates, as described in section 3.1. For this set up 40 vertical levels using the general vertical coordinates (gvc) are chosen to provide a higher resolution at the surface and the bottom.

The model has to be forced by external data: by meteorological data for the surface fluxes, ocean data at the open boundary for temperature, salinity, velocity and elevation as well as inflow water from rivers which discharge into the Persian Gulf.

For the atmospheric forcing the ERA-Interim reanalysis data (Dee et al., 2011) which have a 80 km resolution is used and provides 3-hourly data of all necessary atmospheric parameters, see figure 3.2 for an exemplary distribution of temperature, pressure and winds.
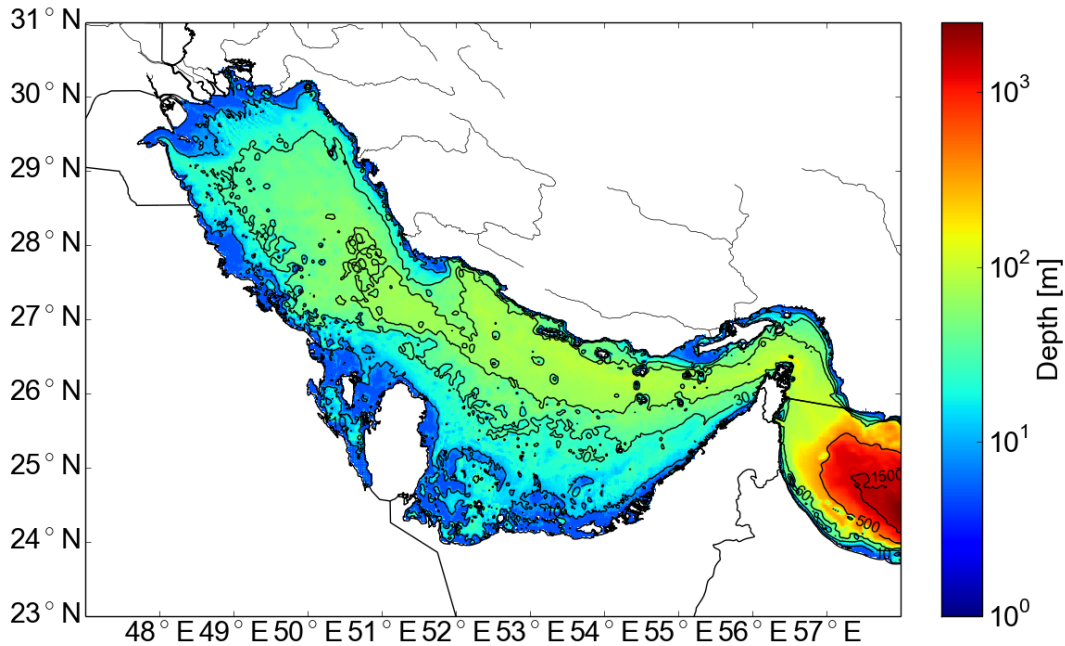
Figure 3.1.: Bathymetry of the Persian Gulf based on ETOPO1 (Amante and Eakins, 2009). Coastlines generated with data from Claus et al. (2014). The contour lines show the depth of 10, 30, 60, 500 and 1500 m.

For the open boundary data, results from the global HYCOM-model (Chassignet et al., 2007) are used which provides 3-hourly data with a spatial resolution of $1/12°$. In addition, the elevation for tides was added to the HYCOM-model using the OSU Tidal Prediction Software (OTPS) (Egbert and Erofeeva, 2002). The OTPS includes the M2, S2, N2, K2, K1, O1, P1 and Q1 tidal constituents.

For the river input data of monthly means for the four main rivers Arvand, Zohreh, Helleh and Mond (locations are shown with red dots in figure 3.3) are used, see table 3.1. Other rivers are not included since their input is only small and their influence of the Gulf wide dynamics is negligible.

Additionally, the surface of the Persian Gulf is marked with passive marker tracers to investigate where the dense deep water of the Persian Gulf is created. The tracer distribution is shown in figure 3.3. The tracer concentration in the surface is set to 1.0 for all time steps. Tracer T_1 marks the shallow region around Bahrain where the highest salinities in the Persian Gulf are found (John et al., 1990). Tracer T_2 and T_3 mark the shallow regions in the north and south which are found to be the main regions where the PGW is formed. T_4 marks the deeper northern parts and T_5 the western part where the IOSW should be dominant.
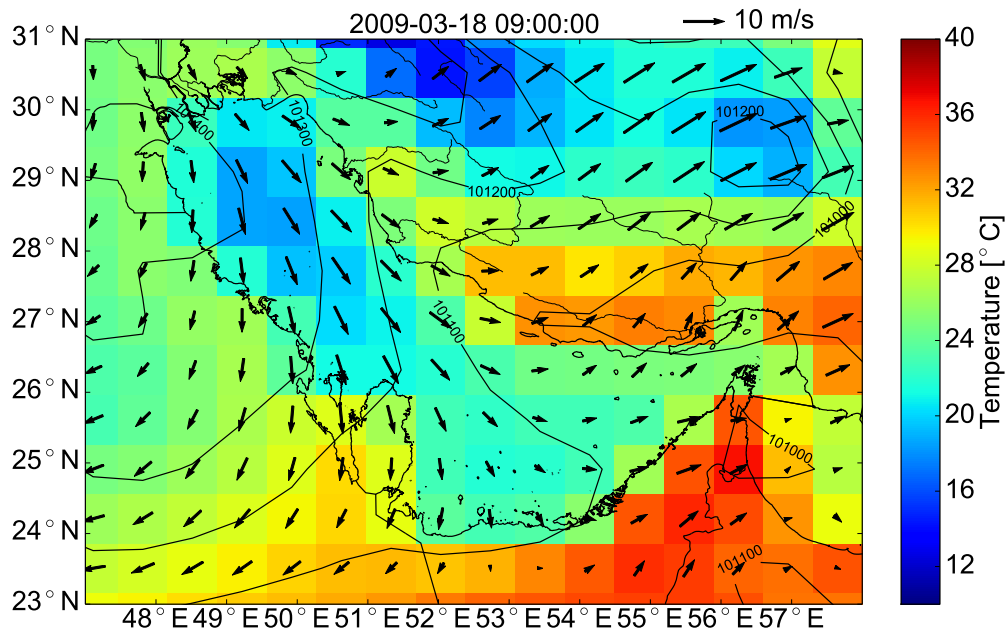
Figure 3.2.: Example of the atmospheric forcing data of the Persian Gulf area from ERA-Interim (Dee et al., 2011). The colors show the temperature in 2m height, the contour lines show the pressure isobars in Pa and the arrows the wind direction and speed in m/s.

The simulation period is two years, starting on 2009-01-01 00:00:00 and ending on 2011-01-01 00:00:00. The applied time step in the model is 5 s. The first year, 2009, functions as a spin-up year and only the second, 2010, is used for data analysis. The tracers are released after the spin-up year on 2010-01-01 00:00:00. Locations of transects used in the following and stations for tide comparison are shown in figure 3.4.

	Jan	Feb	Mar	Apr	May	Jun	Jul	Aug	Sep	Oct	Nov	Dec
Arvand [m³/s]	208.6	229.5	250.3	271.2	250.3	229.5	208.6	187.7	166.9	146.0	166.9	187.7
Zohreh [m³/s]	29.1	32.0	34.9	37.8	34.9	32.0	29.1	26.2	23.3	20.4	23.3	26.2
Helleh [m³/s]	63.6	70.0	76.3	82.7	76.3	70.0	63.6	57.2	50.9	44.5	50.9	57.2
Mond [m³/s]	198.7	218.6	238.5	258.3	238.5	218.6	198.7	178.8	159.0	139.1	159.0	178.8
Temperature [°C]	18.0	21.0	23.0	25.0	27.0	30.0	32.0	29.0	26.0	22.0	19.0	16.0

Table 3.1.: Used monthly mean transports in m³/s for the four biggest rivers in the Persian Gulf region. The listed temperatures are used for all rivers. The data were given to me by Jafar Azizpour who created the data after Kämpf and Sadrinasab (2006).
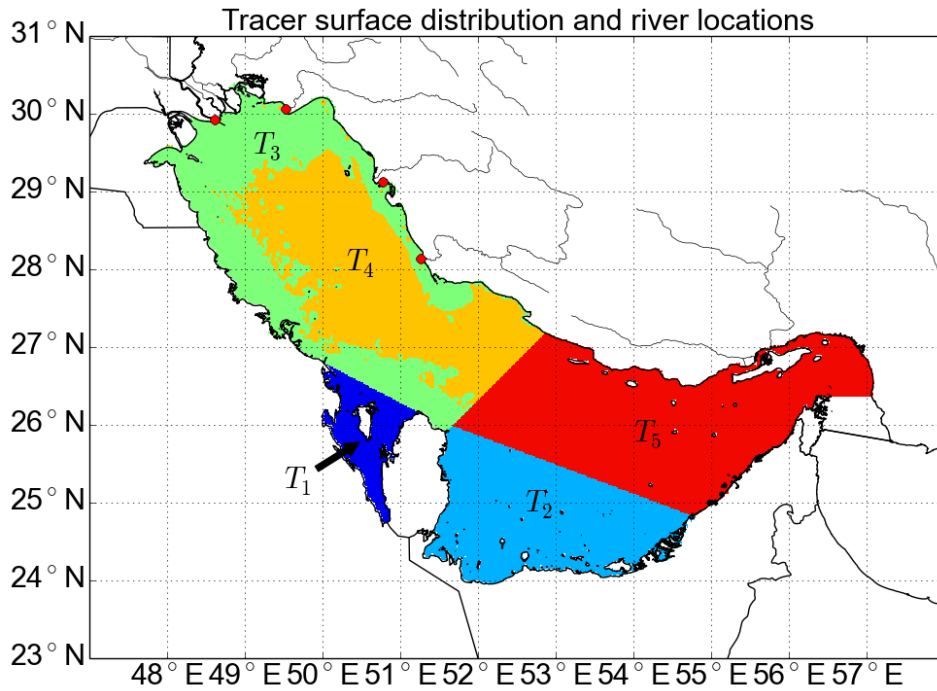
Figure 3.3.: Tracer distribution used to mark different surface areas of the Persian Gulf. The red dots show the locations of the included river mouths.
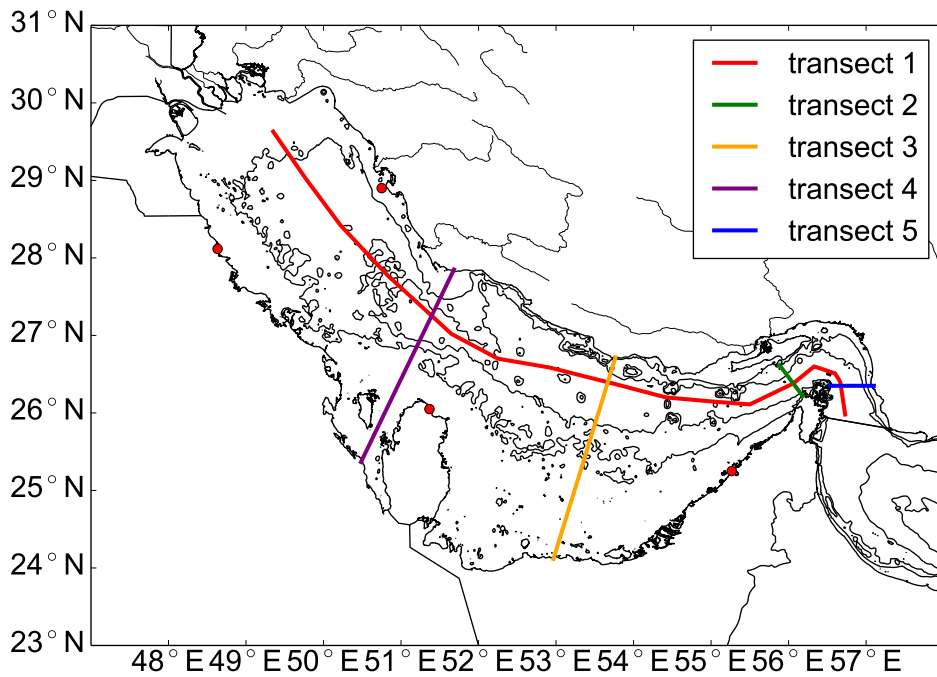

Figure 3.4.: Locations of the transects used in the following. The red dots show the stations which are used for tide comparison.

Chapter 4.

Results, validation and discussion

4.1. Sea surface temperature and tide comparison

4.1.1. SST comparison

For a first validation of the models' results the sea surface temperature (SST) is compared to observational data derived by the Observational Sea Surface Temperature and Ice Analysis (OSTIA) system (Stark et al., 2007; Donlon et al., 2012) which uses all available measurements to compute a global, high resolution temperature and ice coverage dataset. In addition, the SST of the HYCOM model is shown which this study uses to generate boundary conditions.

In figure 4.1 the daily mean SSTs of the first of June are shown. The SST of this study reproduces the spatial distribution of the observation fairly well. Furthermore, the temperatures are well reproduced in the north and central Persian Gulf. The temperatures at the southern coast and in the Strait of Hormuz are too warm and the cold water at the northern Iranian coast is too cold. The HYCOM model shows a better agreement for this day in the central Gulf and the Strait of Hormuz. However, the northern part is too cold.

In figure 4.2 the SSTs for a day in November are shown. The results of this study clearly show too high temperatures for this day in the whole Persian Gulf with a temperature plus of $\sim 2°C$ which can be clearly seen in the difference plot on the right. The spatial pattern with highest temperatures in the central Gulf is reproduced. The HYCOM model shows a very good agreement both in spatial distribution as well as in the values for temperature, not shown here.
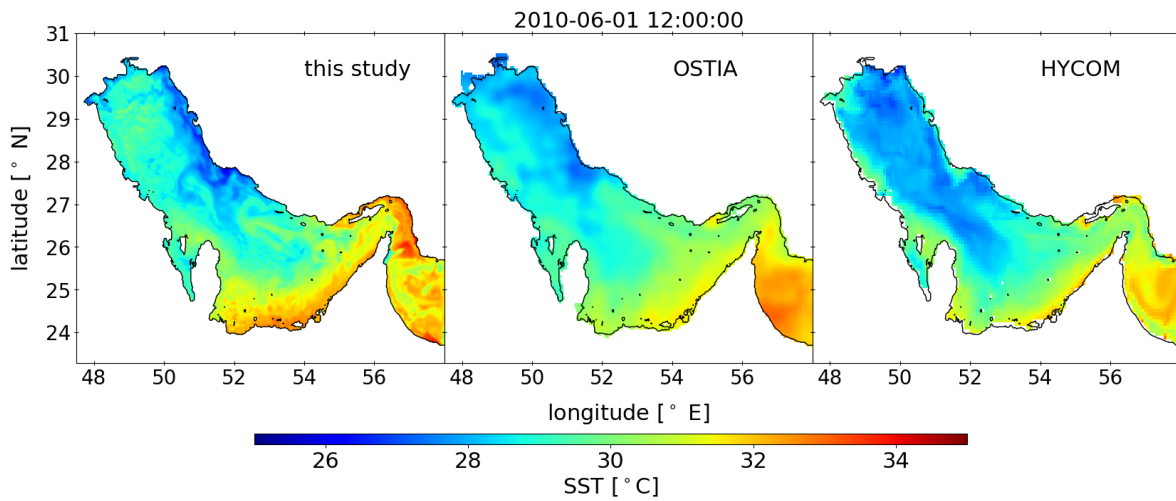
Figure 4.1.: Comparison of SST of this work (left), observational data derived by OSTIA (Stark et al., 2007; Donlon et al., 2012) (middle) and the HYCOM model which was used to generate boundary conditions (right) for a daily mean of the 24 h before the labelled date.

Without showing more comparisons, the SSTs of this study are in general too warm in the central and northern Persian Gulf with differences of ∼2°C and too cold in the shallow areas. The spatial distribution on the other hand is reproduced. The higher temperatures create smaller surface densities and also influence the heat fluxes between atmosphere and ocean which should be notable in the sensible heat flux Q_S. The SST of HYCOM shows good agreements with the OSTIA data. Therefore, the initial conditions
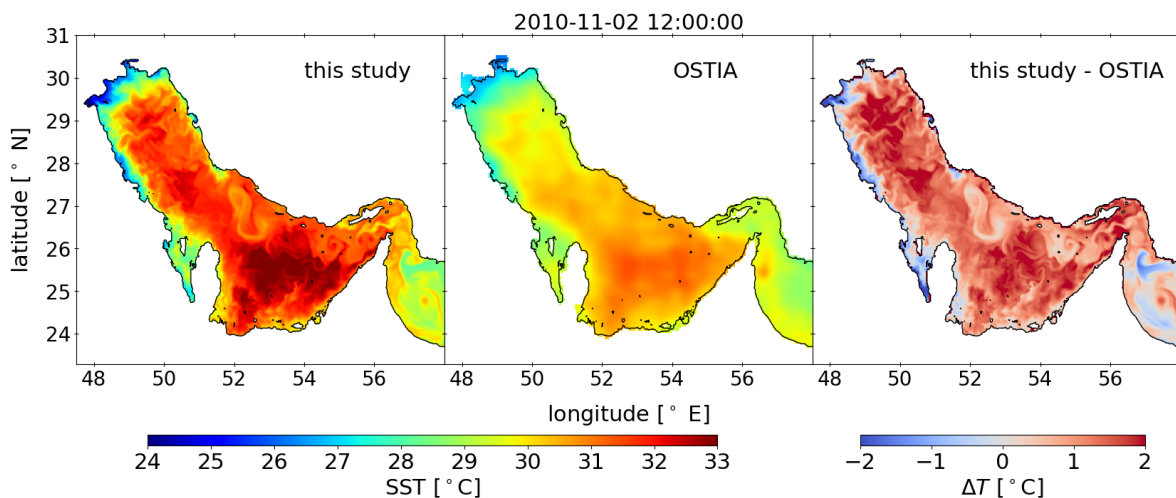
Figure 4.2.: Comparison of SSTs as in figure 4.1 but for another date and the difference between this study and OSTIA is shown on the right instead of the HYCOM results.

and boundary conditions used for this study cannot be a reason for the differences. Another possible reason is the heat flux which is discussed in detail in section 4.2.1.

4.1.2. Tide comparison

In table 4.1 a tide analysis has been carried out for four stations to validate the tidal amplitudes of this set up using the python module 'pytides' created by Sam Cox [1]. Tidal analysis have been performed by Pous et al. (2012) and Mashayekh Poul (2016) which have been used for validation. Comparing the semi-diurnal constituents, the M2 shows clear deviation in amplitude of a factor 1.5-2.5 whereas the S2, N2 and K2 agree better with observations. The diurnal constituents K1, O1 and P1 show similar errors in amplitude, especially in K1. Since all amplitudes seem too small, mixing induced by tides should be underestimated in the model as well. Concerning the phase shift, the tides in this model are lagging behind the observed tides. For the further analysis of this study, the phase shift should not matter for tidal mixing since only monthly or annual means are computed and discussed. It should be noted that the model is not tuned to reproduce the tides as the models used by Pous et al. (2012) and Mashayekh Poul (2016). The Kelvin wave is moving counterclockwise and therefore the stations are sorted counterclockwise as well. The deviations are greatest at the Dubai station and smallest at the Bushehr station. This indicates that the longer the Kelvin wave travels, the greater the errors become. A reason could be numerical errors which occur in the surface elevation equation (2.28). The resulting numerical mixing could decrease the amplitudes. In addition, the prescribed tides at the boundary were computed with a global model whose resolution could be not sufficient to fit the real tides in this region.

	Bushehr	28°54'N|50°45'E	Ras Al Mishaab	28°07'N|48°38'E	Jabal Fowarait	26°03'N|51°22'E	Dubai	25°15'N|55°16'E
	This study	Observations	This study	Observations	This study	Observations	This study	Observations
M2	23.9 | 123	34 | 110	17.2 | 326	25 | 276	17.9 | 56	42 | 44	25.9 | 245	44 | 237
S2	13.7 | 184	12 | 160	7.9 | 44	8 | 335	6.4 | 103	13 | 88	13.4 | 301	16 | 281
N2	6.9 | 96	7 | 84	5.0 | 287	6 | 243	6.2 | 27	11 | 17	7.7 | 222	10 | 217
K2	3.7 | 167	4 | 156	2.5 | 29	3 | 334	1.7 | 100	4 | 88	3.9 | 285	5 | 265
K1	16.7 | 257	31 | 223	21.2 | 303	35 | 259	11.7 | 90	20 | 54	8.9 | 137	23 | 91
O1	17.0 | 236	20 | 189	20.6 | 277	21 | 221	8.6 | 54	9 | 0	11.7 | 107	16 | 42
P1	4.8 | 249	9 | 218	5.8 | 294	13 | 253	2.9 | 82	7 | 54	2.8 | 118	7 | 77

Table 4.1.: Table of the dominant tidal constituents of the Persian Gulf for 4 stations, see figure 3.4. The results are given with amplitude [cm] | phase shift [°] compared to Greenwich. Observational data is listed by Pous et al. (2012) (table 1 and 2).

---

[1] https://github.com/sam-cox/pytides

4.2. Formation of the Persian Gulf's dense water

4.2.1. Heat fluxes and evaporation

The main reason for the formation of the Persian Gulf Water is the evaporation. It causes a loss of fresh water at the surface which is increasing the salinity content and therefore the density. This dense water sinks to the bottom and propagates from there towards the Strait of Hormuz and the Gulf of Oman. In winter the cooling of the surface contributes to the increasing density which is enhancing this process.

In figure 4.3 the monthly means of the different heat fluxes and the fresh water flux $P - E$ are shown. The surface shortwave radiation I_0 shows the typical seasonal course with its maximum in June and July. Note that the values shown include the nights, where $I_0 = 0$. The net heat flux shows positive values from February to September and negative values in the other months. Negative values correspond to heat- and therefore energy loss. Annual mean values for the different fluxes are found:

$$Q_{net} = 32.0\,\mathrm{W/m^2}, \tag{4.1}$$
$$I_0 = 250.4\,\mathrm{W/m^2}, \tag{4.2}$$
$$Q_l = -144.6\,\mathrm{W/m^2}, \tag{4.3}$$
$$Q_S = -4.6\,\mathrm{W/m^2}, \tag{4.4}$$
$$Q_b = -69.2\,\mathrm{W/m^2}. \tag{4.5}$$

Q_{net} differs significantly from an observational estimate: Q_{net} = -7.2 $\pm$ 4.4 W/m^2 (Johns et al., 2003) or a model result Q_{net} = -6.99 W/m^2 (Yao and Johns, 2010a). The reason for that is the overestimation of the shortwave flux of GETM. The Arabian peninsula is a region with tropospheric aerosols which lower the incoming shortwave radiation (Husar et al., 1997). This effect is not covered in this study. When Johns et al. (2003) compared their results with long term atmospheric data of the Comprehensive Ocean-Atmosphere Data Set (COADS) (Woodruff et al., 1993) the mean shortwave radiation was 248 W/m^2 which did not include aerosols. This is a comparable value as found in this study. With a corrected value by 37 W/m^2 using improvements by Tragou et al. (1999), the new shortwave radiation is 211 W/m^2. A reduction of 37 W/m^2 in I_0 would lead to Q_{net} of -5.0 W/m^2, assuming all other heat fluxes are unchanged, which is in the range of estimated heat fluxes. This overestimation of the heat flux should

be the main reason for the too high SSTs in section 4.1.1. For future simulations this correction should definitely be included to achieve better agreements to observations.

The absolute value of fresh water flux until June is smaller than in the second half of the year. A similar pattern was found by Yao and Johns (2010a). With an annual mean loss of fresh water of -1.79 m/yr, the resulting fresh water loss is ≈ -13800 m^3/s. This rate is in the range of confirmed evaporation rates (Ahmad and Sultan, 1991; Johns et al., 2003).
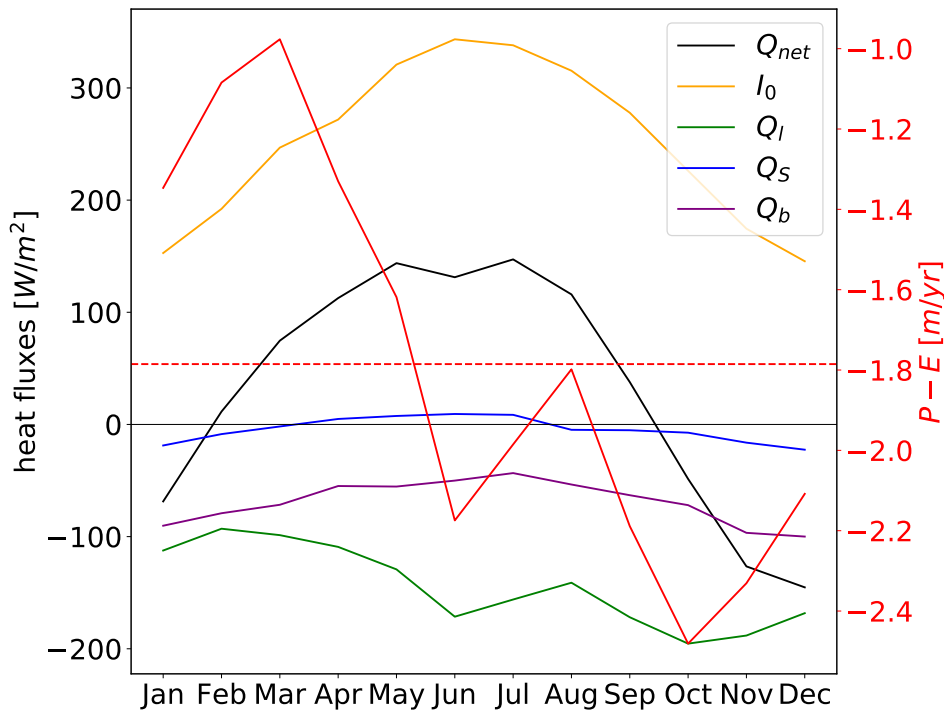
Figure 4.3.: Monthly means of the heat fluxes and fresh water flux $P - E$ for the year 2010: the net heat flux Q_{net}, the surface shortwave radiation I_0, the latent heat Q_l, the sensible heat Q_S and the longwave radiation Q_b. Positive values indicate that the Persian Gulf gains heat and negative values that there is a heat loss. The dashed red line shows the annual mean of $P - E = -1.79$ m/yr.

4.2.2. Regions that contribute to the formation of dense water

In figure 4.4 the spatial distribution of the annual mean fresh water flux in 2010 is shown. The smallest fresh water fluxes and therefore highest evaporation rates are found in the open and deeper northern part of the Persian Gulf whereas the shallow parts in the south show smaller evaporation rates. High evaporation indicates a high

generation rate of saline water which has the potential to become part of the dense outflowing Persian Gulf water. But the surface salinities in figure 4.6 show the highest salinities in the shallow parts of the Persian Gulf where smaller evaporation rates are found. The IOSW has a small salinity when entering the Gulf and its salinity steadily increases due to evaporation and mixing with ambient water on its way to the north. This leads to the higher surface salinities in shallow parts which are reached by the IOSW later than the region with high evaporation. Furthermore, the velocities in the shallow parts are smaller than in the deeper part, see figure 4.14 and 4.15, resulting in a longer residence time in those areas which increases the salinity as well. Since density is dependent on salinity, the shallow areas with high salinities are the regions where the densest water is created. The temperature contributes to density as well. The SST of the four seasons in shown on the left in figure 4.6. In all seasons except summer, the shallow regions have a lower SST than the surrounding deeper regions. Therefore, the highest densities in these regions are formed in winter, when the temperatures are the lowest. These regions are confirmed to be the main location of formation by several studies (Reynolds, 1993; Swift and Bower, 2003; Kämpf and Sadrinasab, 2006; Yao and Johns, 2010a) .
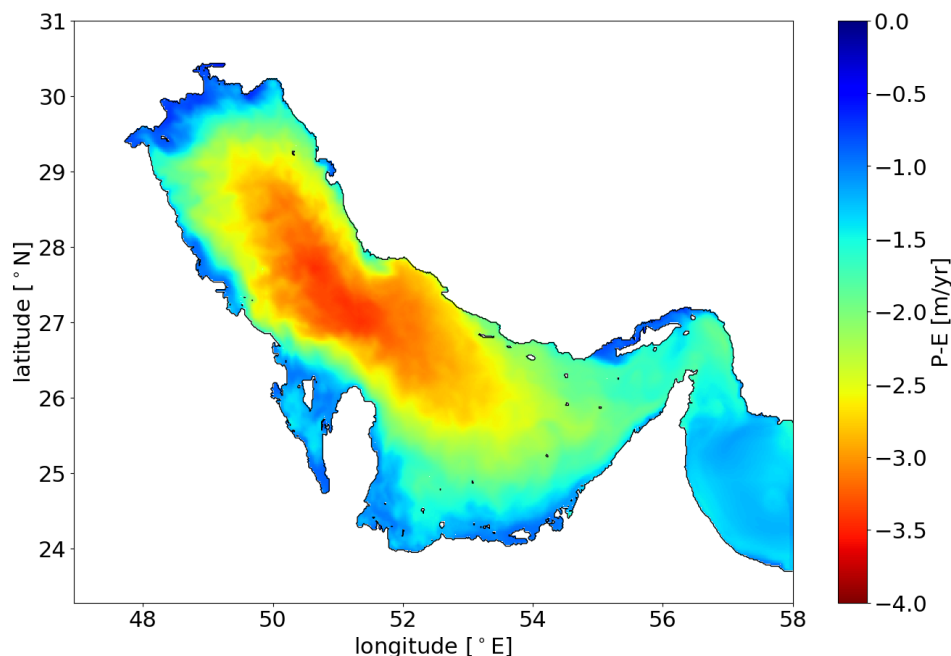
Figure 4.4.: Spatial distribution of the annual mean fresh water flux of 2010. The smallest fresh water fluxes, meaning high evaporation rates are found in the open and deep Persian Gulf in the north. The shallow regions in the north and south show smaller evaporation rates.
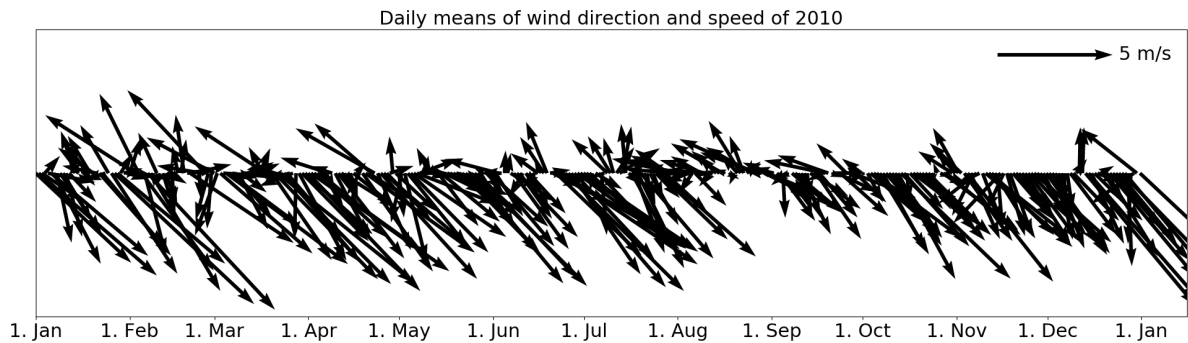
Daily means of wind direction and speed of 2010

→ 5 m/s

1. Jan 1. Feb 1. Mar 1. Apr 1. May 1. Jun 1. Jul 1. Aug 1. Sep 1. Oct 1. Nov 1. Dec 1. Jan

Figure 4.5.: Wind distribution of the Persian Gulf. The dominant winds are the northwesterlies.

The densest waters of the Persian Gulf are formed around Bahrain west of Qatar where salinities greater than 50 g/kg can be found (John et al., 1990) and temperatures become lowest, see figure 4.7. In winter months the density can become >38 kg/m^3, creating a strong density gradient towards the Persian Gulf. But as seen in the tracer distribution of that region, the spreading of the water of that region is rather slow. In figure 4.8 the first kilometers of the purple transect are shown. On the left, the distribution shows a vertically homogeneous salinity and a horizontal gradient towards the open sea. But the velocities do not necessarily point into the same direction which indicates that there must be a counteracting force. A reason for this could be an opposing Ekman transport which is working against the density gradient. The common wind direction in the Persian Gulf is to the southeast, see figure 4.5, where wind directions and speeds are shown as daily means for the whole Persian Gulf. With this the Ekman transport is towards southwest and counteracts the density gradient. Furthermore, increased friction due to a vertical mixing caused by evaporation and therefore by the surface buoyancy flux hinder the exchange flow in this region. The water leaving the shallows around Bahrain is almost immediately mixed with less dense water as shown in figure 4.8. The total mixing shows high values in that area where the outflow is occurring. The bottom distribution in figure 4.7 supports this thesis since there are no high concentrations of tracer T_1 found. Therefore, this region definitely creates dense water but is only a minor contribution to the PGW. A similar result was found by Kämpf and Sadrinasab (2006).

Staying in this region, the bottom distributions of the other tracers in figure 4.9 and 4.10 show only small concentrations, whereas just north of Bahrain the concentrations are close to unity. As already seen before, this region is vertically homogeneously mixed, such that the exchange of this region with the Persian Gulf is restricted.
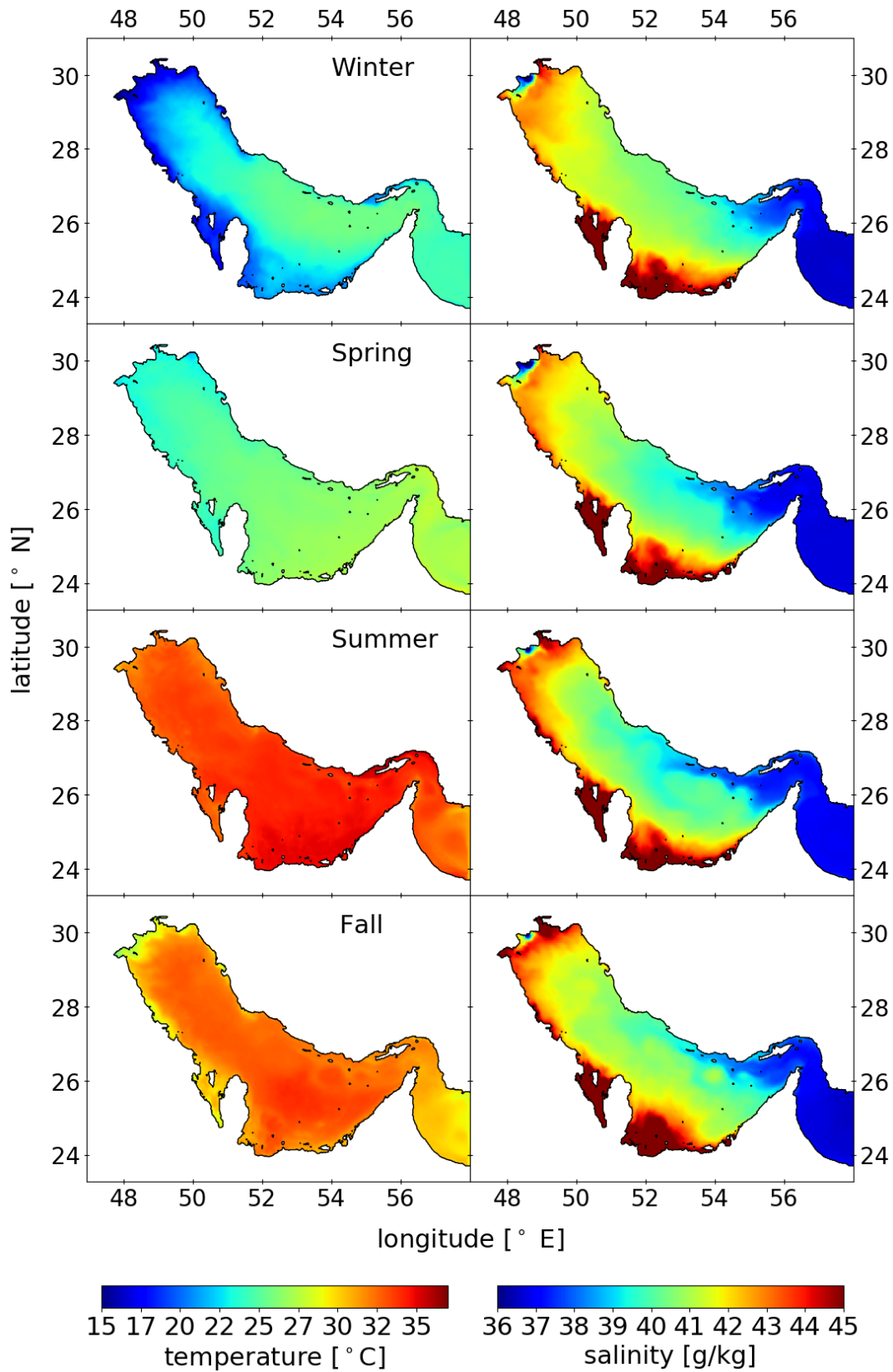
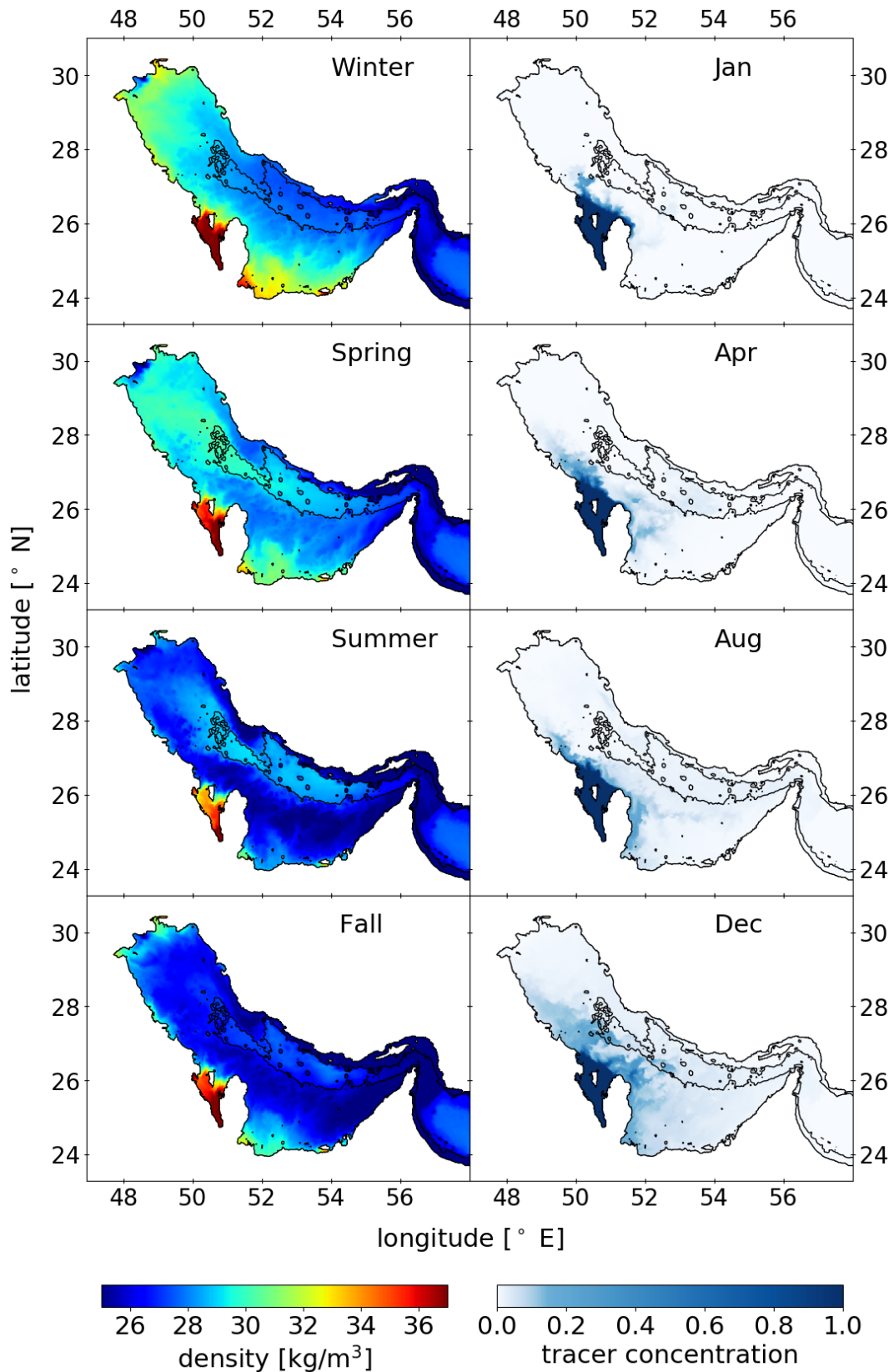**Figure 4.6.:** Seasonal means for SST (left) and surface salinity (right) for 2010.

Figure 4.7.: Seasonal means of the bottom density (left) and the bottom spatial distribution of tracer T_1 (right) for 2010. The tracer distributions display the conditions at the end of the labelled months. The contour shows 60m depth.
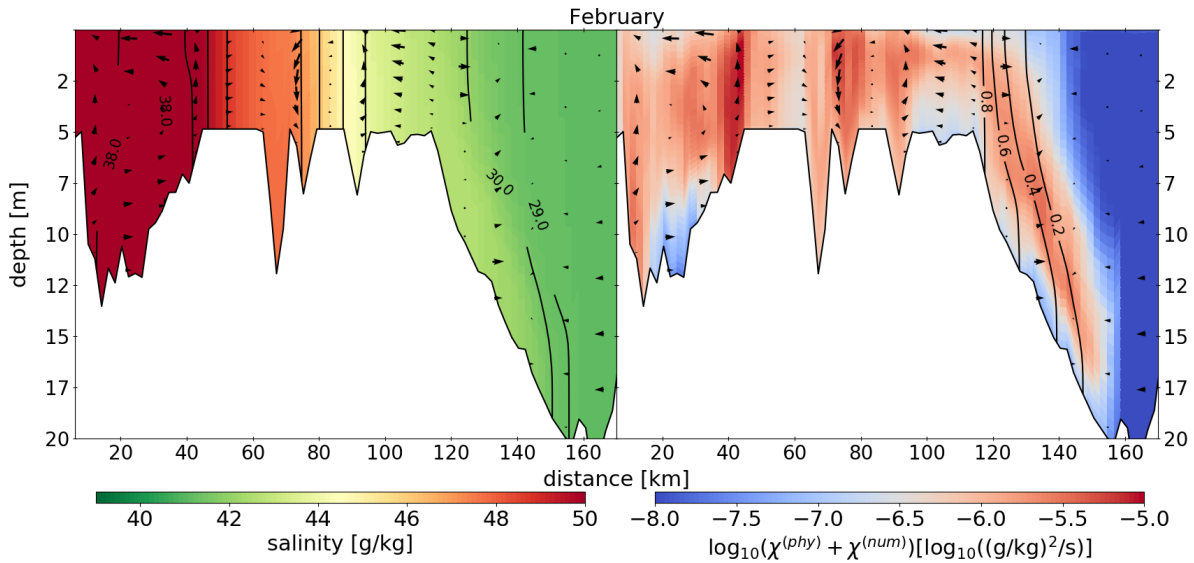
Figure 4.8.: Monthly mean salinity distribution (left) and the sum of physical and numerical mixing (right) along the first kilometers of the purple transect west of Qatar of February 2010. The contour on the left shows the density [kg/m^3] and on the right the concentration of tracer T_1.

The second highest densities can be found in winter in the northern and southern shallows. In figure 4.9 the bottom distributions of the tracers T_3 and T_4 are shown. At the end of January tracer T_3 and T_4 both have concentrations close to unity at the bottom indicating high vertical mixing during this month. Afterwards, both tracers start spreading into the deep channel which can be clearly seen at the end of all months except January. In addition, both tracers do not only spread in the channel, but also in the shallower parts due to advection by the circulation in the Gulf. With the very dense water in the north in winter and strong vertical mixing, both, the shallow and deep northern parts, definitely contribute to the outflow of PGW.

Moving on to the other two tracers in figure 4.10: The southern shallows, where tracer T_2 is released, have very high salinities and high densities during all seasons which are marginally greater than the densities in the north also found by Kämpf and Sadrinasab (2006) which is in contradiction to observational data, where the higher densities are found in the north (Swift and Bower, 2003; Yao and Johns, 2010a). This region is typically warmer than the north and more saline. This water feeds episodically into the deep channel where it mixes with the water from the north. The location where it enters the channel seems to be not the same for all times. At the end of January, the water enters in a wide range whereas at the end of April and August the water is entering at the eastern end of the shallows at the Strait of Hormuz. In December the
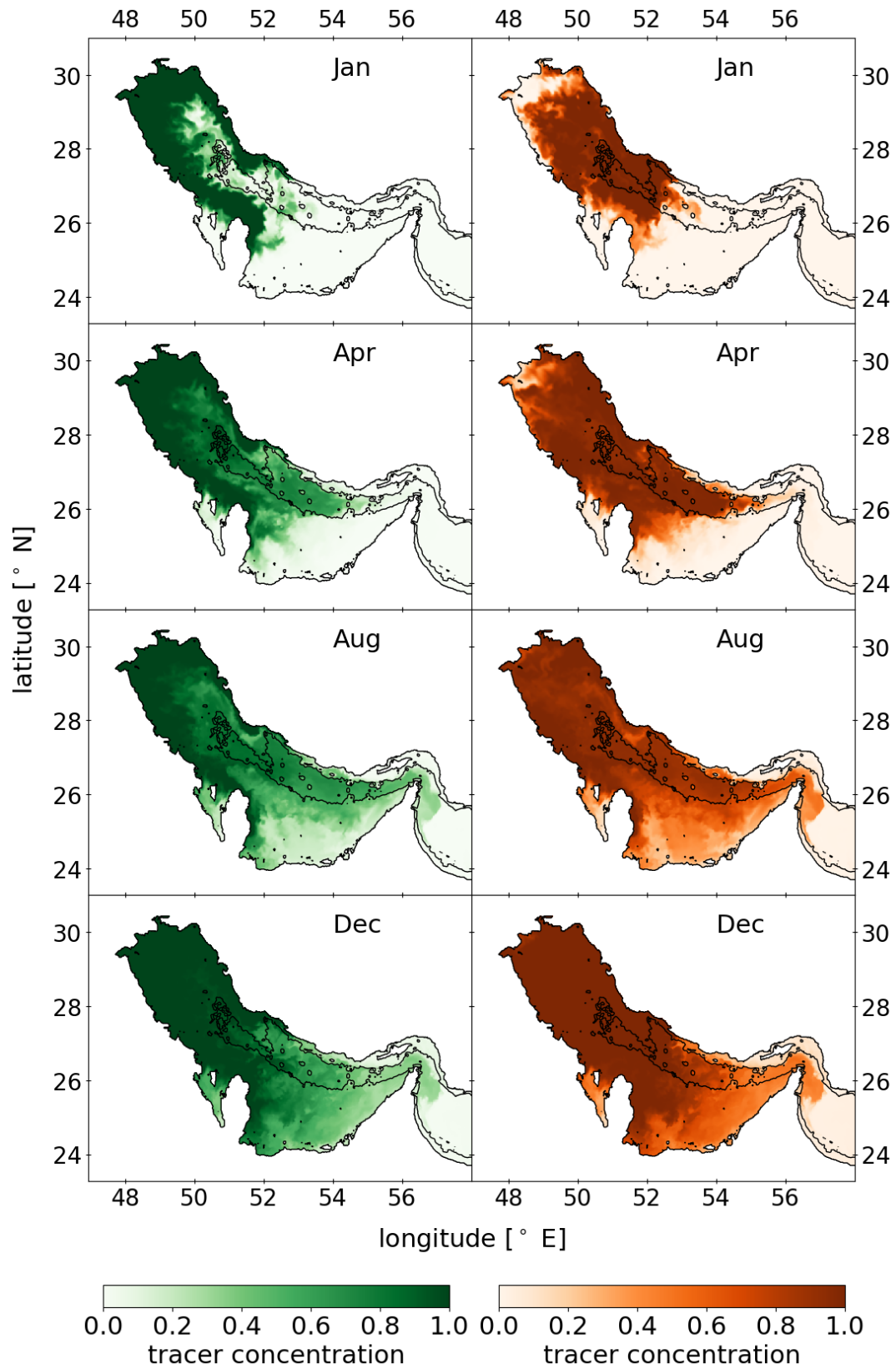
Figure 4.9.: Bottom spatial distribution of tracer T_3 (left) and T_4 (right) at the end of the labelled months.

water is entering in western parts again. It is found by Yao and Johns (2010a) that in winter this water feeds the bottom PGW and creates pulses of higher salinity leaving the Persian Gulf. But in summer the water of this region is too warm and stratifies below the IOSW but above the northern water and leaves the Persian Gulf as intermediate water. The stratification between the IOSW and the PGW will be shown later in section 4.3.2. The southern shallows contribute to the PGW and typically increase its salinity in an episodic way in winter.

Tracer T_5 is different than the others since it is released where the IOSW is dominant. At the end of January tracer T_5 is not vertically homogeneously mixed as the other tracers. At the end of April and August it spread into the north and south, but not into the deep channel. The vertical mixing is restricted due to a seasonal thermocline which develops in spring and vanishes in fall, further discussed in section 4.3. This indicates that the PGW is not formed in this region. In December the channel shows high concentrations which is partly due to tracer coming from the southern shallows which was already found to contribute to the dense outflow. But the main reason for the homogeneous water column is found in the vanished thermocline and increased vertical mixing due to surface cooling and evaporation. This region does not contribute to the PGW but is dominated by the IOSW.

To conclude, dense water from the north enters the channel and moves to the east following the channel. On its way water from the southern shallows enters the channel, if dense enough and the two waters are mixed. This mixed water leaves the Persian Gulf in the Strait of Hormuz and forms the PGW. The area around Bahrain where the highest densities are formed is only a minor contributor to the PGW since the outflow is restricted by Ekman transport and friction. Water leaving the area is mixed so quickly that no high concentrations outside the Bahrain area are found. These findings support the known circulation and features.

4.3. Overturning circulation

In the previous section it was analysed where dense water is formed. In the following, the further evolution of this water is presented. Therefore, first the horizontal circulation in different depths is presented and afterwards different transects are discussed which show how the dense water at the bottom is moving towards the Strait of Hormuz and out of the Persian Gulf.
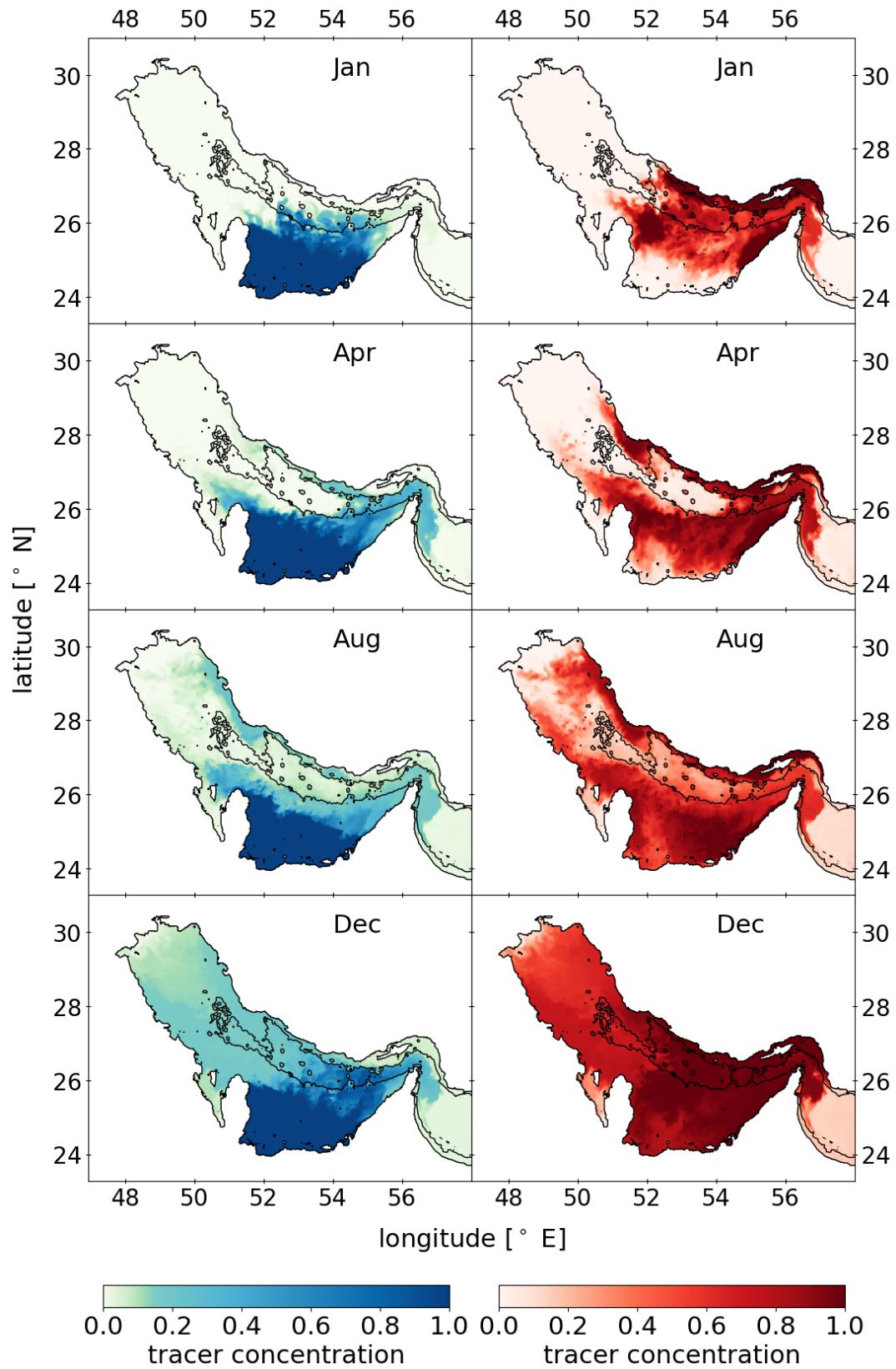
Figure 4.10.: Bottom spatial distribution of tracer T_2 (left) and T_5 (right) at the end of the labelled months.

The circulation of the Persian Gulf experiences a strong seasonal cycle. Especially the evolution of a thermocline, and thus stratification, has a strong influence on the circulation since it controls how far west the IOSW can spread. In summer, the fully developed thermocline restricts vertical mixing and the IOSW can reach far north into the Persian Gulf which can be seen in the salinity distribution in figure 4.11, and the cyclonic circulation establishes. With steadily increasing salinities the IOSW reaches up to kilometer 200 which is in the northern part, better seen in figure 4.15. In winter, when strong evaporation and heat loss create a lot of vertical mixing, the thermocline vanishes and the IOSW cannot reach far into the Persian Gulf, see figure 4.12. The circulation dissolves. Almost the whole Gulf is vertically mixed, stratification starts at around 700 km which is the eastern part of the Persian Gulf close to the Strait of Hormuz where water from the southern shallows stratifies below the IOSW. The IOSW does not propagate further than this area, also see 4.14. In this simulation run, the thermocline and with it stratification, starts to build up in March/April and starts to vanish in October. The evolution of the thermocline follows the evolution of the net heat flux Q_{net} since the heat flux is driving the SST. As soon as the net heat flux becomes smaller, the thermally well-mixed surface layer depth increases and the thermocline moves deeper. The heat loss in October increases the vertical mixing that much that the stratification and the thermocline is moved to a depth of 60 m. Further surface cooling and increasing evaporation lead to a completely vanished thermocline and stratification in November/December. Whereas the heat loss in October almost immediately increases the mixed layer depth, there is a time lag between the positive heat flux in February and March and the build up of the thermocline. Yao and Johns (2010a) found the thermocline to build up in May and vanish in November which is in agreement with this study.

4.3.1. Velocity fields in different layers

The surface circulation in the Persian Gulf is mainly driven by the inflow under the influence of Coriolis force and wind stress. The inflow is driven by a difference in surface elevation due to higher evaporation rate in the Persian Gulf compared to the Gulf of Oman, shown in figure 4.13. The surface elevation difference between the Persian Gulf and the Gulf of Oman is relatively stable over the year with a mean value of ~16 cm.
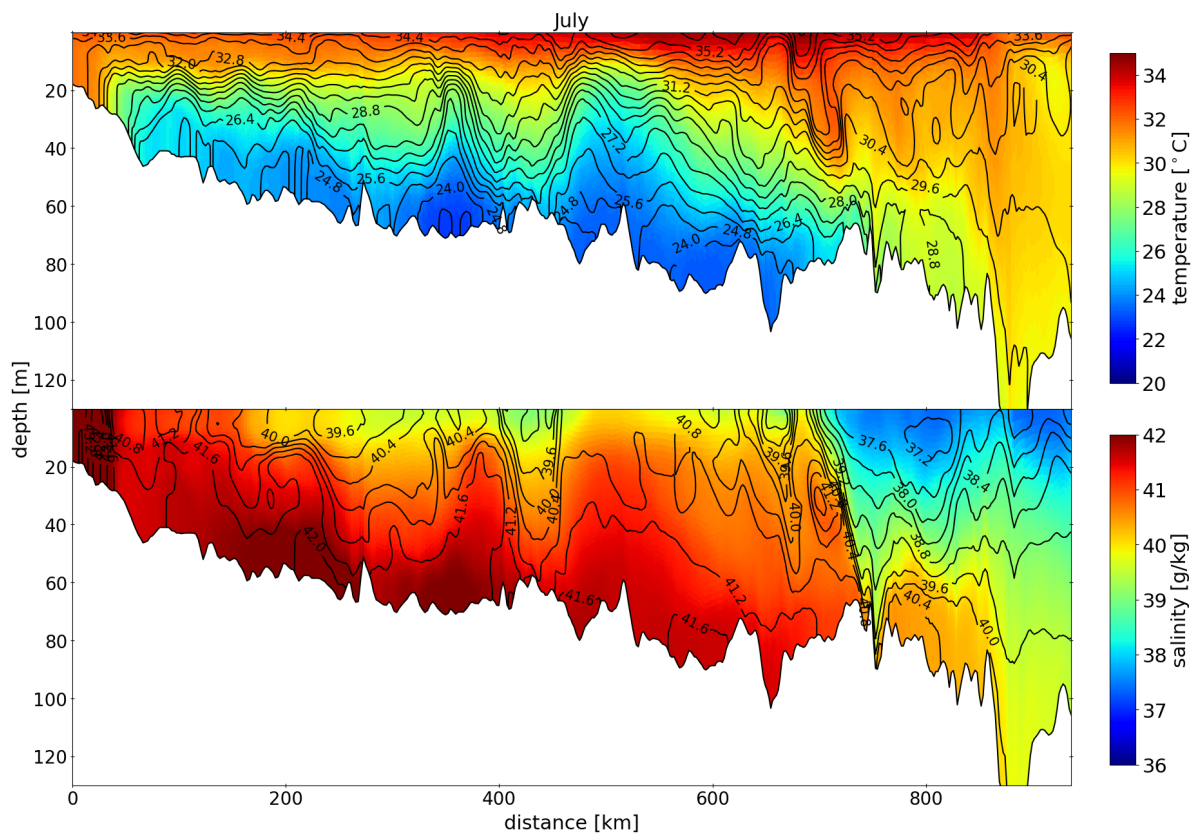
Figure 4.11.: Temperature and salinity distribution as a monthly mean of July along transect 1. The Strait of Hormuz is located around 825 km.

Figure 4.12.: Temperature and salinity distribution as a monthly mean of December along transect 1.
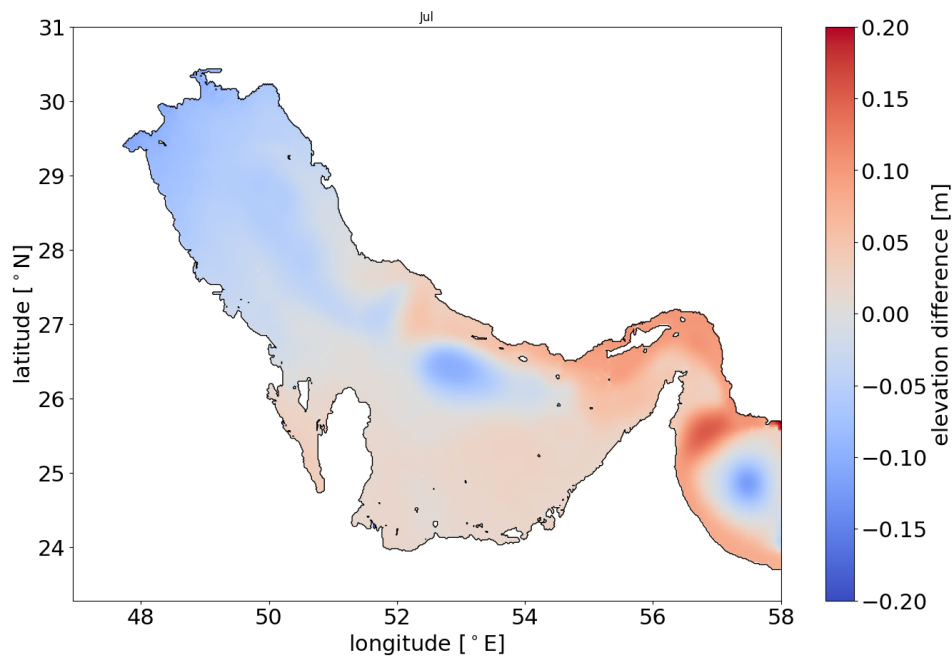
Figure 4.13.: Difference from the monthly mean surface elevation in [m] for July. The surface tilt causes the inflow of IOSW. The negative values in the Gulf of Oman and in the central Persian Gulf are caused by Ekman pumping due to large scale eddies, see figure 4.15.

In figure 4.14 and 4.15 the horizontal velocity fields in the upper 10 m (top), 20-40 m (middle) and 50-100 m (bottom) are shown as monthly means for the labelled months. In January the Persian Gulf shows no surface circulation with the exception that the IOSW is entering through the Strait of Hormuz and moving towards the southern shallows. The salinity field shows high salinities in the north and the southern shallows. These are the two regions which were already found to form the dense water. The IOSW does not reach far into the Gulf because of strong vertical mixing as discussed before.

The intermediate layer shows that saline water from the southern shallows is moving northeastward into the channel, indicating a salinity pulse which happen episodically in winter. In the bottom layer which shows the deep channel where the outflow is concentrated, a salinity gradient towards the Strait of Hormuz can be found. Higher velocities are located in the east where the gradient is stronger.

In spring the circulation starts to establish. Vertical mixing is weakened due to a positive heat flux and smaller evaporation which allows the IOSW to enter the Gulf further. As seen in April, the IOSW forms a jet at the Iranian coast, the Iranian Coastal Jet (ICJ)

which splits into two parts at around 52°E due to wind stress (Yao and Johns, 2010b). The first one, the northern branch, moves further north and forms a cyclonic eddy. The second one, the southern branch, forms a second eddy in the central Persian Gulf. The northwestward current north of Bahrain seems to be a consistent current in this simulation which is not found in other circulation studies. This current is only found in the surface layer which indicates the importance of wind stress for this phenomenon.

Going down to the intermediate layer, the two cyclonic eddies are dominant as well but with smaller velocities. The central eddy spreads in the whole central Gulf with small velocities in the south. The salinity field shows a salt tongue moving towards the deep channel and a low salinity at the Iranian coast from the IOSW at the northern part of the central eddy. The southern part of the eddy shows higher salinities which comes from the north. The bottom layer shows a high salinity in the east which is the dense water formed in the north during winter. The velocities are all eastward, indicating the outflow. Higher velocities are found in the Strait of Hormuz in the west and as well at around 52°E.

Towards summer, stronger stratification occurs due to higher SSTs since heating continues. In addition, since the transports are highest in summer, the IOSW reaches farther north. The salinity field in figure 4.15 shows that the IOSW reaches as far as 29°N. The cyclonic eddy in the north intensified and increased its size and dominates the circulation that the northwestern current north of Bahrain vanished. The central eddy increased its velocities and size as well. The intermediate layer shows the analogous circulation pattern with smaller velocities. The velocities from the southern shallows towards the channel are small, supporting the findings that the salinity pulses of this region happen mostly in winter. The bottom layer shows similar salinity and velocity pattern as before, with smaller salinities and no significant movement in the eastern channel.

In October, the surface salinity increased. The cyclonic eddies dissolved into smaller eddies and start to dissipate. A similar pattern is found in the intermediate layer. The bottom layer shows an almost constant salinity in the eastern and central channel with a weaker gradient towards the Strait and therefore smaller velocities indicating a smaller outflow.

With further vertical mixing the eddies become smaller and weaker in November and December but the IOSW can still be found at the Iranian coast, but with smaller
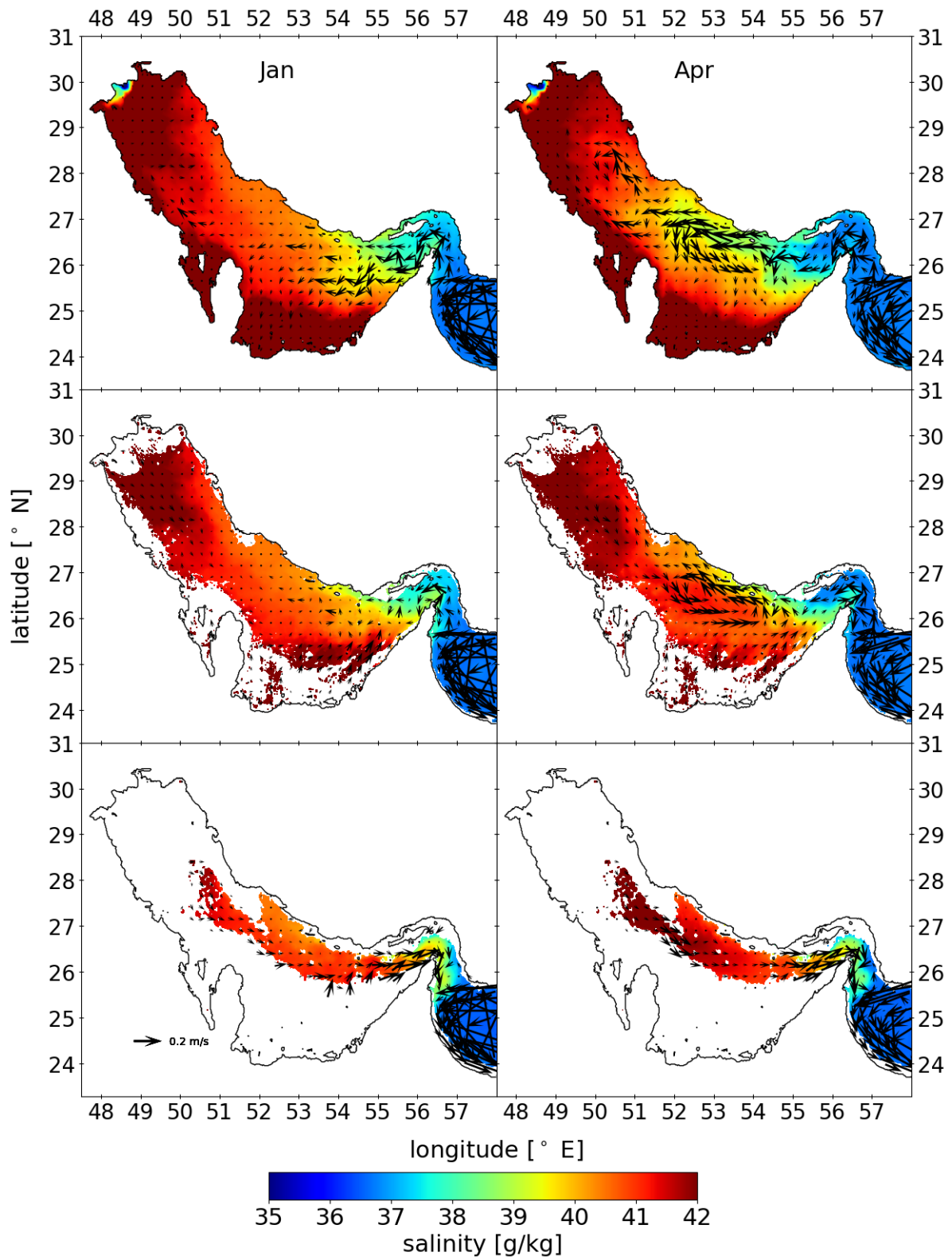
Figure 4.14.: Plot of the horizontal velocity field and salinity in the upper 10m (top), 20-40m (middle) and 50-100m (bottom) depth as monthly means for January (left) and April (right).

velocities. In addition, the velocities in the southern shallows towards the channel increase and the situation of January is found again.

All in all, the evolution of the circulation of the Persian Gulf of this study agrees well with the circulation found by Yao and Johns (2010b,a), for comparison see figure B.1, B.2 in the appendix. The occurrence of the northwestward current north of Bahrain does not occur in Yaos' and Johns' simulation. Since this current is only in the surface layer it is probably a phenomenon caused by wind. Other modelling studies like Thoppil and Hogan (2010) and Pous et al. (2015) agree with the circulation as well.

4.3.2. Cross sections

So far, the regions of formation of dense water and the seasonal general circulation were discussed. In the following, the vertical structures along different transects are discussed with focus on the outflow in the channel. Furthermore, the stratification of water from the southern shallows into the channel is shown and further validation is done.

Transect 1

The temperature and salinity distributions along transect 1 are shown in figure 4.11 and 4.12 but have not been fully discussed yet. Only the evolution of the thermocline was discussed since it is important to understand the seasonal circulation. In the following, the salinity distribution, indicating the exchange flow is discussed and validated with measurements.

Going back to figure 4.11 which shows the vertical temperature and salinity distribution along the axis of the Persian Gulf in transect 1: The temperature shows a strong thermal stratification with cold water of around $\sim$24-25°C at the bottom which was produced in winter in the north and warm water of >35°C at the surface. The salinity distribution follows the isotherms as seen at kilometer 400 with bottom salinities of $\sim$42 g/kg and surface salinities <40 g/kg which are smaller at the Strait of Hormuz due to the IOSW. Around 700 km which is located around 55°E and 26°N a sharp and steep salinity front has established where the PGW and the IOSW clash. This sharp front is found in spring
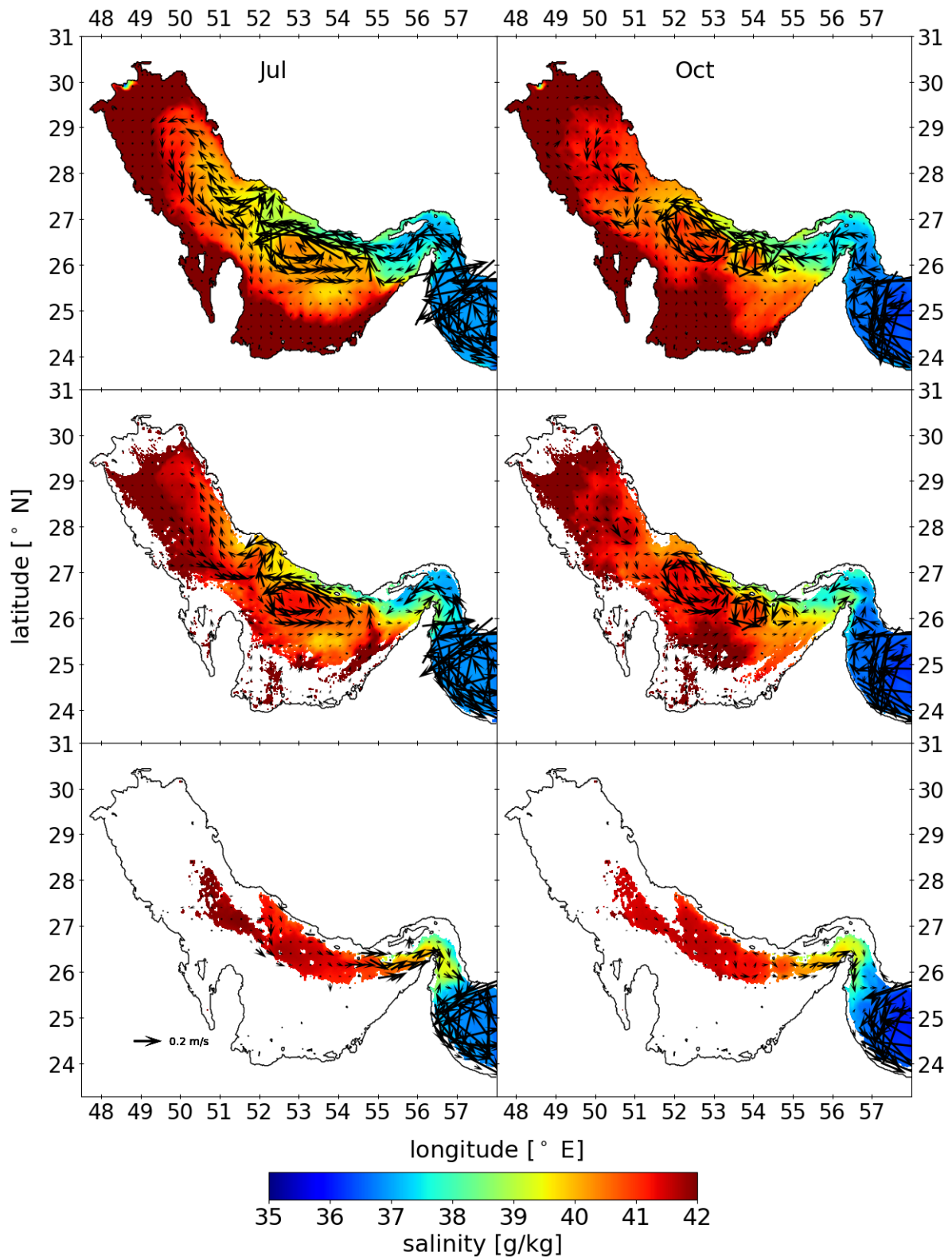
Figure 4.15.: Plot of the horizontal velocity field and salinity in the upper 10m (top), 20-40m (middle) and 50-100m (bottom) depth as monthly means for July (left) and October (right).

and summer. In fall and winter this front is not as steep but fronts can also be found in the Strait, see figure 4.12. According to figures 4.14 and 4.15, the IOSW meets the eastern end of the cylonic eddy in this region in the central Gulf (or the farthest east eddy in fall). The mixing in this region is high and the water is advected northward to the Iranian coast. The depth of these eddies can be up to 60 m, see subsection of Transect 3, which is almost the water depth of this region. East of this front, the bottom salinities have decreased compared to the salinities west of this point. This strong horizontal salinity gradient seems to be the reason for the increased bottom velocities in this region. Winter salinities decrease from the north towards the Strait and are vertically homogeneous. West of the Strait where the IOSW is present, less saline water is stratified over saline water with salinities <42 g/kg but greater than the salinities in the west. This saline water is originated in the southern shallow as the tracer T_2 distribution confirms, not shown. This confirms that the highest salinities of the outflow in winter come from the southern shallows (Thoppil and Hogan, 2009).

A similar transect has been investigated by Reynolds (1993) during the Mt. Mitchell expedition in the early 90s, see figure B.4 for early summer (May-June). Comparing the results with the month May of this simulation, not shown, it follows that this study is about 3°C warmer in the whole water column and about 1 g/kg more saline. The density, on the other hand, shows a similar density range from >29.5 kg/m^3 for the densest water patches to <24 kg/m^3 for the IOSW in the Strait of Hormuz. It should be noted that the winter before the expedition was the coldest winter recorded in that area at that time which produced really cold waters <15 °C in the north, compare figure B.3 in the appendix. The winter measurements show an almost vertical homogeneously situation, where the isolines slowly start to tilt. In comparison to this study, again the salinities and temperatures show the same differences as in May but the density distribution fits well. Comparison of this study to the axial transects given by Swift and Bower (2003), who took all available data and combined them into one dataset including the data collected during the Mt. Mitchell expedition, show similar results: The temperature and salinity are too high, but the density does fit.

Concerning the salinity front, observations do not show such a salinity front west of the Strait, but the simulations by Yao and Johns (2010a) (figure 5a-d) show similar fronts in depths up to 40 m where the IOSW and more saline water from the Persian Gulf clash. The transects by Swift and Bower (2003) show a sharp salinity front south of the Strait where the Persian Gulf meets the Gulf of Oman, but not in the Persian Gulf itself. This region is not covered by transect 1 of this study.

Transect 2

Transect 2 is located at the eastern Persian Gulf at the transition to the Strait of Hormuz close to the measurements of Johns et al. (2003), for plot see figure B.5 in the appendix. The measurements show a stable stratification with an outflow banked against the southern coast. The interesting finding was that there is a surface outflow which is found to be part of a surface recirculation. Similar observational results were found for this transect by Pous et al. (2004).

In figure 4.16 and 4.17 the respective monthly means of this simulation are shown. In March one finds a temperature of 26.0°C at the surface and 24.4°C at the bottom. This differs by nearly 4°C to the measurements where temperatures between 22.5°C and 21.0°C were found. This deviation can be partly explained by the too high heat flux of this study which increases the temperature, $\sim$2°C, see section 4.1.1 and 4.2.1. But this does not explain the whole temperature difference. The measurements were obtained 12-13 years before this simulation run and therefore climatological conditions during the simulation period could just have been different than during the measurements. This includes different weather conditions, different IOSW temperatures and salinities, different strengths and time scales in the exchange flow. An interesting feature in the isotherms is their downward banking at the western coast which is reverse to the upward banking in the isohalines. This feature can be seen with smaller angles in July measurements as well. This is even more surprising since there are positive vertical velocities at this end. The upward dent in the isotherms can be explained by higher vertical velocities at kilometer 10 to 15 than at the kilometer 5 to 10. An explanation for this tilt is not given by Johns et al. (2003). For the north there is a tilt as well and it shows the border between IOSW and PGW since there are slightly higher salinities. The salinity distribution shows a banking to the south due to the geostrophic outflow with velocities of 0.2 m/s and salinities up to 40.5 g/kg which is compared to measurements slower and more saline.

In July, figure 4.17, the SST is $\sim$35.0°C and the bottom temperature $\sim$28.8°C which is again warmer compared to the measurements. But the interesting part can be seen in the velocity contour. The outflow is again banked to the south but in this month there is a surface outflow. This outflowing water at the surface is of different origin than the bottom water. Johns et al. (2003) measured a second outflow in July between 20 and 40 m depth and found the reason for this in surface recirculation. This finding can be confirmed by this study since the surface outflow shows only very low concentrations of
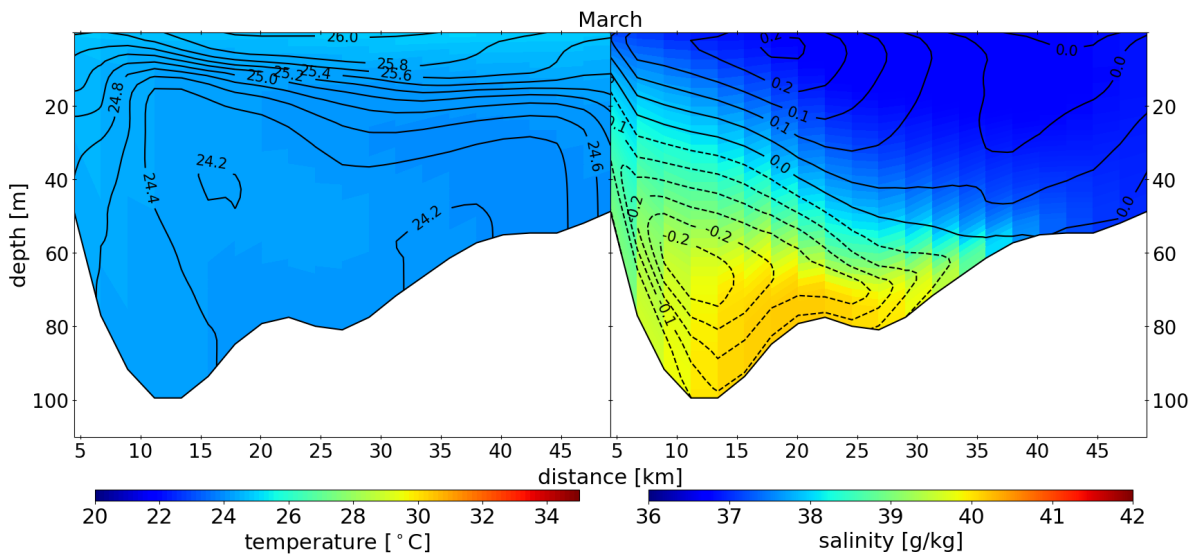
Figure 4.16.: Temperature (left) and salinity distribution (right) along transect 2. The contour on the left shows the temperature [°C] and on the right the perpendicular velocity [m/s] where negative values indicate velocities towards the Strait of Hormuz.

tracer T_3, T_4 but higher concentrations of tracer T_2 and T_5, not shown. Yao and Johns (2010a) found parts of the recirculation are formed by warm water from the southern shallows which cannot sink to the bottom and is therefore stratified into the water column. This can be confirmed by this study but not in all cases high concentrations of tracer T_2 are found.
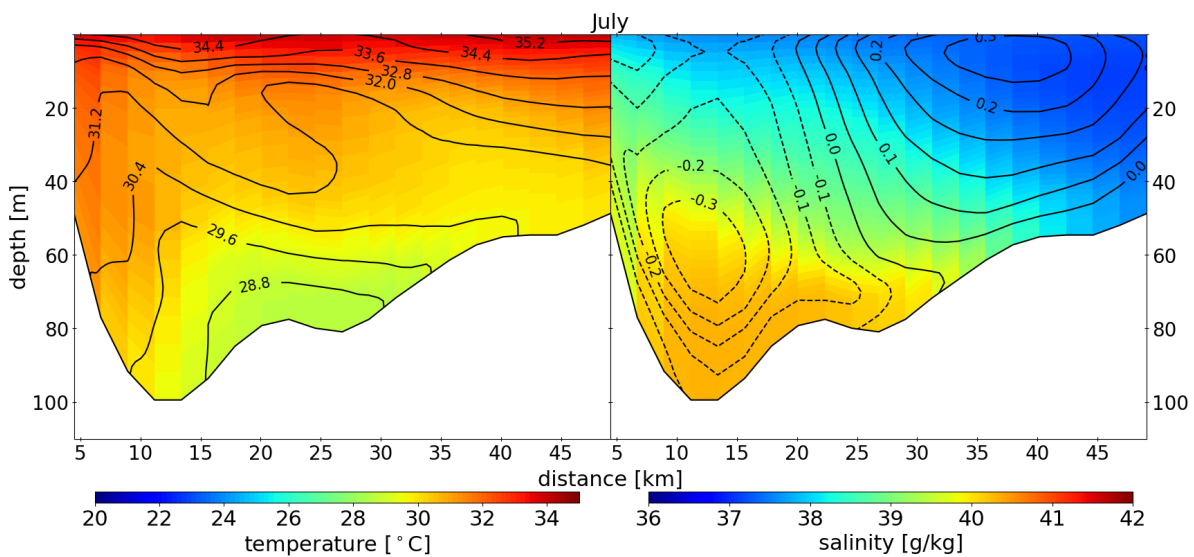
Figure 4.17.: Same as figure 4.16 but for July.

Transect 3

This transect shows a cross section from the southern shallows towards the north and across the channel. This transect will be used to shortly visualise the intrusion by the southern shallows. In figure 4.18 the salinity and tracer T_2 distribution show that dense water is created in the southern shallows on the left and spill into the bottom of the channel which is better seen in the tracer distribution. The salinity decreases from >42 g/kg to <41 g/kg on this way. At the surface and the north (right) the IOSW with low salinities can be seen. The IOSW reaches at the northern end into depths to 40 m. The velocity contours show a weak cyclone which almost reaches to bottom of the channel.
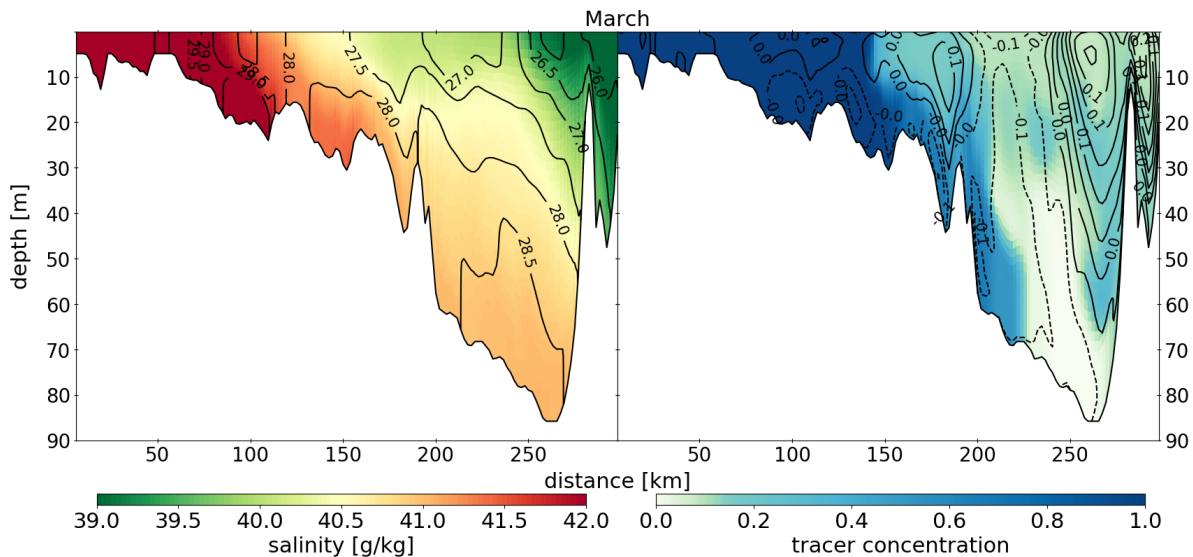

Figure 4.18.: Salinity (left) and tracer T_2 (right) distribution along transect 3 for March. The contour on the left shows the density [kg/m³] and on the right the velocity [m/s] which is perpendicular to the transect. Negative velocities point towards the Strait of Hormuz to the east.

In July, in figure 4.19 when temperatures are higher the density of the southern shallows is smaller than the density in the channel and therefore the water is stratified into the water column. Note that the water is moved to the east since it is influenced by the cyclone in the central Persian Gulf. This water becomes part of the recirculation as described before in the Transect 2 subsection and found by Yao and Johns (2010a). In the surface layer, again, the IOSW can be found with low salinities in the north but also more south. The water column is vertically stratified with water from the north is stratified below the IOSW. The cyclone has strengthened and reaches depths up to 40 m. Below, the slow but steady outflow of dense water from the north is located.
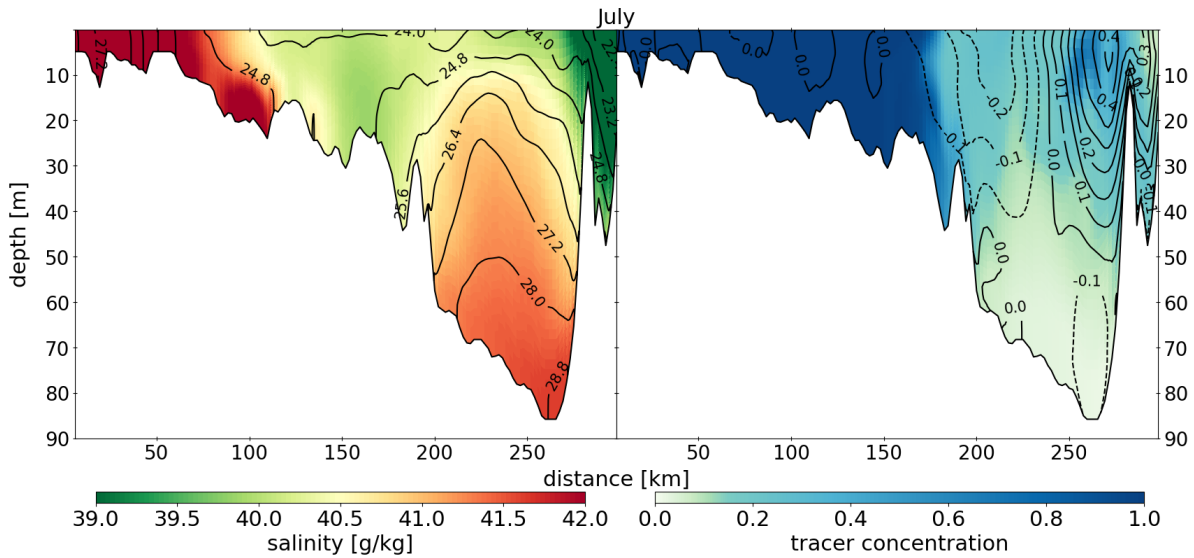
Figure 4.19.: Same as figure 4.18 but for July.

4.3.3. Complete overturning circulation

Putting all pieces from the previous subsections together, the overturning circulation of the Persian Gulf can be described as the following: The inflowing IOSW is entering through the Strait of Hormuz into the Persian Gulf and moves along the Iranian coast to the north, as the Iranian Coastal Jet (ICJ) while increasing its salinity. At 52°E the ICJ splits into two parts: One going north and one going south. Both branches form a cyclonic circulation in one or more eddies and transport IOSW to the shallow regions in the north and south where the saline and dense Persian Gulf Water (PGW) is formed. This dense water sinks into the deep channel along the Gulf axis and forms the dense outflow in the Strait of Hormuz. The saline waters produced in the southern shallows contribute to the outflow in two ways: In winter it increases the salinity of the outflow in episodic events. In summer, when the water is lighter than the water in the channel, it stratifies on top and becomes part of a surface recirculation. This recirculation creates a salinity front when the saline water clashes with the IOSW. In addition, the Persian Gulf experiences a seasonal cycle in its overturning circulation: In summer the IOSW reaches farther into the Persian Gulf because of the stratification and forms the above described circulation pattern. In fall and winter vertical mixing due to heat loss and evaporation prevents the IOSW from reaching far north, resulting in a vanishing surface circulation.

4.4. Quantification of transports through the Strait of Hormuz into the Gulf of Oman

4.4.1. Cross section

The transect discussed in the following is transect 5 which is located at the transition of the Strait of Hormuz to the Gulf of Oman. The temperature and salinity distribution of this transect is shown in figure 4.20 for the month April. The distributions show a two layer exchange flow with cold, saline water leaving the Persian Gulf at the bottom, banked against the western coast and warmer, fresher water entering the same. This spatial pattern is similar to the pattern already found at transect 2 with the exception of the surface outflow due to recirculation. Interestingly, the highest velocities of the inflow are on the west of the transect and not the east as one would expect due to Coriolis force. This coastal jet is a persistent feature which is found in all months with small changes in shape. For example in October, figure 4.21, the coastal jet is located close to the coast, whereas in April the surface jet spreads farther to the east. In summer the surface current is located far east resulting in a very weak current at the western coast with velocities <10 cm/s. Another interesting fact is that positive velocities can be found down to 100 m at the western coast. The salinity distribution along the transects shows a seasonal feature as well: In spring to early summer, the PGW occupies a smaller cross section than in late summer, fall and winter. This creates a near surface inflow of water which is more saline than the IOSW at the western coast during that time span of the year. This leaves the following questions: What causes this current? And, why does the occupied area of the PGW in the cross section change in time?

The Strait of Hormuz has been intensively measured by Pous et al. (2004) in October/November 1999. The results show a similar banking but salinities are about 1 g/kg smaller and temperatures about 3°C colder compared to figure 4.21. These differences match the differences already found in transect 2. Unfortunately no velocity profiles have been measured along the transects. Therefore, measurements cannot give answers to the questions concerning the western current. Yao and Johns (2010b) do not discuss this current, but the surface velocity fields of their work show that this current is persistent in the 'buoyancy only' simulation and is almost not influenced by the high frequency and climatological run. Therefore, this current must be buoyancy driven.
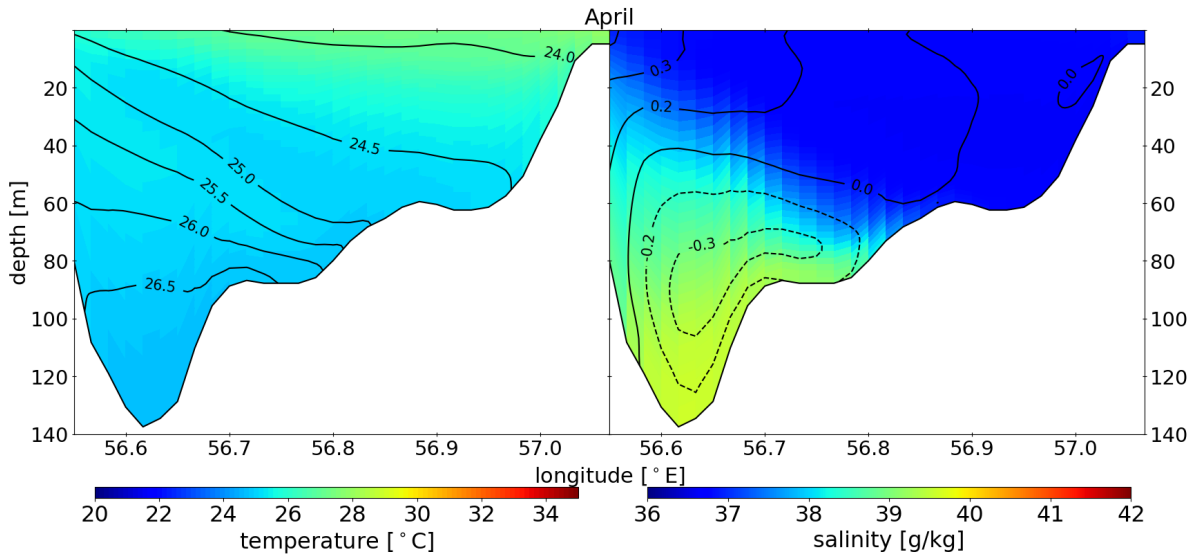
Figure 4.20.: Temperature (left) and salinity (right) distribution along transect 5 which marks the border between the Persian Gulf and the Gulf of Oman for April. The contour on the left shows the density [kg/m^3] and the perpendicular velocity [m/s] on the right. Negative velocities indicate a southward direction.
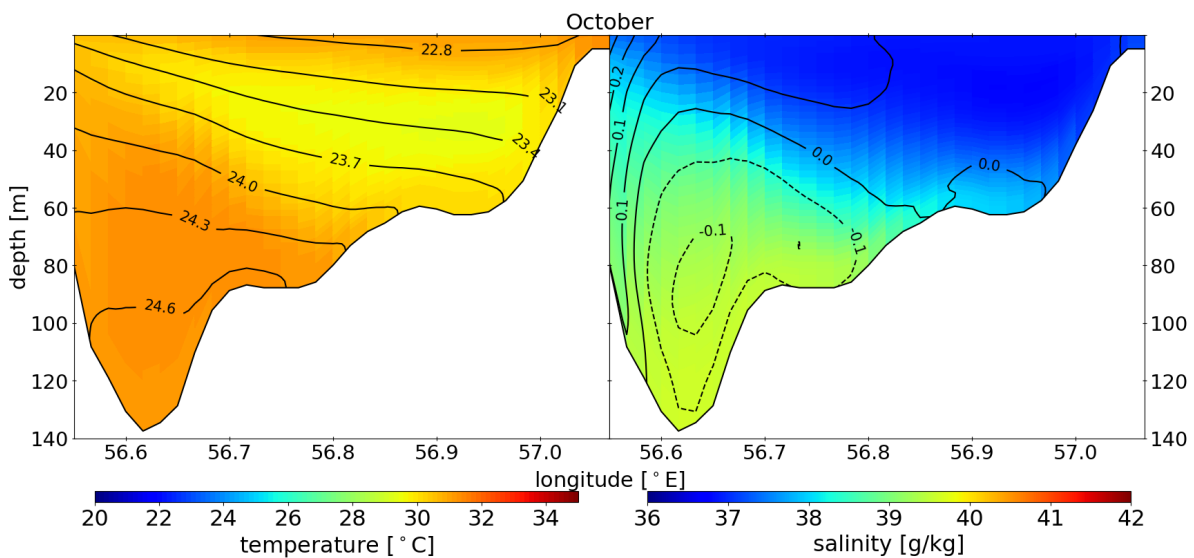

Figure 4.21.: Same as figure 4.20 but for October.

For the high salinities, it was already shown that in fall and winter the vertical mixing increases. This should also mix up the PGW and this could create the increased cross section of PGW along the transect. In figure 4.22 the mixing along the transect is displayed for October where the PGW spreads into the surface layer above 20 m depth. At the western coast, where the current is located, very high mixing is found which mixes the salinity into the current in the whole water column and at the surface. Similar mixing patterns and values are found for every month suggesting that in this transect not only the heat loss and evaporation are responsible for the mixing. A mixing independent explanation can be the stratification of water from the southern shallows. In summer it stratifies over the denser water from the north and increases the PGW cross section. In winter the cross section becomes smaller when the main contribution of the outflow comes from the southern shallows. Probably both mechanisms are active at the same time. Mixing definitely plays an important role as well as the stratification. The data by Johns et al. (2003) show a similar seasonal increase and decrease in the occupied cross section but is not further discussed.
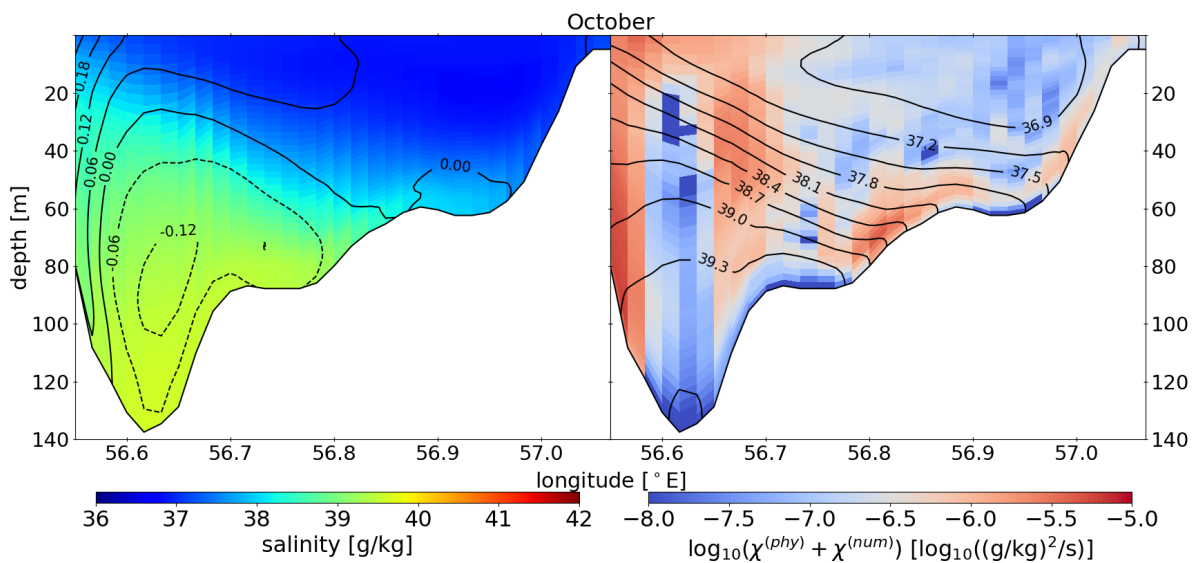

Figure 4.22.: Salinity (left) and mixing (right) distribution along transect 5 for October. The contour on the left shows the perpendicular velocity [m/s] and the salinity [g/kg] on the right.

4.4.2. Transports, salinities and residence time

The quantities describing an exchange flow are the transports and salinities. Therefore, the TEF theory was used to calculate those: Figure 4.23 shows the monthly mean TEF-

profiles for the exchange flow for 2010. Taking a look at the shape of the TEF-profiles, one can identify the inflow in low salinity classes and the outflow in higher salinity classes. In figure 4.24 the daily transports and salinities of the in- and outflow are shown. The graphs have been smoothed using a 7 day running mean. The annual mean values for the exchange flow are given by:

$$Q_{in,year} = 0.20 \pm 0.02 \,\text{Sv} \tag{4.6}$$

$$Q_{out,year} = -0.19 \pm 0.02 \,\text{Sv} \tag{4.7}$$

$$s_{in,year} = 37.02 \,\text{g/kg} \tag{4.8}$$

$$s_{out,year} = 38.86 \,\text{g/kg} \tag{4.9}$$

Comparison of the computed annual means with other studies, see table 4.2, shows this study agrees well with measurements of Johns et al. (2003) and model results of Pous et al. (2015). Pous et al. (2015) show that the transports can vary significantly from one year to another. Therefore, comparison to transports of different years should always be done with this in mind. Nevertheless, the transports are in the right order of magnitude.

As the overturning circulation has a seasonal cycle, one can find a seasonal cycle in the TEF profiles and the transports as well, see figure 4.23 and 4.24: In January the inflow shows a strong influence of winter storms, seen in the high standard deviation in the TEF profiles and the fluctuating daily transports. Highest salinities of this simulation are in January as well. This saline water is coming from the southern shallows and was created in fall. s_{out} shows strong changes in winter and spring. The values are varying by $\sim$1 g/kg in a time span of a few days and stay on a constant high value

	Johns et al. (2003)	Pous et al. (2004)	Pous et al. (2015)	Yao and Johns (2010a)
Q_{in}	0.23 ± 0.04 Sv	0.21 Sv	0.203 Sv	
Q_{out}	-0.21 $\pm$ 0.05 Sv	-0.17 Sv	-0.194 Sv	-0.15 Sv (Jul); -0.07 Sv (Jan)
s_{in}	37.0 ± 0.3 psu			
s_{out}	38.9 ± 0.4 psu			

Table 4.2.: Comparison values for the transport of the exchange flow. The values of Q_{out} of Johns et al. (2003) and Pous et al. (2004) are the sum of the recirculation and bottom outflow values, the errors displayed are summed up as well. The values for Pous et al. (2015) are the means for the years 1995-2000 (table 1).
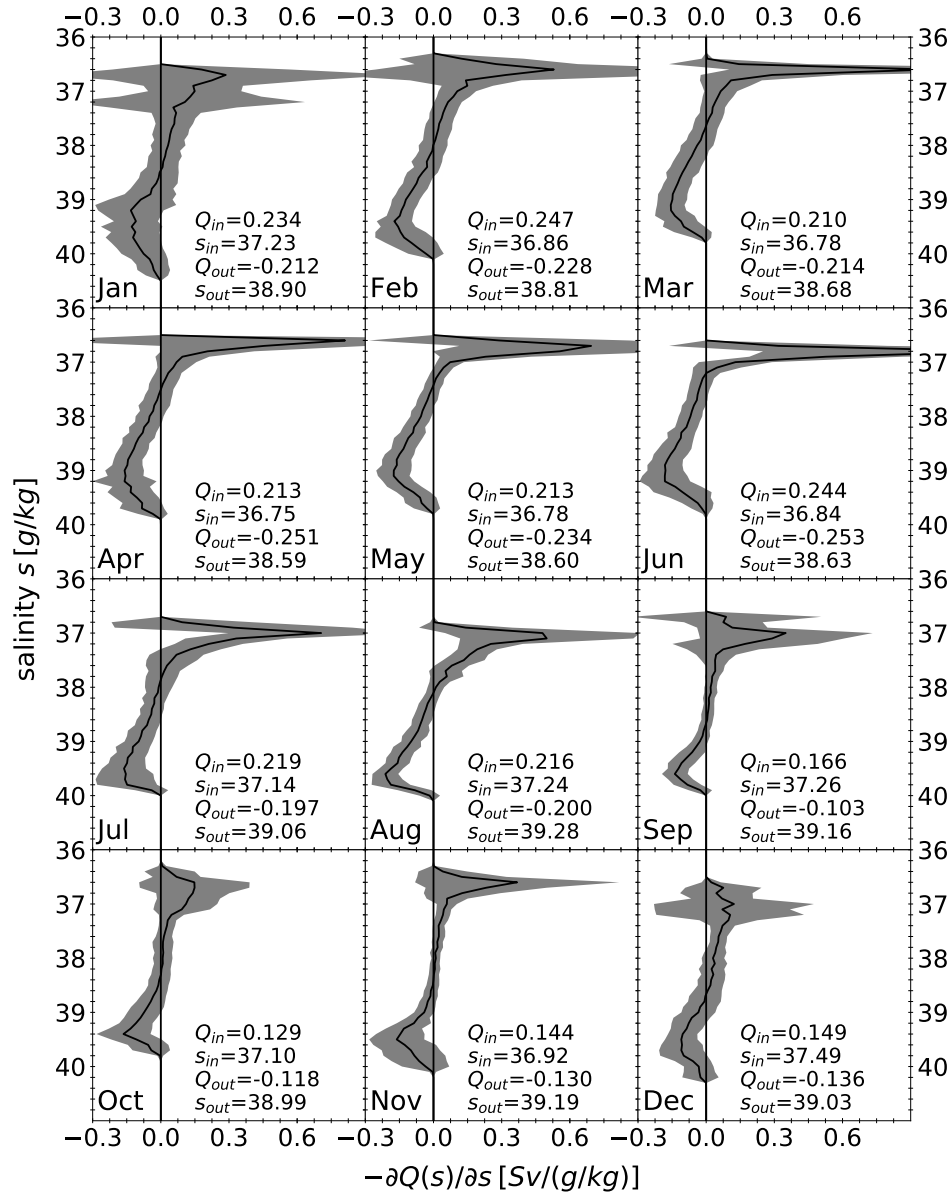
Figure 4.23.: Monthly means of the derivative of the isohaline transport function $-\frac{\partial Q(s)}{\partial s}$ defined in section 2.2.3 are shown as the black lines. In grey the standard deviation of the mean is shown. In addition, the transports and salinities of the in- and outflow are computed.

for 2-3 weeks before becoming smaller again. This matches the description of salinity pulses by Yao and Johns (2010a); Thoppil and Hogan (2009). In this simulation these pulses from the southern shallows can be found until early summer. s_{in} during this time is decreasing in January and stays on a constant small value until July. During this time span of constant small salinities the TEF-profiles show a distinct peak in salinity classes of $\sim$36.5 g/kg. The transports are greater than the annual mean and have their

respective maximum in June. From July both salinities increase. The dense water from the north created in winter reaches the transect and increases the s_{out} to a constant value above the annual mean. s_{in} increases as well due to the western coastal jet which transports saline water back into the Strait since the cross section of the PGW increases. The TEF-profiles show a widening of the inflows' salinity classes which support this thesis. In fall the transports become smaller and the inflow is further widened in salinity classes. Minimum transports are found in late October. In November an increase in s_{out} can be seen which looks similar to a salinity pulse. But the water from the southern shallows should not be dense enough to become part of the PGW during this time. It is possible that an early pulse happened or late winter water reached the Strait.
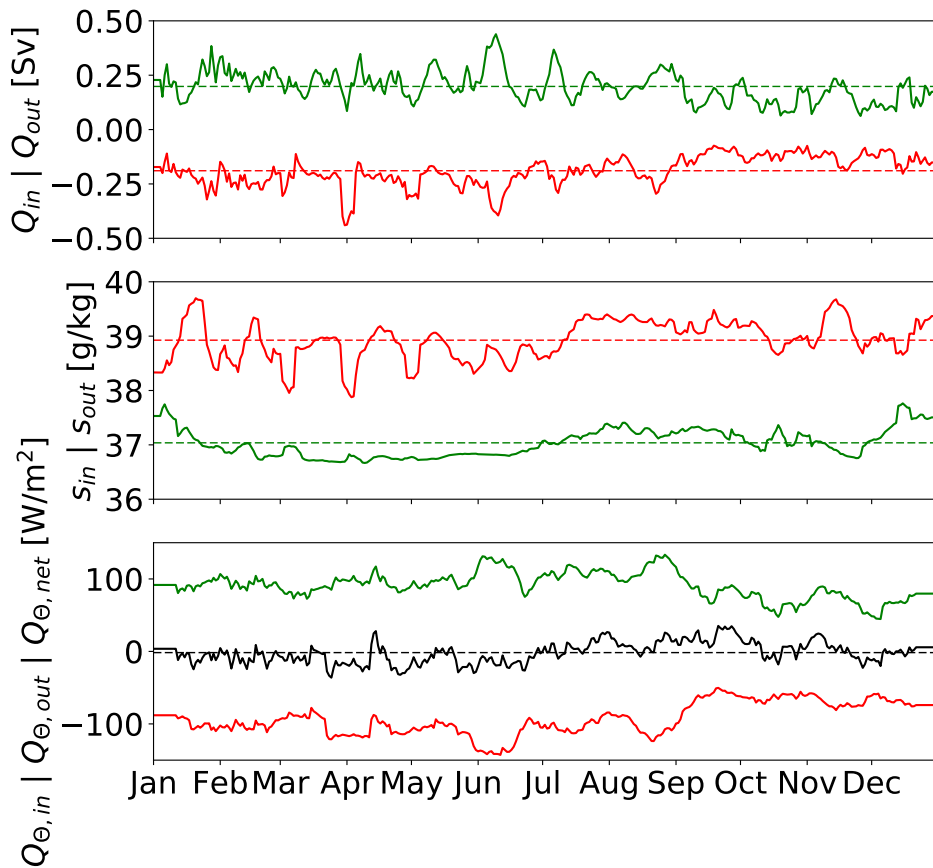

Figure 4.24.: Daily exchange flow quantities for the inflow (green) and the outflow (red), dashed lines show the annual mean values. Top: transports (running mean of 7 days), middle: salinities (running mean of 7 days), bottom: heat fluxes (running mean of 21 days, the black graph shows the sum of $Q_{\theta,net} = Q_{\theta,in} + Q_{\theta,in}$).

With the knowledge of the outflow, one can estimate the residence time by which the whole water is replaced by dividing the volume of the sea by the outflow:

$$t_{res} = \frac{V_{PG}}{Q_{out,year}} = 1.33 \, \text{yr.} \tag{4.10}$$

Results by Sadrinasab and Kämpf (2004) show longer flushing times of 1-8 years, depending on how far the area is located away from the Strait of Hormuz. These results were computed using a tracer released in the Gulf of Oman. When the concentration in a grid cell is over 95 % the time is set to be the flushing time. These results are more exact since the used method is better. Mean flushing times of bottom water are estimated to be ∼6 years.

4.4.3. Heat

Using TEF theory again, one can estimate the heat exchange through a chosen cross section. In this case transect 5. Instead of computing the salinity flux, one can compute a temperature flux when substituting s with the temperature θ in equation (2.56). The resulting temperature flux F_θ can be, similarly to the transports, split up into an in- and outgoing part, $F_{\theta,in}$ and $F_{\theta,out}$. These can be converted to an equivalent heat fluxes:

$$Q_{\theta,in} = \frac{C_p \rho_0}{A_{PG}} F_{\theta,in}, \tag{4.11}$$

$$Q_{\theta,out} = \frac{C_p \rho_0}{A_{PG}} F_{\theta,out}, \tag{4.12}$$

where A_{PG} is the surface area of the Persian Gulf. In figure 4.24 those heat fluxes and the sum $Q_{\theta,net}$ are shown at the bottom. One can see that in the first half of the year the Gulf loses heat to the Gulf of Oman since it exports warm water, formed in summer/fall, and imports colder IOSW. In the second half of the year it is the other way round: The Gulf imports warm water and exports colder water which was formed in winter/spring. This corresponds to a time lag of approximately half a year. The annual mean of $Q_{\theta,net}$ is ∼-1.1 W/m² which is close to zero, indicating that the exchange flow does not add heat to the Persian Gulf in an annual cycle.

Chapter 5.

Outlook

What should be done next? First and most important, the shortwave radiation and with it the net heat flux should be corrected by reducing the mean shortwave radiation by ~37 W/m^2. This should improve the temperatures and therefore should show better agreement with observations. Second, the tidal amplitudes, especially the M2 and K1, should be corrected to have correct tide induced mixing in the model. This could be done by using the regional OTPS for the Persian Gulf region in future simulations. This should provide more accurate tides. Third, the river input data should be more frequent than monthly means and should include all rivers, if data is accessible. Although the river input is only small compared to the evaporation, this should be done especially for the Arvand river which is the largest river mouthing into the Persian Gulf and influences the circulation in the north. Fourth, a more detailed investigation of the PGW, for example the composition of water from the north and south, could be done by using TEF theory along more transects. Additionally, an estimate for the total mixing could be done using the work of Burchard et al. (2017 in prep.) which first has to be modified to include inverse estuaries. Fifth, using adaptive coordinates instead of general vertical coordinates should probably improve results as well since the seasonal thermocline would be better resolved and numerical mixing would be reduced. In addition more layers could be used to improve the vertical resolution. Last but not least, the simulation period can be increased to study changes on longer time scales.

Appendix A.

Scale analysis of the RANS

For scale analysis one divides each state variable into a non-dimensional scale and a part with dimension which has the order of $\mathcal{O}(1)$ to evaluate which are the leading terms and which terms can be neglected since their contribution to the problem is small. For example the velocity u:

$$\tilde{u} = \frac{u}{U} \tag{A.1}$$

where U is the typical velocity scale and $\tilde{u}$ is the dimensionless part of $\mathcal{O}(1)$. We assume the following typical scales for the state variables:

$$x, y : L = 10^5 \, \mathrm{m}$$
$$z : H = 100 \, \mathrm{m}$$
$$u, v : U = 0.1 \, \mathrm{m \, s^{-1}}$$
$$w : W = \frac{H}{L} U = 10^{-4} \, \mathrm{m \, s^{-1}}$$
$$f : \Omega = 10^{-5} \, \mathrm{s^{-1}}$$
$$\rho_0 : R_0 = 1000 \, \mathrm{kg \, m^{-3}}$$
$$\hat{\rho} : R = 1 \, \mathrm{kg \, m^{-3}}$$
$$\hat{p} : P = 100 \, \mathrm{Pa}$$
$$u', v', w' : U^* = 10^{-2} \, \mathrm{m \, s^{-1}}$$
$$\nu : N = 10^{-6} \, \mathrm{m^2 s^{-1}}$$
$$g : G = 10 \, \mathrm{m \, s^{-2}}$$
$$t : T = L/U = 1000 \, \mathrm{s}$$

The x-components of the RANS (2.11) reads as:

$$
\frac{\partial \langle u \rangle}{\partial t} + \langle u \rangle \frac{\partial \langle u \rangle}{\partial x} + \langle v \rangle \frac{\partial \langle u \rangle}{\partial y} + \langle w \rangle \frac{\partial \langle u \rangle}{\partial z} - f \langle v \rangle = -\frac{1}{\rho_0} \frac{\partial \langle \hat{p} \rangle}{\partial x} + \frac{\partial}{\partial x} \left(\nu \frac{\partial \langle u \rangle}{\partial x} \right.
$$
$$
\left. - \langle u'u' \rangle \right) + \frac{\partial}{\partial y} \left(\nu \frac{\partial \langle u \rangle}{\partial y} - \langle u'v' \rangle \right) + \frac{\partial}{\partial z} \left(\nu \frac{\partial \langle u \rangle}{\partial z} - \langle u'w' \rangle \right).
\tag{A.2}
$$

Using (A.1) for all state variables and divide the equation by ΩU, we find the dimensionless equation:

$$
\underbrace{\frac{U}{\Omega L}}_{0.1} \left[\frac{\partial \langle \tilde{u} \rangle}{\partial \tilde{t}} + \langle \tilde{u} \rangle \frac{\partial \langle \tilde{u} \rangle}{\partial \tilde{x}} + \langle \tilde{v} \rangle \frac{\partial \langle \tilde{u} \rangle}{\partial \tilde{y}} \right] + \underbrace{\frac{W}{\Omega H}}_{0.1} \langle \tilde{w} \rangle \frac{\partial \langle \tilde{u} \rangle}{\partial \tilde{z}} - \tilde{\Omega} \langle \tilde{v} \rangle = - \underbrace{\frac{P}{R_0 L \Omega U}}_{1} \frac{1}{\tilde{\rho}_0} \frac{\partial \langle \tilde{\hat{p}} \rangle}{\partial \tilde{x}}
$$
$$
+ \underbrace{\frac{N}{\Omega L^2}}_{10^{-11}} \left[\frac{\partial}{\partial \tilde{x}} \left(\tilde{\nu} \frac{\partial \langle \tilde{u} \rangle}{\partial \tilde{x}} \right) + \frac{\partial}{\partial \tilde{y}} \left(\tilde{\nu} \frac{\partial \langle \tilde{u} \rangle}{\partial \tilde{y}} \right) \right] - \underbrace{\frac{U^{*2}}{\Omega U L}}_{10^{-3}} \left[\frac{\partial}{\partial \tilde{x}} \left(\langle \tilde{u}' \tilde{u}' \rangle \right) + \frac{\partial}{\partial \tilde{y}} \left(\langle \tilde{u}' \tilde{v}' \rangle \right) \right]
\tag{A.3}
$$
$$
+ \underbrace{\frac{N}{\Omega H^2}}_{10^{-11}} \frac{\partial}{\partial \tilde{z}} \left(\tilde{\nu} \frac{\partial \langle \tilde{u} \rangle}{\partial \tilde{z}} \right) - \underbrace{\frac{U^{*2}}{\Omega U H}}_{1} \frac{\partial}{\partial \tilde{z}} \left(\langle \tilde{u}' \tilde{w}' \rangle \right).
$$

Since all variables with a tilde are of the order of $\mathcal{O}(1)$, we can identify the terms which are the leading ones and which terms' contribution is neglectable. We clearly see that the terms, describing the molecular diffusion, are many orders smaller than the leading pressure gradient, Coriolis term and the vertical turbulence term and therefore negligible. Neglecting all terms which are smaller than 1% of the leading terms, we can simplify the x-component of the RANS to:

$$
\frac{\partial \langle u \rangle}{\partial t} + \langle u \rangle \frac{\partial \langle u \rangle}{\partial x} + \langle v \rangle \frac{\partial \langle u \rangle}{\partial y} + \langle w \rangle \frac{\partial \langle u \rangle}{\partial z} - f \langle v \rangle = -\frac{1}{\rho_0} \frac{\partial \langle \hat{p} \rangle}{\partial x} - \frac{\partial}{\partial z} \langle u'w' \rangle.
\tag{A.4}
$$

The scaling for the y-component is analogous:

$$
\frac{\partial \langle v \rangle}{\partial t} + \langle u \rangle \frac{\partial \langle v \rangle}{\partial x} + \langle v \rangle \frac{\partial \langle v \rangle}{\partial y} + \langle w \rangle \frac{\partial \langle v \rangle}{\partial z} + f \langle u \rangle = -\frac{1}{\rho_0} \frac{\partial \langle \hat{p} \rangle}{\partial y} - \frac{\partial}{\partial z} \langle v'w' \rangle.
\tag{A.5}
$$

For the scaling of the z component of the RANS we do the same steps as before. The z-component reads as:

$$\frac{\partial \langle w \rangle}{\partial t} + \langle u \rangle \frac{\partial \langle w \rangle}{\partial x} + \langle v \rangle \frac{\partial \langle w \rangle}{\partial y} + \langle w \rangle \frac{\partial \langle w \rangle}{\partial z} - f^* \langle u \rangle = -\frac{1}{\rho_0} \frac{\partial \langle p \rangle}{\partial z} - \frac{\langle \hat{\rho} \rangle}{\rho_0} g + \frac{\partial}{\partial x} \left(\nu \frac{\partial \langle w \rangle}{\partial x} - \langle w'u' \rangle \right)$$
$$+ \frac{\partial}{\partial y} \left(\nu \frac{\partial \langle w \rangle}{\partial y} - \langle w'v' \rangle \right) + \frac{\partial}{\partial z} \left(\nu \frac{\partial \langle w \rangle}{\partial z} - \langle w'w' \rangle \right),$$

$$(A.6)$$

with $f^* = 2\Omega \cos(\phi)$ which we approximate with the same order as f. Now we insert (A.1) again and divide by ΩU:

$$\underbrace{\frac{W}{\Omega L}}_{10^{-4}} \left[\frac{\partial \langle \tilde{w} \rangle}{\partial \tilde{t}} + \langle \tilde{u} \rangle \frac{\partial \langle \tilde{w} \rangle}{\partial \tilde{x}} + \langle \tilde{v} \rangle \frac{\partial \langle \tilde{w} \rangle}{\partial \tilde{y}} \right] + \underbrace{\frac{W^2}{\Omega U H}}_{10^{-4}} \langle \tilde{w} \rangle \frac{\partial \langle \tilde{w} \rangle}{\partial \tilde{z}} - \tilde{\Omega} \langle \tilde{u} \rangle = \underbrace{\frac{P}{\Omega U R_0 H}}_{10^3} \frac{1}{\tilde{\rho}_0} \frac{\partial \langle \tilde{\hat{p}} \rangle}{\partial \tilde{z}}$$
$$+ \underbrace{\frac{RG}{\Omega U R_0}}_{10^4} \frac{\langle \tilde{\hat{\rho}} \rangle}{\tilde{\rho}_0} \tilde{g} + \underbrace{\frac{NW}{\Omega U L^2}}_{10^{-14}} \left[\frac{\partial}{\partial \tilde{x}} \left(\tilde{\nu} \frac{\partial \langle \tilde{w} \rangle}{\partial \tilde{x}} \right) + \frac{\partial}{\partial \tilde{y}} \left(\tilde{\nu} \frac{\partial \langle \tilde{w} \rangle}{\partial \tilde{y}} \right) \right] - \underbrace{\frac{U^{*2}}{\Omega U L}}_{10^{-3}} \left[\frac{\partial}{\partial \tilde{x}} \left(\langle \tilde{w}' \tilde{u}' \rangle \right) + \frac{\partial}{\partial \tilde{y}} \left(\langle \tilde{w}' \tilde{v}' \rangle \right) \right]$$
$$+ \underbrace{\frac{NW}{\Omega U H^2}}_{10^{-8}} \frac{\partial}{\partial \tilde{z}} \left(\tilde{\nu} \frac{\partial \langle \tilde{w} \rangle}{\partial \tilde{z}} \right) - \underbrace{\frac{U^{*2}}{\Omega U H}}_{1} \frac{\partial}{\partial \tilde{z}} \left(\langle \tilde{w}' \tilde{w}' \rangle \right).$$

$$(A.7)$$

Neglecting again all terms which are smaller than 1% of the leading term we find the hydrostatic approximation:

$$\frac{\partial \langle \hat{p} \rangle}{\partial z} = -\langle \hat{\rho} \rangle g \,. \tag{A.8}$$
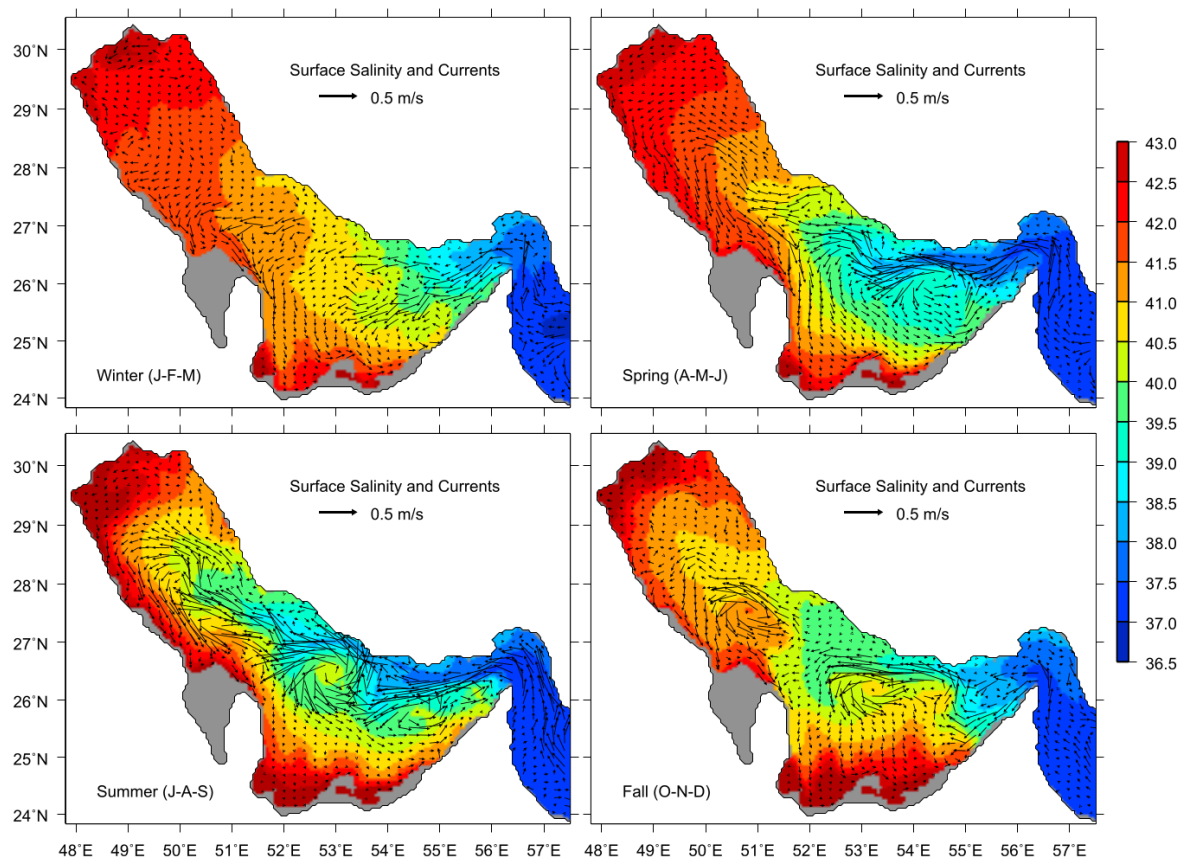
Appendix B.

Plots for validation

Figure B.1.: The surface salinity distribution and surface circulation found by Yao and Johns (2010b) (figure 10). Regions with salinities < 39 psu are marked grey.
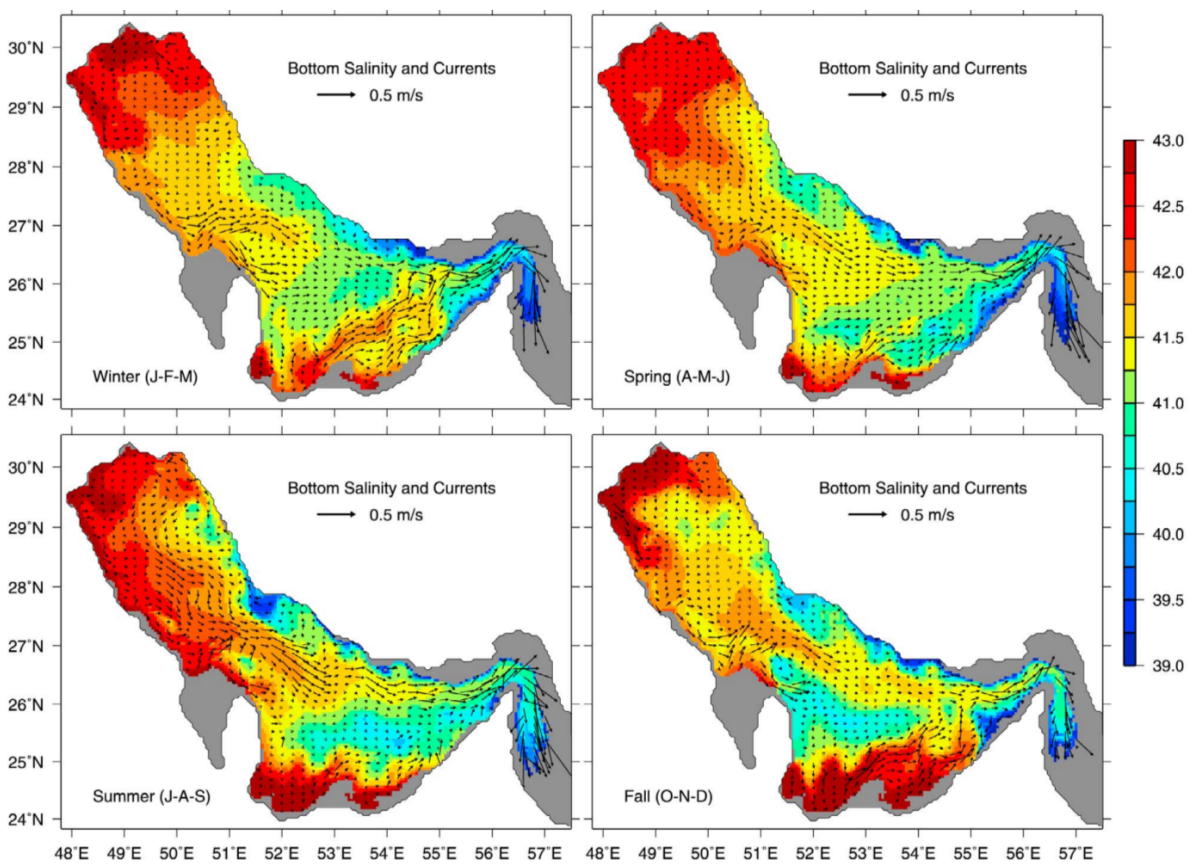
Figure B.2.: The bottom salinity distribution and surface circulation found by Yao and Johns (2010a) (figure 7). Regions with salinities < 39 psu are marked grey.
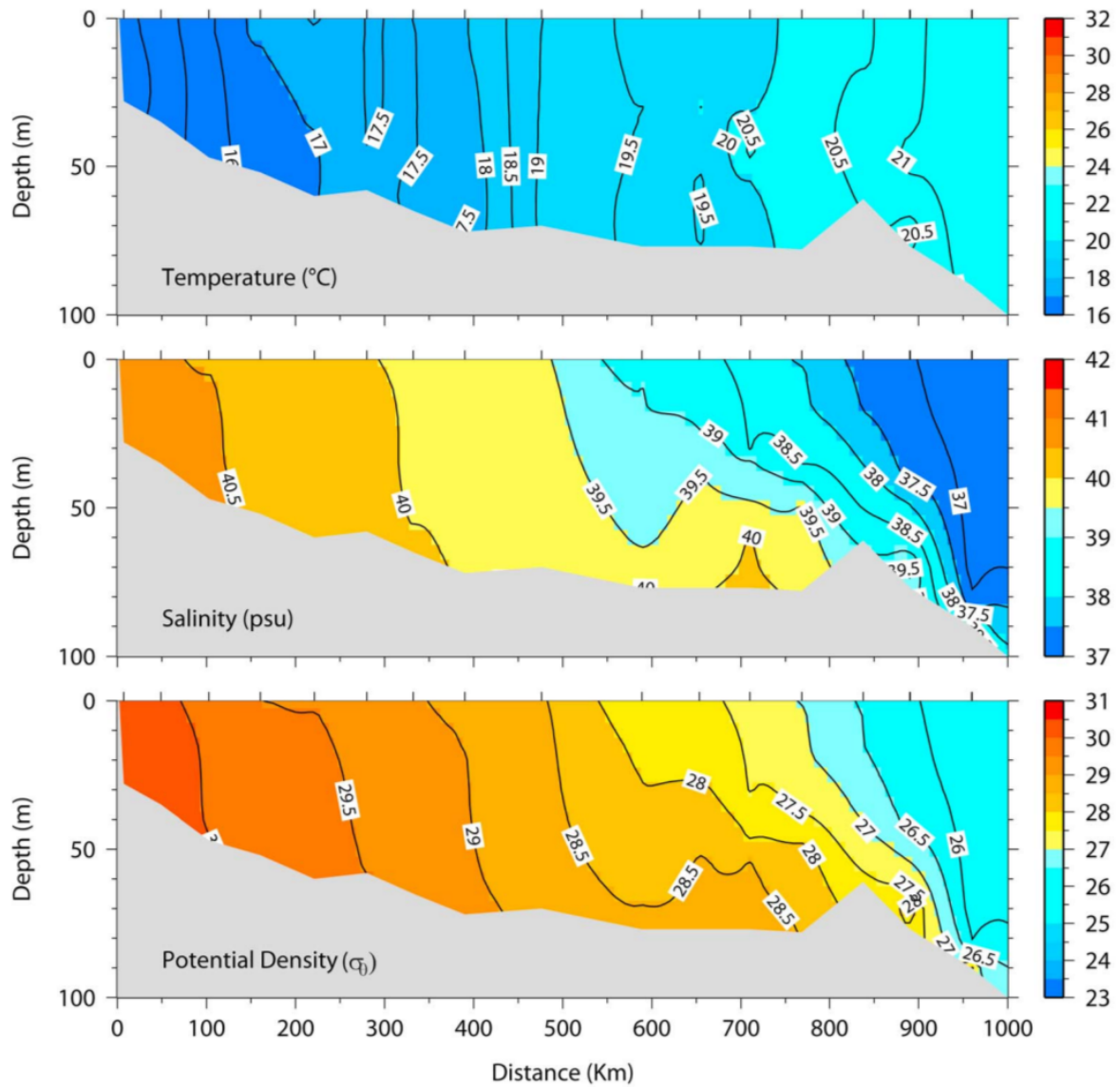
Figure B.3.: Temperature, salinity and density distribution along the axial transect of Mt. Mitchell expedition by Reynolds (1993) (figure 11) replotted by Yao and Johns (2010a) (figure 1a).
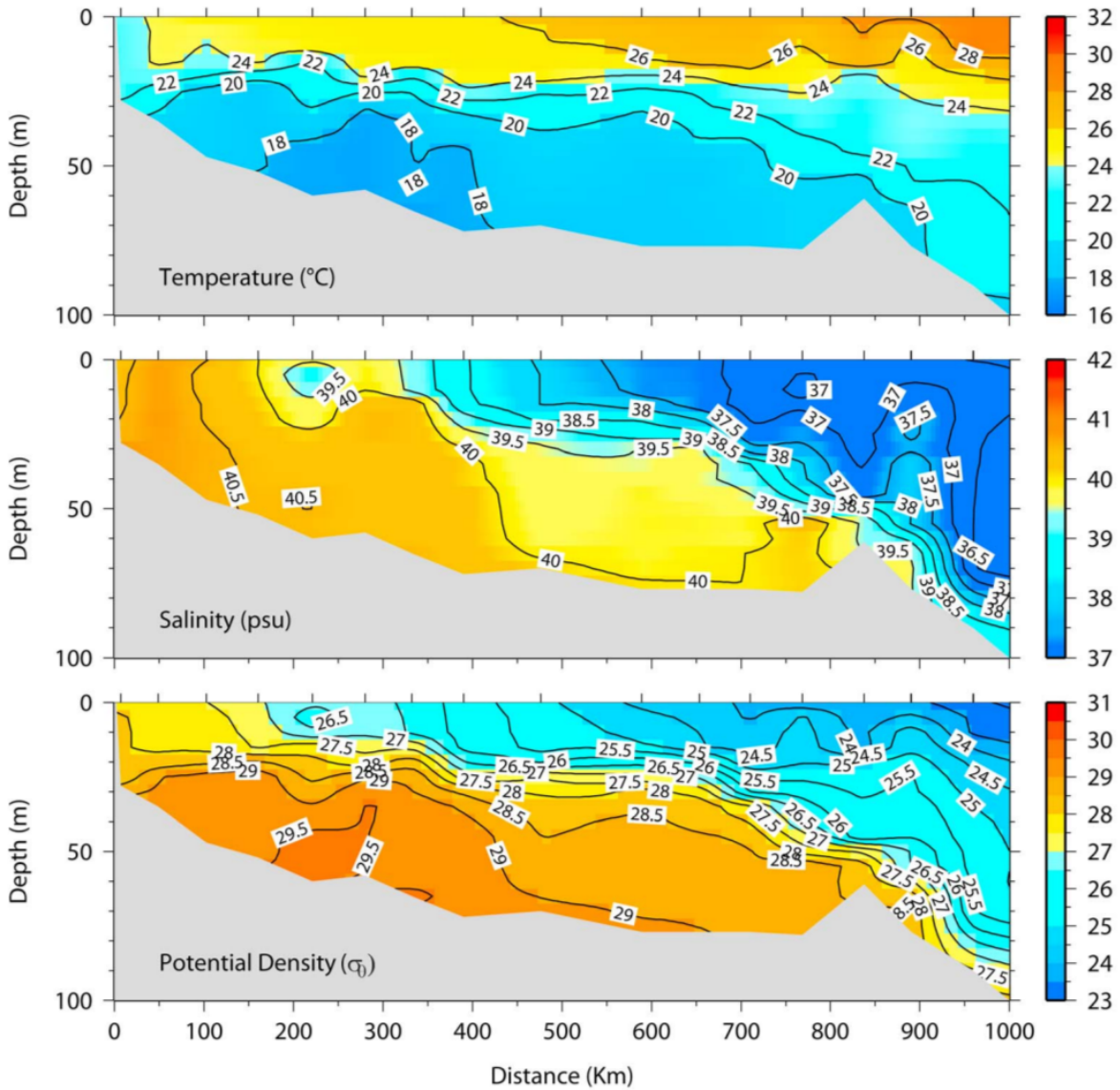
Figure B.4.: Temperature, salinity and density distribution along the axial transect of Mt. Mitchell expedition by Reynolds (1993) (figure 12) replotted by Yao and Johns (2010a) (figure 2a).
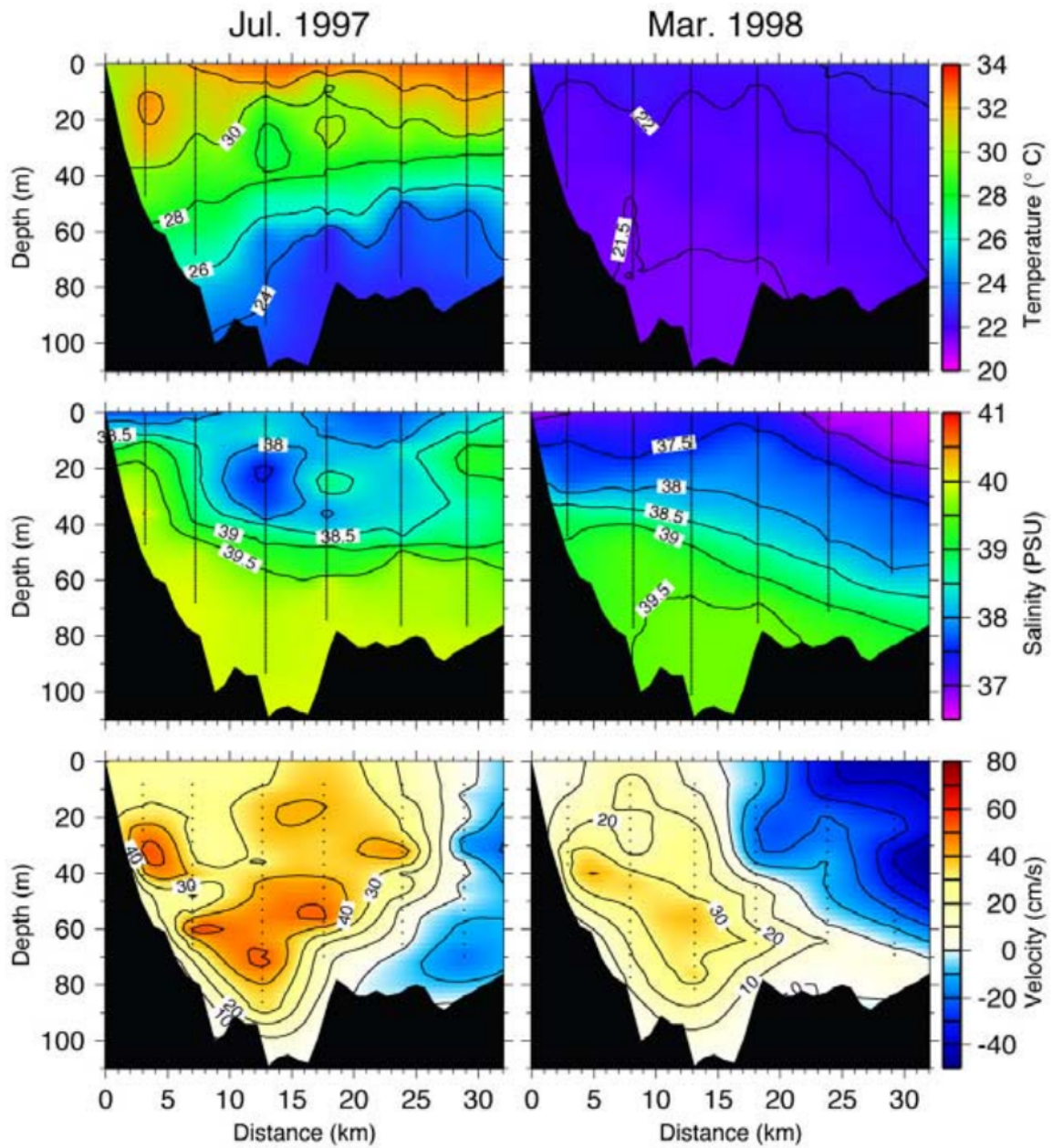
Figure B.5.: Temperature (top), salinity (middle) and velocity (bottom) distribution measured by Johns et al. (2003) (figure 10b) for July 1997 and March 1998.

Bibliography

F Ahmad and SAR Sultan. Annual mean surface heat fluxes in the Arabian Gulf and the net heat transport through the Strait of Hormuz. *Atmosphere-Ocean*, 29(1):54–61, 1991.

Christopher Amante and Barry W Eakins. *ETOPO1 1 arc-minute global relief model: procedures, data sources and analysis*. US Department of Commerce, National Oceanic and Atmospheric Administration, National Environmental Satellite, Data, and Information Service, National Geophysical Data Center, Marine Geology and Geophysics Division Colorado, 2009.

Laurence Armi. Some evidence for boundary mixing in the deep ocean. *Journal of Geophysical Research: Oceans*, 83(C4):1971–1979, 1978.

FJ Beron-Vera, J Ochoa, and P Ripa. A note on boundary conditions for salt and freshwater balances. *Ocean Modelling*, 1(2):111–118, 1999.

Hans Burchard and Thomas H Badewien. Thermohaline residual circulation of the Wadden Sea. *Ocean Dynamics*, 65(12):1717–1730, 2015.

Hans Burchard and Helmut Baumert. The formation of estuarine turbidity maxima due to density effects in the salt wedge. A hydrodynamic process study. *Journal of Physical Oceanography*, 28(2):309–321, 1998.

Hans Burchard and Jean-Marie Beckers. Non-uniform adaptive vertical grids in one-dimensional numerical ocean models. *Ocean Modelling*, 6(1):51–81, 2004.

Hans Burchard and Karsten Bolding. *GETM: A General Estuarine Transport Model; Scientific Documentation*. European Commission, Joint Research Centre, Institute for Environment and Sustainability, 2002.

Hans Burchard and Robert D Hetland. Quantifying the contributions of tidal straining and gravitational circulation to residual circulation in periodically stratified tidal

estuaries. *Journal of Physical Oceanography*, 40(6):1243–1262, 2010.

Hans Burchard and Ole Petersen. Hybridization between σ-and z-coordinates for improving the internal pressure gradient calculation in marine models with steep bottom slopes. *International journal for numerical methods in fluids*, 25(9):1003–1023, 1997.

Hans Burchard and Hannes Rennau. Comparative quantification of physically and numerically induced mixing in ocean models. *Ocean Modelling*, 20(3):293–311, 2008.

Hans Burchard, Karsten Bolding, and Manuel R Villarreal. *GOTM, a general ocean turbulence model: theory, implementation and test cases*. Space Applications Institute, 1999.

Hans Burchard, Xaver Lange, Knut Klingbeil, and Parker MacCready. Estuarine mixing. 2017 in prep.

Eric P Chassignet, Harley E Hurlburt, Ole Martin Smedstad, George R Halliwell, Patrick J Hogan, Alan J Wallcraft, Remy Baraille, and Rainer Bleck. The HYCOM (hybrid coordinate ocean model) data assimilative system. *Journal of Marine Systems*, 65(1): 60–83, 2007.

S Claus, N De Hauwere, B Vanhoorne, F Hernandez, and J Mees. Marineregions. org. *Flanders Marine Institute. Retrieved November*, 26:2014, 2014.

DP Dee, SM Uppala, AJ Simmons, Paul Berrisford, P Poli, S Kobayashi, U Andrae, MA Balmaseda, G Balsamo, P Bauer, et al. The ERA-Interim reanalysis: Configuration and performance of the data assimilation system. *Quarterly Journal of the royal meteorological society*, 137(656):553–597, 2011.

Craig J Donlon, Matthew Martin, John Stark, Jonah Roberts-Jones, Emma Fiedler, and Werenfrid Wimmer. The operational sea surface temperature and sea ice analysis (OSTIA) system. *Remote Sensing of Environment*, 116:140–158, 2012.

Gary D Egbert and Svetlana Y Erofeeva. Efficient inverse modeling of barotropic ocean tides. *Journal of Atmospheric and Oceanic Technology*, 19(2):183–204, 2002.

Rainer Feistel. A Gibbs function for seawater thermodynamics for -6 to 80°C and salinity up to 120g/kg. *Deep Sea Research Part I: Oceanographic Research Papers*, 55(12): 1639–1671, 2008.

NG Freeman, AM Hale, and MB Danard. A modified sigma equations' approach to the numerical modeling of Great Lakes hydrodynamics. *Journal of Geophysical Research*, 77(6):1050–1060, 1972.

W Rockwell Geyer, John H Trowbridge, and Melissa M Bowen. The dynamics of a partially mixed estuary. *Journal of Physical Oceanography*, 30(8):2035–2048, 2000.

Ulf Gräwe, Peter Holtermann, Knut Klingbeil, and Hans Burchard. Advantages of vertically adaptive coordinates in numerical models of stratified shelf seas. *Ocean Modelling*, 92:56–68, 2015.

Dale B Haidvogel and Aike Beckmann. *Numerical ocean circulation modeling*, volume 2. World Scientific, 1999.

Donald V Hansen and Maurice Rattray Jr. Gravitational circulation in straits and estuaries. 1966.

Richard Hofmeister, Hans Burchard, and Jean-Marie Beckers. Non-uniform adaptive vertical grids for 3D numerical ocean models. *Ocean Modelling*, 33(1):70–86, 2010.

Rudolf B Husar, Joseph M Prospero, and Larry L Stowe. Characterization of tropospheric aerosols over the oceans with the NOAA advanced very high resolution radiometer optical thickness operational product. *Journal of Geophysical Research: Atmospheres*, 102(D14):16889–16909, 1997.

VC John, SL Coles, and AI Abozed. Seasonal cycles of temperature, salinity and water masses of the western Arabian Gulf. *Oceanologica Acta*, 13(3):273–281, 1990.

WE Johns, F Yao, DB Olson, SA Josey, JP Grist, and DA Smeed. Observations of seasonal exchange through the Straits of Hormuz and the inferred heat and freshwater budgets of the Persian Gulf. *Journal of Geophysical Research: Oceans*, 108(C12), 2003.

Jochen Kämpf and Masoud Sadrinasab. The circulation of the Persian Gulf: a numerical study. *Ocean Science*, 2(1):27–41, 2006.

Knut Klingbeil, Mahdi Mohammadi-Aragh, Ulf Gräwe, and Hans Burchard. Quantification of spurious dissipation and mixing–Discrete variance decay in a Finite-Volume framework. *Ocean Modelling*, 81:49–64, 2014.

Martin Knudsen. Ein hydrographischer Lehrsatz. *Annalen der Hydrographie und Maritimen Meteorologie*, 28(7):316–320, 1900.

Junsei Kondo. Air-sea bulk transfer coefficients in diabatic conditions. *Boundary-Layer Meteorology*, 9(1):91–112, 1975.

Parker MacCready. Calculating estuarine exchange flow using isohaline coordinates. *Journal of Physical Oceanography*, 41(6):1116–1124, 2011.

Parker MacCready and W Rockwell Geyer. Advances in estuarine physics. *Annual Review of Marine Science*, 2:35–58, 2010.

Hossein Mashayekh Poul. Modelling tidal processes in the Persian Gulf - with a view on Renewable Energy -. *Ph.D. Thesis*, 2016.

Trevor J McDougall and Paul M Barker. Getting started with TEOS-10 and the Gibbs Seawater (GSW) oceanographic toolbox. *SCOR/IAPSO WG*, 127:1–28, 2011.

RA Nunes and GW Lennon. Physical property distributions and seasonal trends in Spencer Gulf, South Australia: an inverse estuary. *Marine and Freshwater Research*, 37(1):39–53, 1986.

Norman A Phillips. A coordinate system having some special advantages for numerical forecasting. *Journal of Meteorology*, 14(2):184–185, 1957.

SP Pous, Xavier Carton, and Pascal Lazure. Hydrology and circulation in the Strait of Hormuz and the Gulf of Oman—Results from the GOGP99 Experiment: 1. Strait of Hormuz. *Journal of Geophysical Research: Oceans*, 109(C12), 2004.

Stéphane Pous, Xavier Carton, and Pascal Lazure. A process study of the tidal circulation in the Persian Gulf. *Open Journal of Marine Science*, 2(04):131–140, 2012.

Stéphane Pous, Pascal Lazure, and Xavier Carton. A model of the general circulation in the Persian Gulf and in the Strait of Hormuz: Intraseasonal to interannual variability. *Continental Shelf Research*, 94:55–70, 2015.

David K Ralston, W Rockwell Geyer, and James A Lerczak. Subtidal salinity and velocity in the Hudson River estuary: Observations and modeling. *Journal of Physical Oceanography*, 38(4):753–770, 2008.

R Michael Reynolds. Physical oceanography of the Gulf, Strait of Hormuz, and the Gulf of Oman—Results from the Mt Mitchell expedition. *Marine Pollution Bulletin*, 27: 35–59, 1993.

Masoud Sadrinasab and Jochen Kämpf. Three-dimensional flushing times of the Persian Gulf. *Geophysical research letters*, 31(24), 2004.

Joseph Smagorinsky. General circulation experiments with the primitive equations: I. The basic experiment. *Monthly weather review*, 91(3):99–164, 1963.

John D Stark, Craig J Donlon, Matthew J Martin, and Michael E McCulloch. OSTIA: An operational, high resolution, real time, global sea surface temperature analysis system. In *Oceans 2007-Europe*, pages 1–4. IEEE, 2007.

Stephen A Swift and Amy S Bower. Formation and circulation of dense water in the Persian/Arabian Gulf. *Journal of Geophysical Research: Oceans*, 108(C1), 2003.

Prasad G Thoppil and Patrick J Hogan. On the mechanisms of episodic salinity outflow events in the Strait of Hormuz. *Journal of Physical Oceanography*, 39(6):1340–1360, 2009.

Prasad G Thoppil and Patrick J Hogan. A modeling study of circulation and eddies in the Persian Gulf. *Journal of Physical Oceanography*, 40(9):2122–2134, 2010.

Elina Tragou, Chris Garrett, Richard Outerbridge, and Craig Gilman. The heat and freshwater budgets of the Red Sea. *Journal of physical oceanography*, 29(10):2504–2522, 1999.

JS Turner. Turbulent entrainment: the development of the entrainment assumption, and its application to geophysical flows. *Journal of Fluid Mechanics*, 173:431–471, 1986.

Lars Umlauf and Hans Burchard. Second-order turbulence closure models for geophysical boundary layers. A review of recent work. *Continental Shelf Research*, 25(7): 795–827, 2005.

ICES UNESCO and IAPSO SCOR. Background papers and supporting data on the international equation of state of seawater 1980, 1981.

SD Woodruff, RJ Slutz, RL Jenne, and PM Steurer. Comprehensive Ocean–Atmosphere Data Set (COADS) Release 1a: 1980–92. *Earth Syst. Monitor*, 4(1):1–8, 1993.

Carl Wunsch. On oceanic boundary mixing. In *Deep Sea Research and Oceanographic Abstracts*, volume 17, pages 293–301. Elsevier, 1970.

Fengchao Yao and William E Johns. A HYCOM modeling study of the Persian Gulf: 2. Formation and export of Persian Gulf Water. *Journal of Geophysical Research: Oceans*, 115(C11), 2010a.

Fengchao Yao and William E Johns. A HYCOM modeling study of the Persian Gulf: 1. Model configurations and surface circulation. *Journal of Geophysical Research: Oceans*, 115(C11), 2010b.

Selbstständigkeitserklärung

Ich versichere hiermit an Eides statt, dass ich die vorliegende Arbeit selbstständig angefertigt und ohne fremde Hilfe verfasst habe, keine außer den von mir angegebenen Hilfsmitteln und Quellen dazu verwendet habe und die den benutzten Werken inhaltlich und wörtlich entnommenen Stellen als solche kenntlich gemacht habe.

Rostock, (Datum)